arXiv:2111.05788v1 [hep-ex] 10 Nov 2021

Science Case for the new High-Intensity Muon Beams HIMB at PSI

Edited by A. Knecht, F. Meier Aeschbacher, T. Prokscha, S. Ritt, A. Signer

M. Aiba[1], A. Amato[1], A. Antognini[1,2], S. Ban[3], N. Berger[4], L. Caminada[1,5], R. Chislett[6], P. Crivelli[2], A. Crivellin[1,5], G. Dal Maso[1,2], S. Davidson[7], M. Hoferichter[8], R. Iwai[2], T. Iwamoto[3], K. Kirch[1,2], A. Knecht[1], U. Langenegger[1], A. M. Lombardi[9], H. Luetkens[1], F. Meier Aeschbacher[1], T. Mori[3], J. Nuber[1,2], W. Ootani[3], A. Papa[1,10], T. Prokscha[1], F. Renga[11], S. Ritt[1], M. Sakurai[2], Z. Salman[1], P. Schmidt-Wellenburg[1], A. Schöning[12], A. Signer[1,5,*], A. Soter[2], L. Stingelin[1], Y. Uchiyama[3], and F. Wauters[4]

[1]Paul Scherrer Institut, 5232 Villigen PSI, Switzerland
[2]Institute for Particle Physics and Astrophysics, ETH Zurich, 8093 Zürich, Switzerland
[3]ICEPP, The University of Tokyo, 7-3-1 Hongo, Bunkyo-ku, Tokyo, 113-0033, Japan
[4]Institute for Nuclear Physics and PRISMA$^+$ Cluster of Excellence, Johannes Gutenberg University Mainz, Germany
[5]Physik-Institut, Universität Zürich, 8057 Zürich, Switzerland
[6]Department of Physics and Astronomy, University College London, WC1E 6BT, United Kingdom
[7]LUPM, Université de Montpellier, Place Eugène Bataillon, 34095 Montpellier, France
[8]Albert Einstein Center for Fundamental Physics, Institute for Theoretical Physics, University of Bern, Sidlerstrasse 5, 3012 Bern, Switzerland
[9]CERN, 1211 Geneva 23, Switzerland
[10]Dipartimento di Fisica E. Fermi & INFN Sezione di Pisa, Largo Bruno Pontecorvo, Edificio C, 208, 56127 Pisa, Italy
[11]INFN Sezione di Roma, Piazzale A. Moro 2, 00185 Roma, Italy
[12]Physikalisches Institut, Universität Heidelberg, Im Neuenheimer Feld 226, 69120 Heidelberg, Germany
[*]Corresponding author: adrian.signer@psi.ch

In April 2021, scientists active in muon physics met to discuss and work out the physics case for the new High-Intensity Muon Beams (HIMB) project at PSI that could deliver of order $10^{10}\,\mathrm{s}^{-1}$ surface muons to experiments. Ideas and concrete proposals were further substantiated over the following months and assembled in the present document. The high intensities will allow for completely new experiments with considerable discovery potential and unique sensitivities. The physics case is outstanding and extremely rich, ranging from fundamental particle physics via chemistry to condensed matter research and applications in energy research and elemental analysis. In all these fields, HIMB will ensure that the facilities SμS and CHRISP on PSI's High Intensity Proton Accelerator complex HIPA remain world-leading, despite the competition of muon facilities elsewhere.

Contents

1 Introduction **4**

2 Particle physics with HIMB **5**

2.1 Muon flavour physics . . . 5
2.2 The Mu3e experiment . . . 8
2.2.1 Mu3e final focus . . . 9
2.2.2 Muon stopping target . . . 11
2.2.3 Mu3e signal and background . . . 13
2.2.4 Mu3e phase II detector design . . . 14
2.2.5 Online data processing at high rates . . . 16
2.2.6 Mu3e-Gamma . . . 16
2.3 $\mu \to e\gamma$ . . . 18
2.3.1 General introduction . . . 18
2.3.2 Gaseous positron tracker . . . 21
2.3.3 Photon calorimeter . . . 23
2.3.4 Photon conversion spectrometer . . . 26
2.3.5 Silicon pixel sensor for $\mu \to e\gamma$ . . . 29
2.4 Muon moments . . . 31
2.4.1 $g-2$ and muon electric dipole moment . . . 32
2.4.2 A $g-2$ / EDM measurement at PSI . . . 35
2.4.3 Prospects for a search of the muon electric dipole moment . . . 36
2.4.4 Prospects for a high-precision measurement of the muon $g-2$ . . . 38
2.4.5 Conclusion . . . 39
2.5 Muonium . . . 41
2.5.1 Development of novel muonium sources at PSI . . . 41
2.5.2 Spectroscopy . . . 42
2.5.3 Gravitational free fall experiment of muonium . . . 44
2.6 Further particle-physics applications . . . 47
2.6.1 Muon decays . . . 47
2.6.2 Muonium - antimuonium oscillations . . . 49
2.6.3 Atomic parity violation in muonic atoms . . . 50
2.6.4 Muon conversion . . . 53

3 Muon spin spectroscopy and material science with HIMB **55**

3.1 Different muon sources around the world . . . 57
3.2 Current status of μSR at PSI . . . 57
3.3 New opportunities for μSR at HIMB: key science drivers . . . 60
3.3.1 Novel quantum materials . . . 62
3.3.2 Energy materials . . . 65
3.3.3 Pulsed beam and pump-probe . . . 66
3.3.4 Low-energy muons . . . 67
3.3.5 Elemental analysis and μSR . . . 70

4 The HIMB project & related beam and detector developments 71
4.1 The HIMB project 71
4.2 muCool beam development 74
4.3 Detector developments 86

5 Conclusions 88

Acknowledgements 88

References 90

Acronyms 115

1 Introduction

Muon physics covers research fields from fundamental particle physics to materials science. Muons are leptons with either negative or positive electric charge, such as electrons and positrons, but 207 times more massive and unstable. Muons are efficiently produced in weak decays of pions which are usually produced by proton beams hitting nuclei in some target material. Muons themselves decay again weakly, with a lifetime of about $2.2\,\mu$s. They have spin 1/2 and a magnetic moment.

In particle physics, since their first discovery, muons played an important role to help develop the theory and establish the present Standard Model of particle physics (SM). Muons are today used to perform some of the most sensitive tests to probe the limits of our theoretical understanding. In almost all presently existing tensions of experimental measurements with precision predictions of the SM muons are involved, suggesting they might be playing a key role in finding and establishing the breaking of this best theory to date. With a similarly long history, a broad range of research topics in solid-state physics, chemistry and materials science is being addressed by muon spin spectroscopy, usually using positive muons as highly sensitive local magnetic probes.

In all these fields, the availability of low-momentum, high-intensity muon beams is a prerequisite, and technological progress from muon production to detector development and sample environments boosted reach and capabilities of the research over decades.

World-wide, several large-scale facilities provide muons to experiments and user instrumentation. They are located at RAL (UK), at J-PARC (Japan), at TRIUMF (Canada) and at PSI in Switzerland. They are all active in condensed matter research, while broader programs in particle physics are pursued mostly at J-PARC and at PSI. A dedicated program in particle physics also exists at the muon campus of FNAL (USA). Several other accelerator facilities are developing or considering a future muon physics program, among them the CSNS (China), RAON (Korea), SNS (USA), and the ESS (Sweden). Some facilities provide pulsed, others continuous muon beams, complementing each other and allowing for different kinds of experiments.

The High Intensity Proton Accelerator facility HIPA at PSI [1] provides one of the most powerful proton beams to target stations, with 1.4 MW average beam power presently only matched by the pulsed SNS. HIPA has a 50 MHz time structure leading to quasi-continuous beams of slow muons. Many experiments today use so-called 'surface muons', positive muons generated in the decay of positive pions stopped close to the surface of a production target. These muons have well-defined momenta, are fully polarised and can be efficiently transported into secondary beam areas. The muon beams at PSI are presently leading the high-intensity frontier, with surface muon rates of order $10^8\,\mathrm{s}^{-1}$, and PSI is home to world-leading research in particle physics (see [2] for a recent review) and condensed matter research with muons (see [3–8] for reviews).

Installation of two new High-Intensity Muon Beams (HIMB), proposed within the IMPACT project (Isotope and Muon Production using Advanced Cyclotron and Target technology) at PSI, will constitute a leap forward for muon physics. Surface muon intensities will be boosted to $10^{10}\,\mathrm{s}^{-1}$, serving particle physics in one and condensed matter research in a second beamline. These unprecedented muon intensities will allow

for completely new experiments.

The interested national and international muon science community met for a HIMB physics case workshop, April 6-9, 2021 at PSI, as a kick-off event for the work presented in this paper. While we report on ongoing work and many aspects will be worked out over the coming years and many new, additional applications and ideas for HIMB will continue to appear, we have assembled here a compelling physics case documenting unprecedented opportunities for muon science. HIMB will secure a world-wide leading position of fundamental and applied muon science at PSI and attract many national and international user groups. Specific findings of future research cannot be predicted, however, it is clear that HIMB will have great impact. Projects to be conducted on this new facility will push the limit of the known far into presently unknown territory with plenty of opportunities for ground-breaking discovery, furthering basic knowledge and understanding of nature, development of novel technologies and fertilising spin-offs to other fields.

This paper is structured according to the two main use cases of the two beamline branches of HIMB as follows: Opportunities for particle physics are discussed in Section 2. Muon spin spectroscopy and materials science follow in Section 3. In Section 4 we deal with facility aspects, a short description of the lay-out and the properties of HIMB as well as further add-ons and technological aspects.

2 Particle physics with HIMB

2.1 Muon flavour physics

Flavour is arguably the least understood sector of the SM. There is still no compelling explanation as to why three copies (or flavours) of matter field families exist. Put specifically for charged leptons, why is there a muon and a tau in addition to the electron? According to the SM, the only difference between the various flavours is the coupling to the Higgs field, resulting in (widely) different masses.

Given the need to go beyond the SM it is natural to explore the sector that is least understood. Does the muon indeed behave precisely as the electron? There have been several recent measurements that cast doubt on this statement. The so-called B-anomalies seem to indicate that the decay of some B mesons involving a $\mu^+\,\mu^-$ pair in the final state do not precisely follow the pattern expected from corresponding decays with an electron-positron or tau pair in the final state [9–11]. Also, measurements of the anomalous magnetic moment (AMM) of the muon [12, 13] are in tension with the prediction of the SM [14]. Thus, it is not inconceivable that the role of the muon in particle physics will evolve from "who ordered that" to being the key to unlock the door to physics beyond the SM. Ever more precise investigations of processes involving muons are required to address these questions.

In the SM without right-handed (and therefore with massless) neutrinos, lepton flavour is conserved. Hence, a muon cannot decay into an electron without a muon neutrino and an electron antineutrino in the final state. The neutrinos are required to balance muon and electron flavour. However, this symmetry is accidental. Writing down all operators

with the fields of the SM, compatible with gauge invariance, Lorentz invariance, and renormalisability (i.e. of dimension 4 or less) it just so happens that there is no operator that violates lepton flavour symmetry. It is by no means a fundamental ingredient in the construction of the SM. And, more importantly, we know that this symmetry is broken in nature. Indeed, neutrinos have tiny but non-vanishing masses and as a result they oscillate, i.e. they change their flavour. This can be seen for example by letting muons decay and observe at a distant detector the emergence of electrons. This is precisely the observation of lepton flavour violation. Accordingly, the SM has to be modified by the introduction of right-handed neutrinos. This also leads charged lepton flavour violation (cLFV) in muon decays investigated at PSI such as $\mu \to e\gamma$ or $\mu \to eee$. In the SM with massive neutrinos, these decays can happen, albeit with a branching ratio (BR) smaller than 10^{-54}. Thus, while there is nothing sacred about lepton flavour, for practical purposes cLFV processes are forbidden in the SM and any measurement of such a process is a clear signal of beyond the Standard Model (BSM) physics. This offers a unique opportunity to search for BSM physics and has triggered a wealth of experimental and theoretical activities [15].

Similar to the introduction of right-handed neutrinos, a generic BSM model induces cLFV. As one typical example we mention supersymmetry. Even in the minimal supersymmetric Standard Model (MSSM) the soft breaking terms include numerous cLFV operators and currently there is no satisfactory explanation as to why they are absent or suppressed. The situation is similar for virtually all extensions of the SM. Thus, from a BSM point of view there is absolutely nothing exotic about cLFV. To the contrary, the absence of cLFV is exotic.

This can also be understood from an effective field theory (EFT) point of view. If we assume BSM physics is at a high scale well beyond the energy scale of the process, we can parameterise BSM effects through operators of dimension larger than 4. Using the SM fields, there is a single dimension 5 operator [16], closely linked to neutrino masses. At dimension 6, there are numerous operators including contact interactions (four-fermion operators) and dipole interactions among others [17, 18]. The flavour-diagonal dipole operators contribute to the electric dipole moment (EDM) and anomalous magnetic moment (AMM) of the corresponding particles. Their off-diagonal variants directly induce for example the cLFV decay $\mu \to e\gamma$. Similarly, off-diagonal four-fermion operators contribute to decays like $\mu \to eee$. Including a flavour-diagonal dimension 6 operator to parameterise BSM effects, but avoiding the corresponding cLFV operators requires either the introduction of an additional symmetry as explanation, or a fine-tuning for which there is currently no theoretical justification at all. In this connection it should also be mentioned that the conventional split into contributions from dipole and contact interactions is applicable at the high scale only. Through renormalisation-group evolution these operators mix and contact interactions directly impact, e.g., the $\mu \to e\gamma$ process [19, 20].

The mixing of different effects also implies that a diverse program is required to investigate cLFV. In case a signal is measured in a single process, it is impossible to pinpoint what precisely causes this cLFV decay. As for the current tension for the AMM of the muon, there will be many possible explanations. In order to narrow down

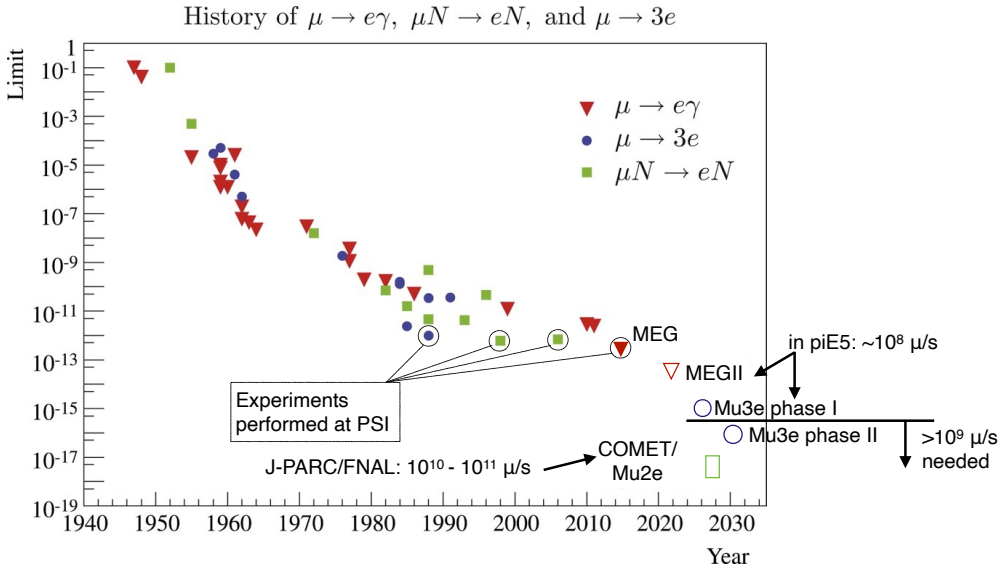

Figure 1: The history of limits for branching ratios of the three golden cLFV channels. Symbols that are not filled in indicate projected measurements. Plot modified from [21].

the nature of BSM that causes a potential cLFV decay it is imperative to measure or constrain as many such processes as possible. While this also concerns cLFV tau decays, the most stringent limits come from cLFV muon decays.

There are three golden cLFV muon-decay channels that have dramatic impact. In addition to the already mentioned $\mu \to e\,\gamma$, these are the decay $\mu \to e\,(e^+e^-)$ (or $\mu \to 3e$ for short) as well as the conversion of a muon to an electron in the field of a nucleus, $\mu\,N \to e\,N$. As illustrated in Figure 1, there is a long history of searches for such decays. The current best limits on the BR for all three decays have been obtained at PSI with $\mathrm{BR}(\mu \to 3e) < 1 \cdot 10^{-12}$ [22], $\mathrm{BR}(\mu \to e\gamma) < 4.2 \cdot 10^{-13}$ [23] and $\mathrm{BR}(\mu\,N \to e\,N) < 7 \cdot 10^{-13}$ [24].

The sensitivity to $\mu \to e\,\gamma$ and $\mu \to 3e$ will be improved further in the coming years. Using the currently existing beamline πE5 at PSI with $10^8\,\mu\,\mathrm{s}^{-1}$, MEG II [25] and phase I of Mu3e [26] aim to reach a sensitivity of $\mathrm{BR}(\mu \to e\gamma) = 6 \cdot 10^{-14}$ and $\mathrm{BR}(\mu \to 3e) \sim 2 \cdot 10^{-15}$, respectively.

To improve the sensitivity for the third golden channel, $\mu\,N \to e\,N$, it is advantageous to use a pulsed beam. At J-PARC and Fermilab a dedicated effort is ongoing by COMET [27] and Mu2e [28] with the long-term goal to increase the sensitivity for muon conversion by several orders of magnitude. For the other two channels a continuous muon beam is better suited. As illustrated in Figure 1, improving upon MEG II and phase I of Mu3e requires an increased muon intensity, as provided by the HIMB project. In fact, from the beginning it was envisaged to have a phase II for Mu3e and in Section 2.2 the decisive impact of HIMB for Mu3e will be described in detail. Prospects for measurements of $\mathrm{BR}(\mu \to e\gamma)$ beyond MEG II will be discussed in Section 2.3.

There are several observables linked to cLFV that can also be investigated more pre-

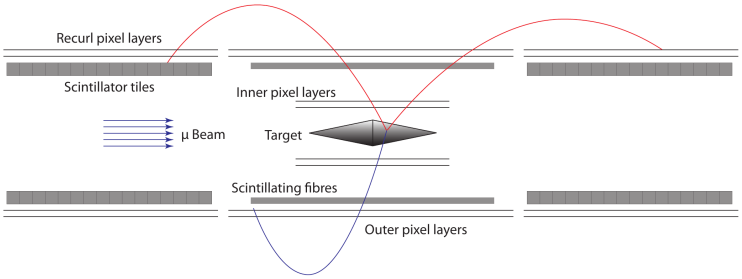

Figure 2: Schematic view of the Mu3e phase I experiment. Taken from [26].

cisely with HIMB. As already mentioned, the AMM and the EDM of the muon are related to the same dipole operator, albeit with diagonal flavour indices. Plans for future PSI activities in this direction are discussed in Section 2.4. Muonium, a bound state of a positive muon with an electron $M = (\mu^+ e^-)$ also serves as a clean probe for testing cLFV through oscillation into antimuonium $\overline{M} = (\mu^- e^+)$. More generally, muonium serves as a laboratory for quantum electrodynamics (QED) and gravity tests. This will be elaborated upon in Section 2.5. In Section 2.6 we will touch upon further possible applications of HIMB for particle physics with muons. Taken together, HIMB is an essential facility to fully explore the opportunities provided by high-intensity, low-energy experiments. It will ensure PSI remains at the forefront of this branch of particle physics, lead to further insights into its theory landscape [29] and trigger progress in experimental techniques that often has applications well beyond particle physics as well.

2.2 The Mu3e experiment

The Mu3e experiment at PSI is aiming to search for the lepton flavour violation decay of the muon in the reaction $\mu^+ \to e^+e^+e^-$ with unprecedented sensitivity.

The ultimate experimental sensitivity depends mainly on the achievable energy (momentum) resolution and has been estimated [30] to be $\mathcal{O}(10^{-16})$ single event sensititivity (SES) for the new and innovative conceptual design of the Mu3e experiment, and assuming state-of-the-art detector technologies. Another limitation comes from the available muon rate which, for a given number of muon stops, not only determines the total running time of the experiment but also the accidental background (BG) rate, and thus the maximum achievable sensitivity.

The validity of the experimental concept and the performance of the applied high-rate detector technologies will be tested during Mu3e phase I at the πE5 compact muon beam line, with an anticipated start of data taking in the year 2023. Experience collected during phase I will provide important input for the design of the phase II detector.

The design of the Mu3e phase I experiment is sketched in Figure 2 and shortly described here. A full description of the experimental setup is given in the Mu3e phase I

technical design report [26]. Positively charged muons with a momentum of about $p = 28\,\mathrm{MeV}/c$ ("surface muons") pass a moderator and are then stopped on a hollow double cone shaped target. The 10 cm long muon stopping target is surrounded by two layers of silicon pixel sensors which have a pixel size of $80\,\mu\mathrm{m} \times 80\,\mu\mathrm{m}$. Tracking is completed by the two outer pixel layers in the central region, and the up- and downstream recurl stations which register hits from back-curling tracks in the strong solenoidal magnetic fields of $B = 1\,\mathrm{T}$. All silicon pixel layers use the monolithic MuPix chip produced in high-voltage monolithic active pixel sensor (HVMAPS) technology [31, 32]. The ultra-thin pixel modules have a radiation length of only about $1 \times 10^{-3}\,\mathrm{X}_0$ and are cooled by an innovative gaseous helium system. The timing system consists of scintillating fibres in the central region and scintillating tiles placed up- and downstream from the central region. Both timing detector systems provide sub-nanosecond resolution to measure time coincidences. Vertex and timing information combined are crucial to suppress accidental BG, mainly originating from Bhabha scattered positrons in combination with ordinary Michel decays, see Section 2.2.3. The data are continuously readout and processed by a graphics processing unit (GPU) based filter farm which searches for three tracks pointing to a common vertex (3-prong) and reconstructs the charge and momentum of the particles.

In the following the proposed detector design for Mu3e phase II is presented, taking into account the HIMB constraints as well as the expected BG.

2.2.1 Mu3e final focus

The transverse beam emittance $\epsilon_{\mathrm{trans}} = \epsilon_x \cdot \epsilon_y$ of the HIMB will be about one order of magnitude larger compared to the compact muon beam line used for Mu3e phase I. The so-called matched beam size depends on the magnetic field B of the experimental solenoid

$$\sigma_{x,y}^{\mathrm{matched}} \quad = \quad \sqrt{\frac{2\epsilon_{x,y}\,p}{e\,B}} \tag{2.1}$$

with p being the muon momentum at the stopping target. To achieve an overall muon stopping efficiency similar to Mu3e phase I the diameter of the stopping target (38 mm in phase I) would have to be significantly increased.

However, a wider muon stopping target is detrimental to the requirement of an excellent vertex resolution which is mainly given by the track extrapolation uncertainties due to multiple scattering. As a consequence the accidental BG rejection scales with the muon stopping target diameter as $\approx 1/D^2$. Thus a small target diameter, and correspondingly small beam size, is favoured to achieve highest sensitivity in an accidental BG limited environment, see also discussion in Section 2.2.3

Consequently, one of the design challenges for Mu3e at HIMB is the minimisation of the matched beam size which can be achieved, according to (2.1), by three measures:

- reduction of the muon beam momentum p,
- increase of the magnetic field strength B of the experiment,

- special optics with oscillating beam envelope.

Simulation studies show that the initial muon beam momentum of about 28 MeV/c can be decreased using a moderator to about 16 $\pm$ 4 MeV/c without significantly losing muons. In order to profit from the lower beam momentum, the moderator must be placed in a region of small beam waist where the beam dispersion is large and the additional contribution from multiple scattering in the moderator is negligible. Several designs with different placements of the moderator, different type of moderators (solid and gaseous), and with and without pre-solenoids have been simulated by the method of single particle tracking. The simulation also considers the fringe field of the solenoid which significantly influences the trajectories of the very low momentum muons. For the example of a design with a solid moderator in the entrance region of the Mu3e solenoid, the 1 σ envelope is shown in Figure 3 (right). The most critical parameter for the muon transmission efficiency is the size of the beam pipe inside the experimental magnet. Simulation studies show that the transmission efficiency scales approximately linear with the beam-pipe radius in the region $R = 30$ - 50 mm. Whether the beam-pipe radius can be increased with respect to the phase I design (30 mm) needs to be answered by detailed technical design studies.

The second option is to increase the experimental solenoid field strength. According to (2.1) the beam size would shrink $\propto 1/\sqrt{B}$. At the same time, however, particles from the muon decay would be bent more strongly, leading to a larger acceptance loss of low-momentum tracks, if the detector system is not resized accordingly. Considering the already very tight space constraints of the Mu3e phase I design, a simple miniaturisation with two inner and two outer pixel layers would be very challenging. A better option is to add a third inner pixel layer. With three closely stacked pixel layers low-momentum tracks can be reconstructed which do not reach the outer pixel layers due to the strong

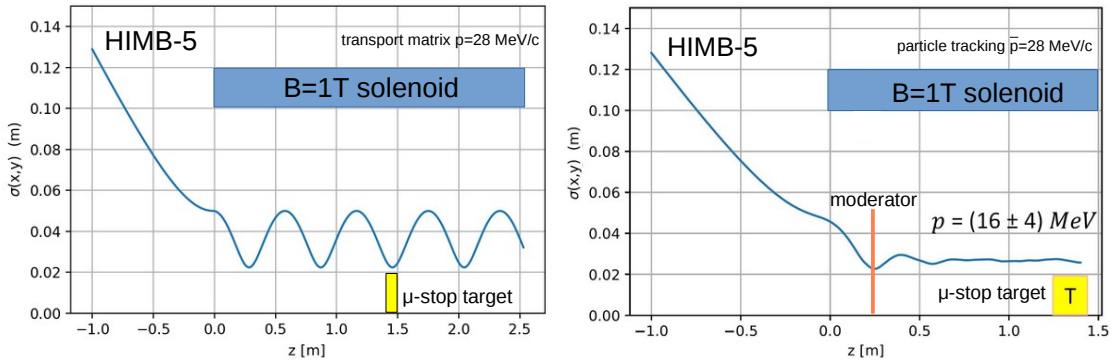

Figure 3: 1 σ beam envelopes for the HIMB-5 scenario (see Section 4.1) and a solenoid field of $B = 1$ T for an unmatched beam optics (left) and a matched beam optics (right) with a 600 μm mylar moderator placed inside the solenoid entrance region. The 1 σ beam envelope is determined by transport matrices (left) and using particle tracking including energy loss and multiple scattering in the moderator (right). The right plot is taken from [33] and has been modified.

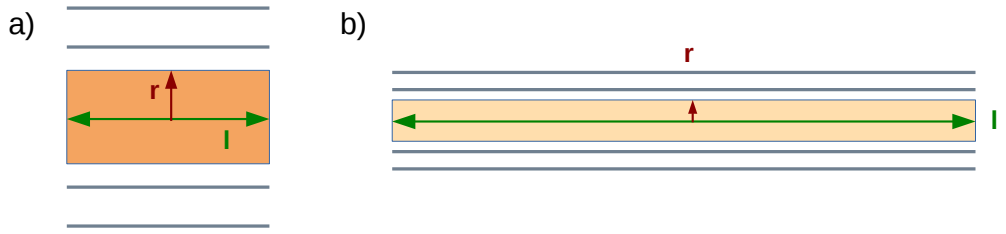

Figure 4: Longitudinal view of the Mu3e muon stopping target region for a) a short and wide, and b) a long and narrow geometry. The different brightnesses represent different average densities of the stopping material. The inner pixel tracking layers are shown in grey.

magnetic field. The higher redundancy also helps to reduce the hit combinatorics in the track reconstruction. Ideally, one of the three pixel layers would also provide very precise time information (timing layer). Designs with three inner pixel layers are discussed in the context of a combined Mu3e and MEG search in Section 2.2.6.

The third option is to use a special beam optics where the final focus of the muon beam is intentionally not matched with the experimental solenoid field. In that case the beam envelope inside the experiment oscillates with a wave length of $\approx 60\,\text{cm}$ for $B = 1\,\text{T}$ and $p = 28\,\text{MeV}/c$, see Figure 3 (left). This beam setup provides periodic minima which are significantly smaller than the equilibrium beam size. Such a design, however, is difficult to realise for several reasons: A) the beam pipe must be large to include all periodic beam waists, B) the minima are smeared out due to dispersion effects especially after placing a moderator, and C) the region around the minimum is relatively narrow, $\approx 10\,\text{cm}$, thus excluding a long muon stopping target which is favoured to reduce accidental BG.

2.2.2 Muon stopping target

Accidental BG can be best suppressed by using a long muon stopping target and by ensuring excellent vertex resolution, so that two muons decaying at the same time can be distinguished by tracking (vertexing). For a given beam momentum, the longitudinal radiation length X_L is fixed by the required stopping power and given by $X_L \propto l\rho$, with ρ being the average density of the muon stopping target. The transverse direction is the preferred detection plane. The average transverse radiation length is given by the product of target density and radius which should ideally match the beam size, $X_T \propto r\rho = X_L\, r/l$. Since X_T affects the signal particles (e.g. multiple scattering) and the generation of accidental BG (Bhabha), the primary design goal[1] is a long muon stopping target and a small beam size, see Figure 4.

The impact of the radial target size on the directional momentum resolution is illustrated in Figure 5. The accidental BG rate depends on the vertex resolution which is

[1]The relation between longitudinal and transverse radiation length holds, irrespective of the detailed stopping target geometry and material (gas, solid, etc.).

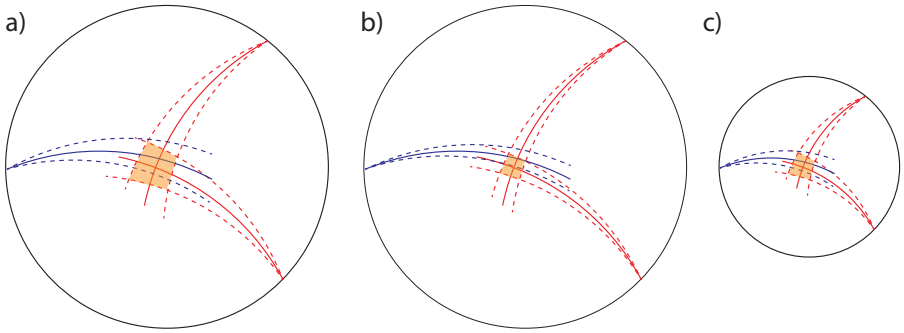

Figure 5: Transverse view of the Mu3e target region. Multiple scattering in the first detector layer leads to extrapolation uncertainties, defining the region susceptible to accidental BG (a). This region can be made smaller by reducing material in the first layer (b) or by reducing the transverse extent of the target region (c).

mainly determined by multiple scattering in the first tracking layer. The vertex resolution can be improved by reducing the material in the first tracking layer or by using a smaller target radius, thus reducing the extrapolation uncertainties.

For Mu3e phase II, a hollow double cone structure similar to phase I is considered as well as new ideas like silicon aerogel or gaseous targets. Gas is favourable for constructing a long muon stopping target and has also the advantage of a very small transverse radiation length. Active (instrumented) targets, which provide direct information about the muons stop/decay position, have the potential to improve the tracking, and therefore momentum resolution. However, the potential improvement is very small and probably not worth the effort[2].

Several target designs and materials have been simulated in a $B = 1\,\mathrm{T}$ field and optimised with the goal to equally distribute the muon stops along the beam direction [33]. For a muon stopping target radius of 19 mm, stopping rates of about $2 \times 10^9\,\mu/\mathrm{s}$ were calculated for solid state targets with different geometries (double cone, tilted plane, helicoid). The flattest stopping distribution on the longitudinal axis was achieved with a 30 cm long gaseous ethane target at atmospheric pressure. The corresponding total stopping rate is about $2.5 \times 10^9\,\mu/\mathrm{s}$ and slightly higher as for the solid targets. These estimates were obtained for a rather large beam-pipe radius of 50 mm. Which target design eventually is chosen will also depend on the technical feasibility to build a long ($\gg$10 cm) stopping target with low density.

[2] Active targets could also be used to reject accidental BG by identifying and rejecting close muon stops in space and time, which however also reduces the effective muon stopping rate.

2.2.3 Mu3e signal and background

Detailed studies of signal efficiencies and BG suppression have been performed in the context of Mu3e phase I and are documented in the technical design report [26]. Assuming a muon stopping rate of $1 \times 10^8\,\mu/\mathrm{s}$ a single event sensitivity of 2×10^{-15} is expected.

In order to reach the ultimate sensitivity goal of 10^{-16} at HIMB, higher muon stopping rates and an improved detector are required. In the following, some of the challenges for almost completely suppressing BG whilst keeping a reasonable signal efficiency in a much harsher environment are discussed.

For HIMB, we assume that a surface muon beam with $2 \times 10^9\,\mu/\mathrm{s}$ is stopped in the experiment and the muons decay at rest. The signal signature is then two positrons and one electron originating from a common vertex, coincident in time and with a four-momentum sum corresponding to a stopped muon. All BG processes that can mimic this signal topology need to be suppressed to an expectation of less than one BG event in the signal region over the lifetime of the experiment. The two main BG classes, namely the rare muon decay $\mu^+ \to e^+e^-e^+\nu\bar{\nu}$ and accidental combinations of two positrons and an electron are discussed below.

Besides an excellent BG suppression, a decent efficiency for the signal process is required in order to achieve the sensitivity goal in a reasonable amount of time. The efficiency is on the one hand limited by the detector geometry, which does not cover the area around the beam and defines a lower limit on reconstructable transverse momenta (roughly $10\,\mathrm{MeV}/c$ transverse momentum for the phase I Mu3e design). On the other hand, any gaps or deficient parts in the detector will affect the efficiency. As all three tracks have to be fully reconstructed, detector inefficiencies enter the final efficiency with a high power. The exact signal efficiency depends on the signal kinematics, which in turn depends on the type of new physics. For the phase I design it ranges from about 10% for pure dipole operators to about 19% for four-fermion operators [26, 34, 35]. With the planned improvements for the phase II detector design, see Section 2.2.4, the signal efficiency is expected to increase by at least 50% compared to phase I.

The process $\mu^+ \to e^+e^-e^+\nu\bar{\nu}$ is allowed in the SM and occurs with a BR of 3.4×10^{-5} [36]. It is indistinguishable from the signal process except for the energy and momentum carried away by the neutrinos. The invariant mass of the $e^+e^-e^+$ system has been calculated to next-to-leading order [37]. Close to the endpoint, the spectrum falls roughly with the sixth power of the *visible mass* and the branching fraction falls below 10^{-16} about $1\,\mathrm{MeV}/c^2$ below the endpoint, driving the requirements for the invariant mass resolution.

Combinations of different processes that in total have two positrons and one electron in the final state can mimic the signal signature if their origins in space and time are not resolvable by the detector and their combined kinematics match the signal. These accidental BGs scale with powers of the muon decay rate R. The ordinary muon decay is a very rich source of positrons. So when studying accidental BGs, sources of electrons have to be investigated, where those that appear in coincidence with a positron are particularly dangerous. Since most electron production processes scale with the amount

of material seen by positrons leaving the target region transverse to the beam X_T, see Figure 4, the best BG mitigation is to reduce all material to the minimum. Furthermore, accidental BGs can be reduced by good timing (σ_t) and vertex (σ_v) resolution as well as good resolution for the kinematics, e.g. the three-particle invariant mass resolution σ_{M_3}, and the centre-of-mass-system momentum resolution σ_p.

Detailed simulation studies for the phase I Mu3e experiment have shown that the most frequent accidental BG is from the combination of a Michel positron which undergoes Bhabha scattering in the detector material (leading to an e^+e^- pair) with another Michel positron. In order to match the signal kinematics, both Michel positrons must have energies close to the maximum allowed energy[3]. The scattering of a positron at $\approx 53\,\mathrm{MeV}/c$ with an electron at rest creates an e^+e^- pair with an invariant mass of $\approx 7\,\mathrm{MeV}/c^2$ which can be used to suppress this BG with little signal loss if the two particle invariant mass resolution σ_{M_2} is sufficiently small.

A similar BG topology is produced by a photon conversion combined with a Michel positron. The rarity of $\approx 53\,\mathrm{MeV}$ photons combined with the small amount of material in the muon stopping target region strongly suppresses this BG and obviates the need for a two-particle invariant mass cut (which would remove the expected signal kinematics in case of dominating dipole operators).

The third variety of accidental BG with two coincident particles combining with a Michel positron takes the e^+e^- pair from a rare muon decay $\mu^+ \to e^+e^-e^+\nu\bar{\nu}$. A detailed study of this BG was performed for the phase I Mu3e experiment [38], a simple rate extrapolation produces 17 events in the signal region for running the phase I apparatus under HIMB conditions, giving a target for the necessary improvements in kinematic, vertex and timing resolution.

Backgrounds with three unrelated particles can arise from combinations of any of the above processes which include one electron, or from Compton scattering with two Michel positrons. The BG rates scale with the muon rate to the third power, but are also suppressed by the vertex and timing resolution squared. Extrapolations from the phase I simulation show that at muon rates of a few 10^9 per second this kind of BG is completely negligible if the detector performance is sufficient to deal with the "2+1" accidental BG.

2.2.4 Mu3e phase II detector design

To further optimise the signal sensitivity it is planned to expand the geometrical acceptance for tracks with respect to Mu3e phase I design. This can be achieved by extending the pixel sensor instrumentation in up- and downstream directions. With the experience from Mu3e phase I, we believe that significantly larger tracking modules can be produced. For Mu3e phase II, we consider a vertex detector length of about 30 cm, see Figure 6, or even longer. Currently, the longest pixel modules for Mu3e phase I have a length of 36 cm. Twice as long pixel modules could be produced with a new pixel sensor generation with improved readout capabilities, like daisy chaining of the data.

[3]Note that this BG has its kinematic endpoint 1 electron mass *above* the muon mass, as the electron originates from the detector material and is not created in the muon decay.

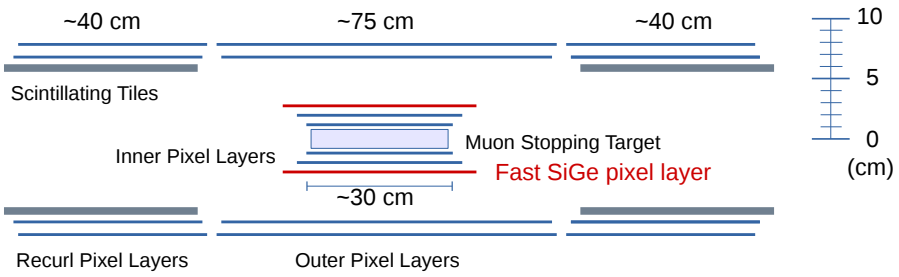

Figure 6: Sketch of an elongated detector design for Mu3e phase II at HIMB.

With such a design the requirements will be less stringent for the flexprint, where the individual pixel sensors are glued onto.

The detector technologies of Mu3e phase I were specifically chosen to prove the high-rate capability of the experiment for phase II and to pave the road for extremely high beam stopping rates in excess of $10^9\,\mu/\mathrm{s}$. Nonetheless, for Mu3e phase II several improvements with respect to the phase I detector are necessary to further suppress BG and to exploit the full HIMB potential. In addition to the extended vertex region and the increase of the overall acceptance, the scintillating fibre detector, see Figure 2, needs to be exchanged due to occupancy limitations. The alternative technology has to provide a significantly higher granularity and a time resolution of about 100 ps, or better. Therefore, the development of a monolithic silicon pad detector (PicoPix) based on the 130 nm SiGe BiCMOS process from IHP[4] was started. This technology was proven in test beams to provide time resolutions as good as $\mathcal{O}(100\,\mathrm{ps})$ for a design with sub-millimeter pixel size [39]. Replacing the scintillating fibre detector by a layer of PicoPix sensors would provide 4-dimensional information (time and spatial coordinates). The high granularity of these sensors will allow to place them at small radii close to the muon stopping target, see Figure 6. The PicoPix detector can be regarded as a fifth tracking layer, in addition to the four standard pixel layers, for which a new generation of MuPix sensors with improved time resolution and readout capabilities will be used. Running Mu3e at HIMB with about 20 times higher beam rates compared to phase I will substantially increase the hit combinatorial problem in the online track finding on the filter farm, see Section 2.2.5. The generally much improved time resolution of the tracking detectors will help to mitigate the combinatorial problem.

The final layout of the phase II design will be subject of further simulation studies. They will address the possibility to increase the magnetic field and to change the radius of the outer pixel layer to further improve the momentum resolution, see also Section 2.2.6. During the workshop also an idea was discussed to use the most inner pixel layer to stop the muons. With such a concept the rate of muon stops could be further increased. The feasibility of this idea needs to be experimentally studied.

[4]Institute for High Performance Microelectronics in Frankfurt/Oder, Germany

2.2.5 Online data processing at high rates

The data rate produced by the Mu3e detector at HIMB is three to four orders of magnitude larger than what can technologically and economically be saved to mass storage. The experiment thus relies on a fast and efficient on-line reconstruction, which identifies interesting events in real time. For the phase I experiment it was shown [40–42] that a compact and affordable farm of a dozen PCs with GPUs is capable of finding and fitting all relevant particle tracks and identifying three-track vertices, all using algorithms developed specifically for the multiple scattering dominated regime in which Mu3e operates [43–46]. Assuming a four-layer tracking on the filter farm, the computing power needed scales roughly with the third power of the rate; even with optimistic assumptions about the evolution of GPUs until the start of data taking at HIMB, this factor 8000 cannot be compensated simply by more and newer hardware. One key to tackling the online reconstruction challenge is improved time resolution of the pixel sensors, in particular in the vertex region. If a resolution of the order of 1 ns can be reached, the GPU only based approach is likely viable even at HIMB rates. Alternatively, large associative memories can be used for matching with pre-computed patterns; this option introduces additional complexity into the system, but we can profit from experience gained in the ATLAS hardware track trigger projects [47, 48].

2.2.6 Mu3e-Gamma

Considering the very high rates of the HIMB with up to $1 \times 10^{10}\,\mu$/s, a $\gamma \to e^+e^-$ converter can be considered for photon detection, despite the in general low conversion (detection) efficiency. By tracking the e^+e^- pair, a photon converter allows for a precise measurement of the photon position, a good measurement of the photon direction and a very precise measurement of the photon energy. This makes the converter option very interesting for the search $\mu^+ \to e^+\gamma$, see also section Section 2.3.4. In particular an active converter is of high interest as it further improves the excellent energy resolution of a photon converter tracker by directly measuring the energy loss of the e^+e^- pair in the converter, which is the main limitation for the energy resolution.

The feasibility of a passive photon converter in the Mu3e phase I experiment has been studied in [49] using a GEANT4 simulation. In the studied design the converter consists of 0.1 mm gold and the e^+e^- pair is reconstructed in a two-layer HVMAPS spectrometer with a pixel size of 80 μm. For photons with energy $E_\gamma = 53\,\text{MeV}$, a resolution of about 250 keV (peak) was found, to be compared with the in average 220 keV energy loss of a single MIP in 0.1 mm gold. A significant contribution to the uncertainty comes from the unknown position of the conversion point and the therefore unknown path length of the e^+e^- pair in the converter material. Also energy straggling significantly contributes to the energy resolution which is more severe for large Z materials due to the larger possible energy transfer in collisions.

Both contributions to the energy resolution can be significantly reduced if thick silicon sensors are used as active converter which measures directly the energy loss in the depleted region. To make this concept work the sensor should be thick and the depleted

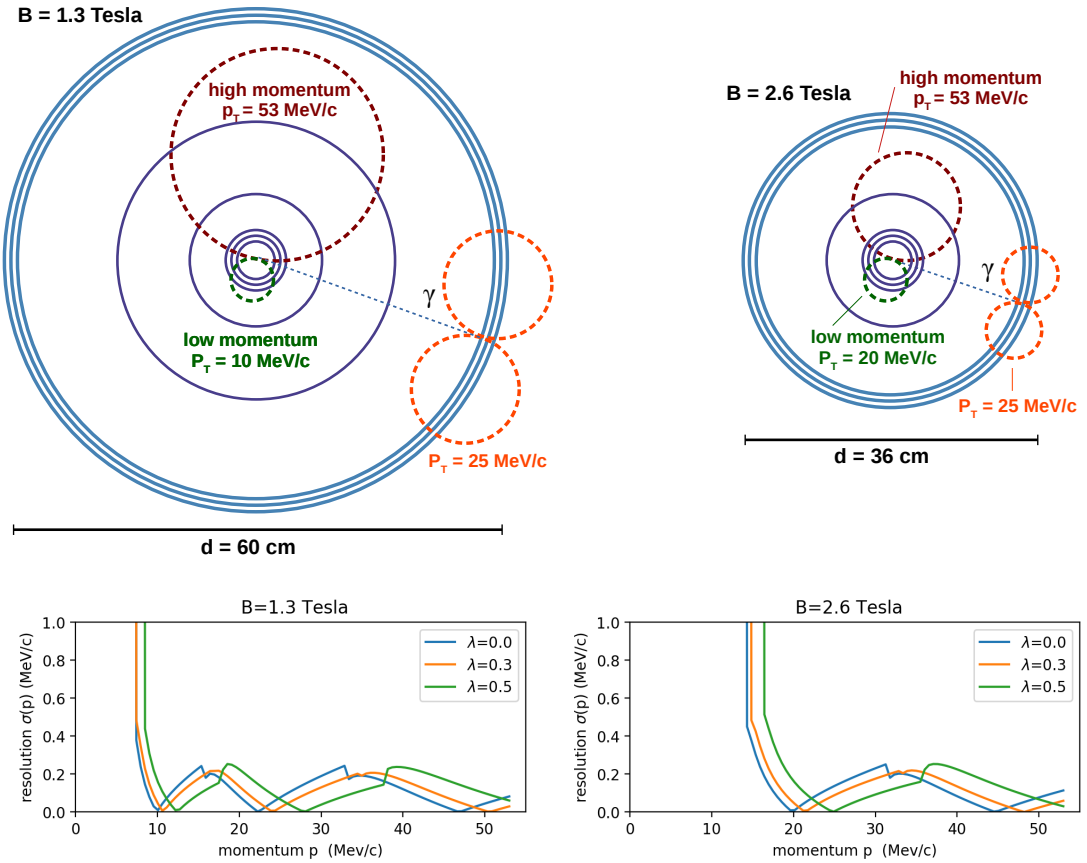

Figure 7: Transverse cross sections of conceptual Mu3e-γ designs (top) and calculated momentum resolution of charged particles from the muon decays as function of the momentum for three example elevation angles λ (bottom). The designs are optimised for the detection of $\mu^+ \to e^+\gamma$ for a solenoid field of $B = 1.3\,\mathrm{T}$ (left) and $B = 2.6\,\mathrm{T}$ (right). Photons are detected in a dedicated three-layer active converter pixel spectrometer which measures the ionisation loss of the e^+e^- pair in silicon. See text for more details.

region which is relevant for charge collection should be large. A charge collection region of about $600\,\mu$m can be achieved if a high ohmic substrate (e.g. $\gtrsim 15\,\mathrm{k\Omega cm}$) is depleted at about 200 V. Using three such active converter layers results in a total radiation length of about 2%. The resulting photon conversion (detection) efficiency is on one hand much smaller than for photon calorimeters, on the other hand such a detector provides and excellent photon energy resolution of about 100 keV, more than an order of magnitude better than the upgraded MEG II xenon calorimeter. For not too small pixel sizes the active converter serves as spectrometer for the reconstruction of the e^+e^- without the need of any additional tracking detectors, thus largely simplifying the design.

Two possible designs of a Mu3e detector combined with a three-layer active converter pixel spectrometer are shown in Figure 7 (Mu3e-γ). The designs are optimised for different solenoid fields and provide an excellent momentum resolution of about $\sigma_p \lesssim$

$250\,\mathrm{keV}/c$ over a large momentum range. This is achieved by choosing a spacing of the tracking layers that ensures that for all particle momenta at least one section of the track (a section is defined between two detection layers) approximately fulfils the condition of a half turn where the multiple scattering uncertainty on the track momentum vanishes, see discussion in [44]. Because of the excellent momentum resolution of the Mu3e-γ designs, this concept is very well suited for a combined search of $\mu^+ \to e^+e^+e^-$ and $\mu^+ \to e^+\gamma$.

The $B = 1.3\,\mathrm{T}$ design in Figure 7 is optimised to provide a large kinematic acceptance[5] ($p_T \gtrsim 8\,\mathrm{MeV}/c$). With such a design even very exotic processes like $\mu \to eeeee\nu\nu$ can be detected with good efficiency. This design requires the instrumentation of large detector areas with pixel sensors which is costly and creates a high power consumption. The instrumented areas are almost a factor two smaller for the $B = 2.6\,\mathrm{T}$ design, however for the price of a smaller kinematic acceptance ($p_T \gtrsim 15\,\mathrm{MeV}/c$). The larger solenoid field has also the advantage of better muon beam focusing which leads to an increase of the muon stopping rate of almost a factor 2 compared to the $B = 1.3\,\mathrm{T}$ design, see the discussion in Section 2.2.1.

In all designs, charged particles from the muon decays remain inside a radius of $r \leq 26\,\mathrm{cm}$ and cannot reach the active converter pixel spectrometer. The BG rate for photon detection is therefore very small, thus making it together with the excellent photon energy resolution a promising instrument to search for $\mu \to e^+\gamma$ or any other decay involving photons in the final state. Examples are the search for exotic LFV decays such as $\mu^+ \to e^+X\gamma$ with X being a pseudo-scalar axion, and the search for dark photons $\mu^+ \to e^+\nu_e\bar{\nu_\mu}A'$ with A' being a long living dark photon which weakly mixes with SM particles and decays in flight $A' \to e^+e^-$ after a few picoseconds.

For the $\mu \to e^+\gamma$ search an excellent timing resolution is crucial. This could be achieved by using a dedicated timing layer in one of the inner three pixel layers for measuring the e^+ timing and by integrating a $\sigma_t \lesssim 100\,\mathrm{ps}$ time-to-digital converter (TDC) in the active converter pixel layers. For monolithic silicon pixel detectors time resolutions of $\mathcal{O}(100\,\mathrm{ps})$ have only been achieved with small prototypes, so far [39]. If such a time resolution can be achieved on a large scale chip in a large scale tracker system will be an important research topic for the coming years. Alternatively, a dedicated timing detector (e.g. scintillator) could be added in front to the converter station[6] to measure the photon timing.

2.3 $\mu \to e\gamma$

2.3.1 General introduction

The state-of-the-art of the $\mu^+ \to e^+\gamma$ search is represented by the MEG II experiment [25] at PSI.

The best current upper limit on the BR of the $\mu^+ \to e^+\gamma$ decay has been set by the MEG experiment at PSI as $\mathrm{BR}(\mu \to e\gamma) < 4.2 \cdot 10^{-13}$ [23]. An upgrade of the

[5] Assuming standalone tracking in the three innermost pixel layers.

[6] The timing layer would measure the time of the e^+e^- pair after a half turn.

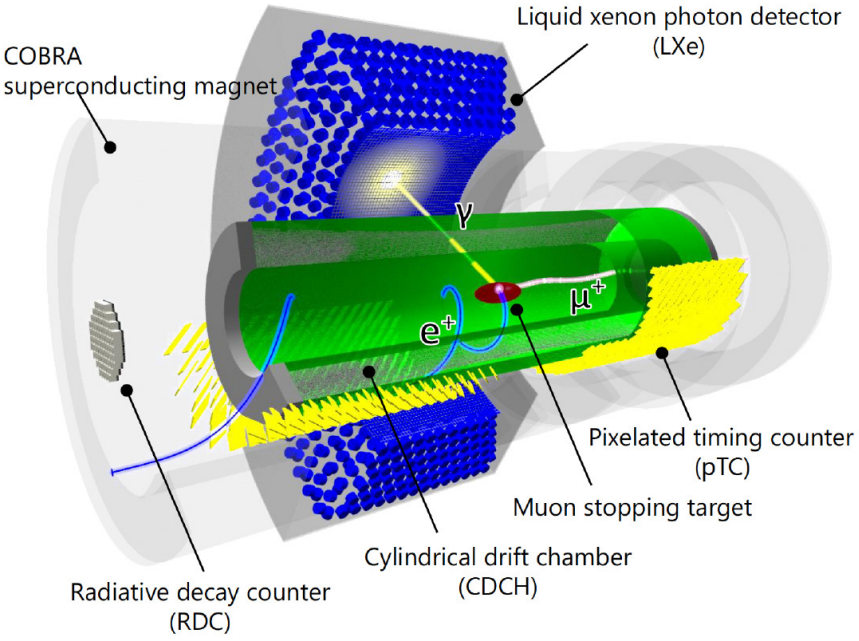

Figure 8: A sketch of the MEG II experiment with all the key elements.

experiment to MEG II has been carried out. MEG II preserves the concept of the previous experiment while improving the detector performances roughly by a factor 2 for all the kinematic variables and aiming at running up to $7 \cdot 10^7 \mu^+/\text{s}$. The expected final sensitivity is $\text{BR}(\mu \to e\gamma) = 6 \cdot 10^{-14}$ for a data-taking period of 3 years. The MEG II experiment has successfully completed its engineering phase and it has just entered into the physics run mode (run2021). For all technical aspects we refer to the most recent document [50].

The signature of a $\mu^+ \to e^+\gamma$ decay at rest is a back-to-back, mono-energetic, time coincident γ and e^+. There are two main BG sources, the dominant being the accidental coincidences between a high-energy positron from the principal decay $\mu^+ \to e^+\nu\overline{\nu}$ (Michel decay) and a high-energy photon from positron annihilation-in-flight or bremsstrahlung or from the radiative muon decay (RMD) $\mu^+ \to e^+\nu\overline{\nu}\gamma$. The other source comes from the RMD itself, when neutrinos take off only a small amount of energy.

In MEG II, positive surface muons with a momentum of 28 MeV/c are stopped in a thin slanted polyethylene target (thickness 140 μm; angle 15 deg), located at the centre of the apparatus.

All kinematic variables of the γ (energy E_γ, time t_γ and interaction point X_γ) are measured using a liquid xenon (LXe) calorimeter. All kinematic variables of the e^+ are measured with a spectrometer made of a cylindrical drift chamber (CDCH) combined with plastic scintillators coupled to silicon photomultiplier (SiPM) - the so-called pixelated timing counter mounted inside a gradient magnetic field. The performance of the

Table 1: Comparison of the e^+ and γ kinematic variable resolutions (in σ) with the MEG (measured) and MEG II (expected) apparatus.

	MEG	MEGII
E_e(core) [keV]	306	130
θ_e(core) [mrad]	9.4	5.3
ϕ_e (core) [mrad]	8.7	3.7
t_e [ps]	70	35
u_γ [mm]	5	2.4
v_γ[mm]	5	2.2
w_γ [mm]	6	3.1
E_γ (w $<$ 2 cm) [%]	2.4	1.1
E_γ (w $>$ 2 cm) [%]	1.7	1.0
t_γ [ps]	67	60
$t_{e\gamma}$ [ps]	122	84
Tracking efficiency [%]	65	78
CDCH-pTC matching efficiency [%]	45	90
Gamma efficiency [%]	63	69
Trigger efficiency [%]	99	99

experiment is continuously monitored by a variety of calibration methods. All signals are recorded with custom designed waveform digitisers up to 5 Gsample/s with the DRS4 chip. A flexible trigger system allows to select $\mu^+ \to e^+\gamma$ candidate events together with pre-scaled calibration data.

A sketch of the MEG II experiment with all the key elements is shown in Figure 8. Table 1 summarises the performances of MEG (measured) and MEG II (expected).

Pushing down the sensitivity of the $\mu^+ \to e^+\gamma$ search requires both beam rate increase and improved background rejection capability. The SES scales as

$$\mathrm{SES} = \frac{1}{R \cdot T \cdot A \cdot \epsilon}\,, \tag{2.2}$$

where R is the beam rate, T is the acquisition time, A is the geometrical acceptance and ϵ the product of all the efficiencies (detection efficiency, selection efficiency, etc.).

The BR of the accidental BG B_{acc} scales as

$$B_{acc} = R \cdot \Delta E_e \cdot (\Delta E_\gamma)^2 \cdot \Delta T_{e\gamma} \cdot (\Delta \Theta_{e\gamma})^2\,, \tag{2.3}$$

where ΔE_e, ΔE_γ, $\Delta T_{e\gamma}$ and $\Delta \Theta_{e\gamma}$ are the positron energy, gamma energy, relative positron and gamma timing and relative positron and gamma angle resolutions.

These formulas suggest that, given a very good detector geometrical acceptance and detector efficiency, the most effective parameter to improve sensitivity is the beam rate. On the other hand the BR of the accidental BG – the dominant BG – increases linearly

with the beam rate. In order to really benefit from a beam-rate increase therefore relies on detectors able to simultaneously sustain higher beam intensity and provide better kinematic variable resolutions.

While the measurement of the positron kinematic variables is conceptually delineated and the spectrometer option is the most competitive one, leaving just room for the specific technology to be selected, the measurement of the gamma kinematic variables is in principle open to two different approaches: either detecting the gamma directly via a calorimeter or converting it into an electron-positron pair and then measuring it via a spectrometer.

The calorimeter option offers a higher detection efficiency compared to the conversion one. Nonetheless, the latter could be the favourite choice at a very high beam rate in order to keep the BG under control, due to the better kinematic resolutions. The capability of sustaining a higher beam rate compensates for the drop in terms of efficiency. The best option as a function of the beam rate is defined by the BG regime. Figure 9 shows it in a schematic way.

In the next sections the different experimental approaches summarised in Figure 10 will be presented. While a calorimeter with improved performance could still be appealing, based on the current and foreseen technologies external photon conversion seems to be more promising at very high beam intensities, as expected with HIMB. Photon conversion can be further improved if complemented with an active target.

2.3.2 Gaseous positron tracker

A precise reconstruction of the kinematics of 52.8 MeV/c positrons can only be achieved with a very light tracker in a magnetic field. Indeed, at such low momentum, the contribution of the multiple Coulomb scattering to the tracking resolutions tends to become dominant, so that an extremely good position resolution is not necessary if it is compensated by a reduced material budget. Despite the rapid evolution of ultra-thin silicon detectors, this aspect makes gaseous detectors still competitive for this application.

The state of the art is represented by the CDCH of the MEG II experiment [51]. With a gas mixture of helium and isobutane in 90:10 volume concentrations and cells made of 20 μm gold-plated tungsten sense wires and 50 μm silver-plated aluminium field wires, with a minimum cell size of 3.5×3.5 mm^2 and a full-stereo geometry, this detector is designed to provide 100 μm single-hit resolution in the plane transverse to the beam axis, with an average radiation length of about 350 m. The resulting momentum and angular resolutions are expected to be around 100 keV and 5 mrad, respectively. In consideration of the technical difficulties for building a chamber with thinner wires, and the intrinsic limitations to the achievable single-hit resolution in a drift chamber, we cannot expect any dramatic improvement of these performances, although there are proposals to refine the track reconstruction exploiting the detection of single ionisation clusters [52] and to use carbon monofilaments to build wires with reduced density [53].

For these reasons, in terms of performances, the MEG II CDCH can be considered the benchmark for the next generation of gaseous trackers for $\mu \to e\gamma$. There is anyway a strong limitation to the use of such a kind of detector at beam intensities much higher

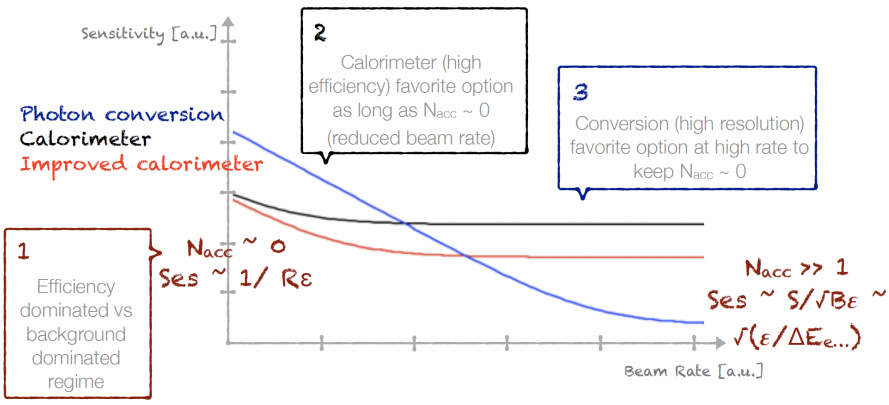

Figure 9: A sketch of the sensitivity as a function of the beam rate for three different scenarios: a) calorimeter (black line) - used as a reference; b) Improved performing calorimeter (red line); c) photon conversion (blue line).

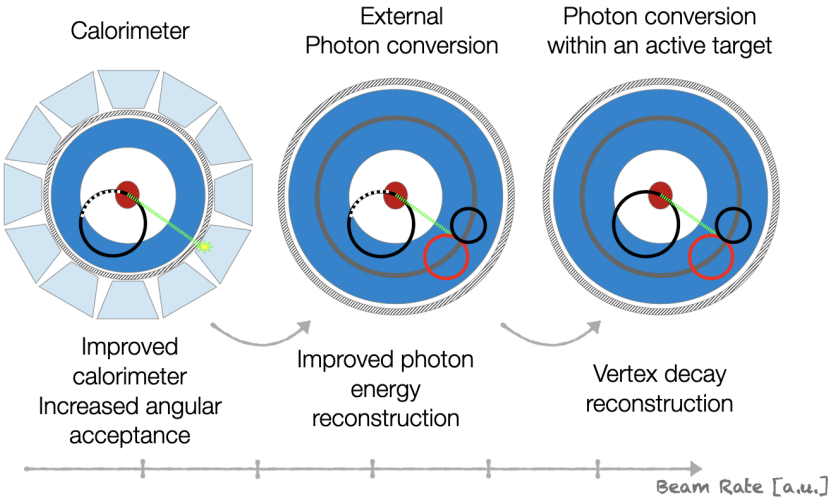

Figure 10: A sketch of the different experimental approaches as a function of the beam rate.

than 10^8 μ/s: the MEG II CDCH is expected to undergo a 25% gain loss per year in the inner and most illuminated region at 7×10^7 μ/s, due to wire ageing effects [25]. While in MEG II an increase of the sense wire voltage can be applied to compensate for this loss, with a much higher beam intensity the ageing rate would clearly become unmanageable.

As a possible solution, a radical change in the geometry of the drift chamber, with wires lying in planes transverse to the beam axis, would reduce the positron rate per unit length in the inner wires, so suppressing the ageing rate by a factor of about 10. This design requires the wire support structures and the readout electronics to be distributed in between the tracker and the outer detectors (positron timing and photon detectors), whose performances could deteriorate by the consequently higher material budget.

As an alternative approach, the replacement of the drift chamber with a time projection chamber (TPC) can be considered, so to strongly reduce the material budget (thanks to the absence of wires in the tracking volume) and exploit the high particle flow capabilities of modern TPCs readout by micro-pattern gaseous detectors (MPGDs). The typical geometry of a $\mu \to e\gamma$ experiment requires anyway a relatively long detector along the beam axis (2 m for the MEG II CDCH). If a conventional TPC is used, with the electrons drifting along the beam axis, the deterioration of the longitudinal position resolution due to the electron diffusion would spoil the detector performances. Moreover, simulations show that the current density in the readout detector and the space charge density in the tracking volume would be prohibitive also with the most advanced MPGDs. We considered, as a possible alternative, a radial TPC, i.e. with electrons drifting radially, toward the external surface of the cylindrical detector. This surface could be instrumented with a cylindrical MPGD (e.g. a cylindrical GEM [54] or μRWell [55]). The shorter drift distance would allow to reduce the readout current and space charge densities, down to values that are comparable with the ones expected in the GEM-TPC of the upgraded ALICE experiment [56]. It supports the feasibility of such a solution, although big challenges need to be faced. Beside the ones already experienced in ALICE, there is the specific need of keeping the material budget on the external surface of the detector very low, which would require a dedicated effort to integrate the front-end electronics with its cooling in the structure of the readout MPGD.

2.3.3 Photon calorimeter

The photon measurement is the most difficult and crucial part of the $\mu \to e\gamma$ experiment. A significant improvement of the photon detector performance would be a key to higher sensitivities of future $\mu \to e\gamma$ experiments. Photon measurements with a LXe scintillation detector have been carried out in the MEG/MEG II experiment. This calorimetric approach has been nicely working with the muon beam intensity up to 7×10^7 μ/s in the MEG II experiment. The performance of the calorimeter would, however, be limited at higher beam intensities above 10^8 μ/s foreseen at future $\mu \to e\gamma$ experiments aiming at $\mathcal{O}(10^{-15})$ sensitivity.

The challenges for new calorimetry for incoming experiments at the intensity frontier is to provide detectors with ultra-precise time resolution and supreme energy resolution. Two very promising materials on the market are BrilLanCe (cerium doped lanthanum bromide, $LaBr_3$(Ce)) and Lutetium–Yttrium oxyorthosilicate (LYSO) $Lu_{2(1-x)}Y_{2x}SiO_5$(Ce), supported by recent developments aiming at providing relatively large crystals.

Cerium doped lanthanum bromide stands out due to its ultra-high light yield (1.65 $\times$ NaI(Tl)) and by a more than an order of magnitude faster decay time compared to NaI(Tl). With these properties together with its high density, $LaBr_3$(Ce) is the ideal medium for calorimetry limited only by the currently available crystal sizes on the market.

Due to recent developments, larger crystals up to a radius $R = 4.45\,\text{cm}$ and a length $L = 20.3\,\text{cm}$ can be produced commercially. A calorimeter built from such a large

Table 2: Main scintillation properties for widely used scintillating media. A F.o.M. is given as defined in the text.

Scintillator	Density ρ (g/cm^3)	Light yield LY (ph/keV)	Decay time τ (ns)	F.o.M. $\sqrt{\tau/(\rho \cdot \mathrm{LY})}$
$LaBr_3$(Ce)	5.08	63	16	0.22
LYSO	7.1	27	41	0.46
YAP	5.35	22	26	0.47
LXe	2.89	40	45	0.62
NaI(Tl)	3.67	38	250	1.34
BGO	7.13	9	300	2.16

crystal is a potential candidate for the detection of photons at energies from few tens up one hundred MeV. This corresponds to the interesting energy range of current cLFV experiments. Thus $LaBr_3$(Ce) may be a suitable candidate for future experiments in this sector.

LYSO on the other hand exhibits a very high density, comparable to BGO and thus features short radiation length X_0 and Molière radius R_M. Despite the fact that the light yield is only roughly 70 % of NaI and the decay time roughly three times longer compared to $LaBr_3$(Ce), its density makes LYSO an attractive candidate as well, especially considering that the available crystal size is one of the limiting factors.

Table 2 summarises the main scintillation properties compared to the widely used scintillation media. For a quick comparison a figure of merit (F.o.M.) is defined as the square root of the ratio of the scintillation decay time τ and the product of the light yield (LY) and the density ρ.

The result is a detector with a high photosensor granularity, high rate sustainability, maximal photosensor coverage area, optimal geometrical acceptance and insensitivity to magnetic fields. Due to the small thickness of modern photosensors of a few mm, even the radiation impinging area can be covered with minimal impact on photons passing through. This feature allows for a double readout scheme, where the multi-pixel photon counters (MPPCs) are mounted also on the front/entrance face. The smaller the MPPC pixel size the smaller the saturation effect. In addition, the granularity due to the MPPCs allows some geometrical reconstruction of the event. A sketch of a detector assembly is shown in Figure 11.

Figure 12 shows the results obtained with different crystal sizes of both $LaBr_3$(Ce) and LYSO up to the so-called ultimate dimension, not yet available on the market. The detectors are exposed to 55 MeV gammas impinging on the entrance face. Two types of MPPC were selected to be used as a model in the simulation: Hamamatsu S13360-6025PE and sensL MicroFj-60035TSV. For crystals of 15 cm diameter and 20 cm and 16 cm of length for $LaBr_3$(Ce) and LYSO respectively, an energy resolution up to around 1% for $LaBr_3$(Ce) and 0.4% for LYSO is obtained. In order for $LaBr_3$(Ce) to fully benefit from its higher light yield, one has to go for even larger crystals of about 40 cm diameter. In such a configuration, resolutions around 0.3% and better has been

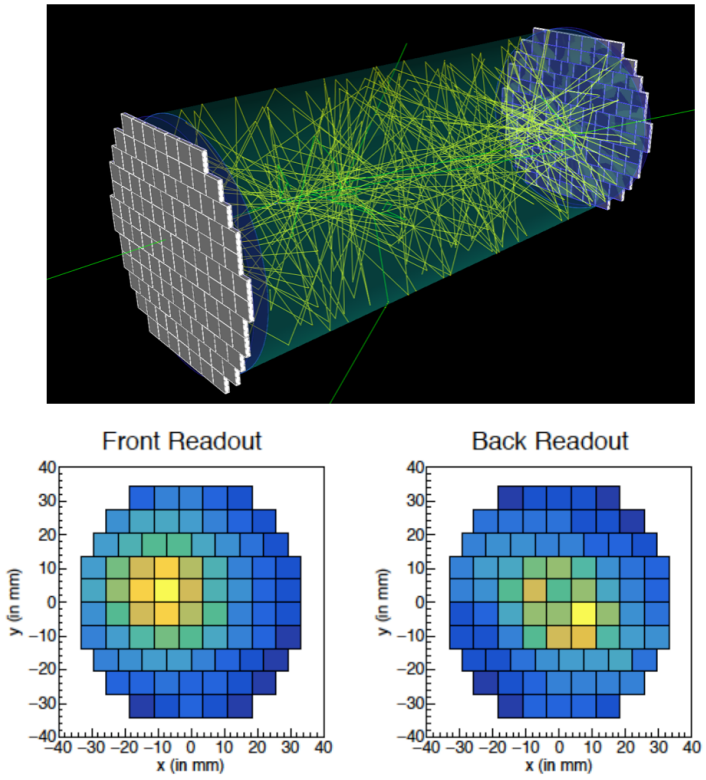

Figure 11: A sketch of the scintillation light distribution associated to a 55 MeV gamma event impinging on (R=3.5 cm, L=16 cm) LYSO crystal coupled to Hamamatsu S13360-6025PE MPPCs (top) and the typical collected charge distribution on the front and back face (bottom).

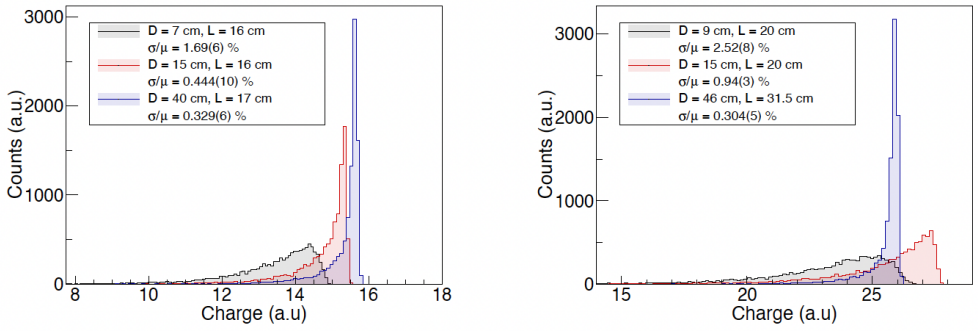

(a) LYSO Crystals

(b) $LaBr_3$:Ce Crystals

Figure 12: Energy resolution for different crystal sizes, where σ and μ are the standard deviation and the mean . "Available" crystals are shown in black, "Large" sized crystals in red and the "Ultimate" crystals in blue.

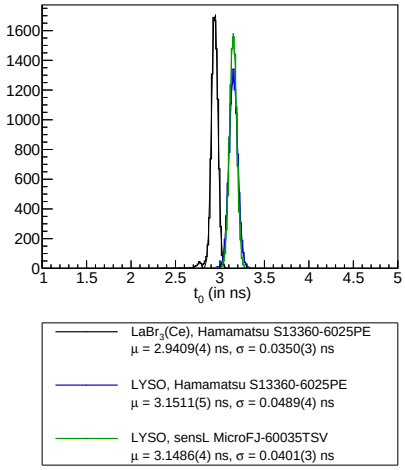

Figure 13: Timing resolutions for the available (R=4.45 cm, L=20.32 cm) $LaBr_3$(Ce) and (R=3.5 cm, L=16 cm) LYSO crystals. Here the $LaBr_3$(Ce) is coupled to the Hamamatsu S13360-6025PE. For the LYSO both MPPC options (Hamamatsu S13360-6025PE and sensL MicroFJ-60035TSV) are displayed.

quoted also for the $LaBr_3$(Ce).

Examples of time distributions are shown in Figure 13. Timing resolutions below 50 ps are in the reach. The Monte-Carlo simulations are based on the Geant4 libraries with dedicated code that includes the MPPC response and the whole electronic chain up to the DAQ, based on waveform digitisers with a sampling frequency up to 5 GSample/s. The reconstructed algorithms are based on waveform analysis. The simulations are supported by measurements done with available LaBr3(Ce) crystals with sizes of (R=3.81 cm, L=7.62 cm) and (R=1.27 cm, L=10.16 cm) coupled to either photomultiplier tubes or MPPCs and the characterisation of the MPPC response.

In conclusion, new detectors have been considered here based on either large LaBr3(Ce) or LYSO crystals coupled to MPPCs showing very promising results for high-energy $\mathcal{O}(50)$ MeV photon calorimetry. Independent of the specific detector assembly, simultaneous energy, timing and position resolutions below 0.5 MeV, 50 ps and a few mm appear to be feasible. Such results put this new calorimetry at the detector forefront for particle physics research at beam intensity frontiers.

2.3.4 Photon conversion spectrometer

Photon measurements based on a pair conversion spectrometer would be an alternative and viable option with several advantages over the calorimetric approach with higher beam intensity. In the pair conversion spectrometer, the incident photon is converted to an electron-positron pair in a thin converter and the conversion pair is then measured with a tracker. More precise measurements of the energy and position as well as higher rate capabilities are expected. In addition, the photon direction can be measured with

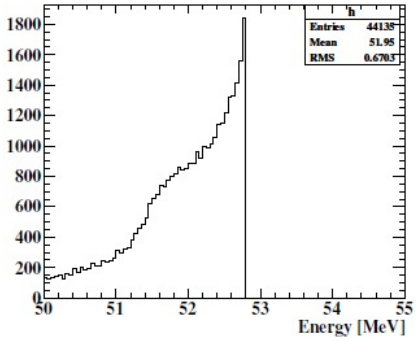

Figure 14: Energy sum distribution of the conversion pair emitted from 560 μm thick lead converter with signal photon injection.

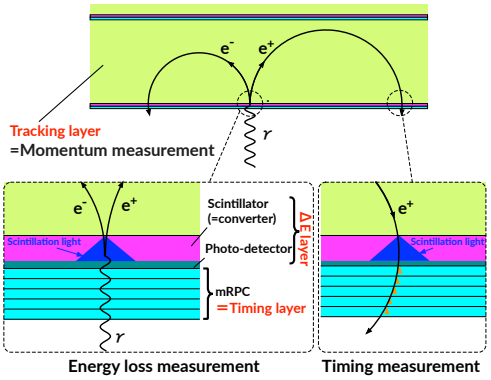

Figure 15: Possible structure of the active conversion spectrometer.

the conversion spectrometer since the emission of the conversion pair is highly boosted along the incident photon direction. This would provide a possibility to further reduce the accidental background together with a widely spread distribution of the stopping muon. It must be noted that the precise measurement of the photon direction is not possible with the calorimetric approach. On the other hand, a major challenge for the conversion spectrometer is the low detection efficiency due to the low conversion efficiency with a thin conversion layer. It can be mitigated to some extent with multiple conversion layers. The pair spectrometer was employed in the previous $\mu \to e\gamma$ experiment, MEGA (1985–1999)[57]. It consisted of three photon conversion layers, each of which was based on two 250 μm thick lead converters, with the overall detection efficiency of 5%. The signal statistics can be improved by increasing the beam intensity, limited by the rate capability of the detectors.

Another crucial limiting factor of the conversion spectrometer is the energy loss of the conversion pair inside the converter. Figure 14 shows the simulated result for the energy sum of the conversion pair emitted from a 560 μm thick lead converter with signal photon injection, where a significant tail due to the energy loss in the converter can be seen. This leads to an inefficiency for the signal photon and/or deterioration of the energy resolution.

It is proposed here to use a so-called "active converter" where the energy loss of the conversion pair in the converter is measured by the converter itself. Figure 15 shows a possible structure of the conversion spectrometer composed of an active converter, a tracking layer, and a timing layer. The incident photon is converted in the active converter layer which measures the energy loss of the conversion pair in the converter. The possible technology for the active converter is a scintillator coupled with a photo-detector or silicon detector. The tracks of the conversion pair are measured in the tracking layer. It is not a harsh environment since the Michel positrons do not reach the conversion spectrometer placed outside the positron spectrometer in the proposed design

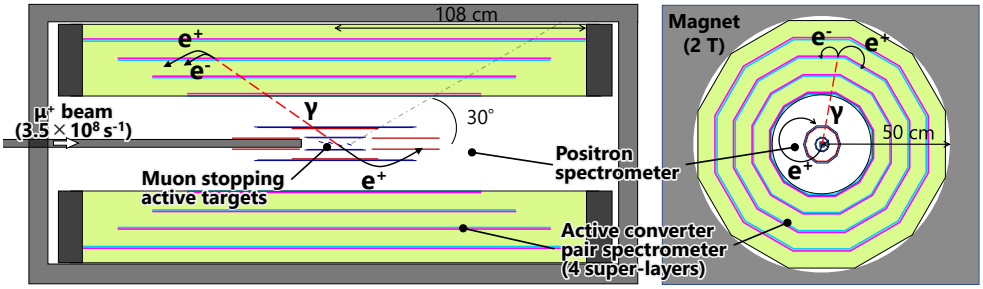

Figure 16: Possible layout of $\mu \to e\gamma$ experiment with photon conversion spectrometer.

as shown later. A gaseous detector such as a drift chamber or a TPC can therefore be used as a tracker, although thin silicon detectors can be an attractive candidate technology as well. The timing layer placed in front of the active converter measures the timing of the returning conversion pair, with which the photon timing can be extracted after correcting for the time-of-flight of the conversion pair. The timing layer is required to be low-mass to avoid the photon conversion before the active converter, although it can basically be vetoed by placing a thin scintillator layer between the active converter and the timing layer. The use of multi-layer resistive plate chamber detectors is considered as a candidate technology. The timing can also be measured by the active converter if its timing resolution is good enough.

Figure 16 shows a possible layout of the $\mu \to e\gamma$ experiment with the photon conversion spectrometer. The photon spectrometer with four layers of the active converters is placed outside the positron spectrometer. Silicon detectors are envisaged as a technology option for the positron spectrometer because of their high rate capability. The design of the positron spectrometer is inspired by the Mu3e detector, which would provide a possibility of a concurrent search for $\mu \to eee$ in this setup. One of the most important improvements in the experimental design compared to the MEG II experiment is the enhanced signal acceptance especially for the zenith angle, which is $\pm 60^\circ$, while it is $\pm 20^\circ$ for the MEG II experiment. The enhanced zenith-angle acceptance would enable us to measure the angular distribution of $\mu \to e\gamma$ with polarised muon beam after a possible discovery of $\mu \to e\gamma$ decay in the MEG II experiment. Together with the measurement of the BR, we could pin-down the underlying new physics behind $\mu \to e\gamma$.

The materials for the active converter are being investigated from the viewpoint of the expected performance of the active converter such as conversion efficiency and the detector resolutions. One of the crucial parameters is the critical energy, above which the energy loss by bremsstrahlung dominates over ionisation energy loss. Since the active converter can basically measure the ionisation energy loss only, the critical energy should ideally be higher than the energies of the conversion pair, which range from 0 to 52.8 MeV. The critical energy is known to have an empirical dependence on the atomic number as $610\,\mathrm{MeV}/(Z + 1.24)$ [58]. The critical energies of LYSO and YAP as good candidates for scintillator materials from the viewpoint of the detection efficiency are 12 MeV and 23 MeV, respectively, which are not sufficiently high compared to the ener-

gies of the conversion pair. On the other hand, the critical energy for plastic scintillator, which is not ideal from the viewpoint of the detection efficiency, is 93 MeV and thus sufficiently high. The comparison among the candidate materials is not straightforward since some part of the energy loss by bremsstrahlung can be absorbed and measured by the converter. Simulation studies are in progress to compare the performance of different materials as the active converter. The energy loss measurement can be ruined when the returning conversion pair hits the converter. A segmentation of the scintillator into cells is therefore required for the active converter.

The gaseous photo multiplier tube (Gas PM) and SiPM are under consideration as the photodetector for the scintillator converter. The Gas PM consists of a photocathode and resistive plate chamber (RPC) as electron multiplier. The technology of the ultra-low mass RPC with diamond-like carbon electrodes developed for the MEG II radiative decay counter [59] can be used for the RPC of the Gas PM. The development of the large-area photocathode sensitive to visible scintillation light is, however, extremely challenging. The combination of the vacuum ultraviolet (VUV) scintillator and the CsI photocathode sensitive to VUV light is also under investigation because CsI photocathodes are much easier to handle. The scintillation readout by SiPM is also viable option. A good light collection efficiency and its small position dependence have been already demonstrated by the CALICE scintillator calorimeters [60].

Further studies on the design and the performance of the photon conversion spectrometer are in progress, including detailed simulation studies and prototype tests for the candidate technologies.

2.3.5 Silicon pixel sensor for $\mu \to e\gamma$

With the advent of monolithic silicon pixel sensors, which can be thinned to a few tens of micrometers, silicon detectors became an attractive alternative for tracking low-energy particles, especially for high-rate applications, where gaseous detectors suffer from sparks and ageing effects. Ultra-light mechanical designs combined with gaseous helium cooling of the sensors allow for the construction of silicon tracking layers with a thickness of about 1 per mill of radiation length, as demonstrated by the Mu3e Phase I experiment. A similar design could also be used for precisely measuring the trajectory of the positron in the $\mu \to e\gamma$ search. Since positrons from this decay are mono-energetic a further optimisation of the Mu3e spectrometer can be done and applied to MEG to achieve a momentum resolution of about 100 keV/c. This optimisation aims at detecting the decay positrons after curling half a turn (180° in the solenoid field). This can be achieved by operating the Mu3e pixel detector in a magnetic field of about 2.5 T (instead of 1.0 T) or by increasing the radius of the outer pixel layer with respect to the Mu3e phase I design. In order to fully profit from the high rate capability of the silicon detector technology (in terms of radiation hardness) the sensor is required to provide a very good time resolution as well. The HVMAPS sensor used for the Mu3e phase I experiment has a time resolution of about 5 ns and would perfectly fulfil the requirements of a $\mu \to e\gamma$ search at HIMB. For the $\mu \to e\gamma$ search the first tracking layer must be as thin as possible in terms of radiation length. The thinner the sensor the less multiple scattering

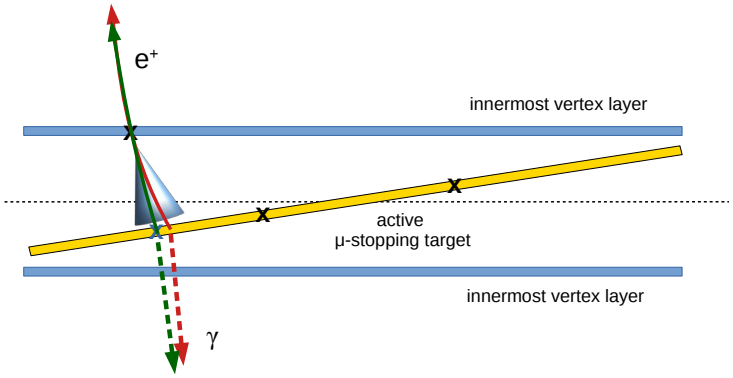

Figure 17: Sketch of the active muon stopping target concept for the reconstruction of $\mu \to e\gamma$ events. Extrapolated positron tracks are assigned to hits (muon decay) in the active target to improve the vertex information (direction of the positron and photon).

affects the measurement of the initial positron direction, which is derived from the hit positions in the first two tracking layers and is crucial for the topological BG rejection (back-to-back signature of signal).

The experimentally proven radiation hardness of the high-voltage complementary metal-oxide-semiconductor process [61] also allows to use HVMAPS for beam monitoring applications and the usage as active muon stopping target such that the muon decay position is directly measured. The achievable resolution is a few tens of microns and much smaller than the uncertainty of a few hundreds of micrometer by extrapolating the reconstructed positron trajectory back to the muon stopping target, see Figure 17. By directly measuring the muon decay vertex, the direction of the signal positrons and photons can be more precisely determined and BG not exhibiting the back-to-back topology can be more efficiently suppressed. This concept, however, only works if the active muon stopping target is not too thick since multiple scattering inside the material would otherwise compromise the measurement of the positron direction. Studies are ongoing where the signal response of thinned HVMAPS is measured and a small reduction of the hit detection efficiency has been observed with the MuPix10 sensor for substrate thickness below $50\,\mu$m. This efficiency loss, however, might be recovered with an improved amplifier design in future sensor versions. Furthermore, in order to make this concept viable, the density of muon stops must not be too high as otherwise ambiguities in the matching of positron tracks with the muon decay positrons will reduce the track linking efficiency. This requirement defines a limit on the maximum muon stop rate, depending on the maximum distance (radius) of the first tracking layer and the thickness of the first tracking layer in case of a silicon tracker.

The possibility to implement an active conversion target (see Section 2.3.4) in a depleted silicon detector as photon detector was already discussed in the context of a combined Mu3e-MEG experiment in Section 2.2.6. A sketch of such a detector is shown in Figure 18. Photons with an energy $\gtrsim 10\,\text{MeV}$ convert in the sensor material and

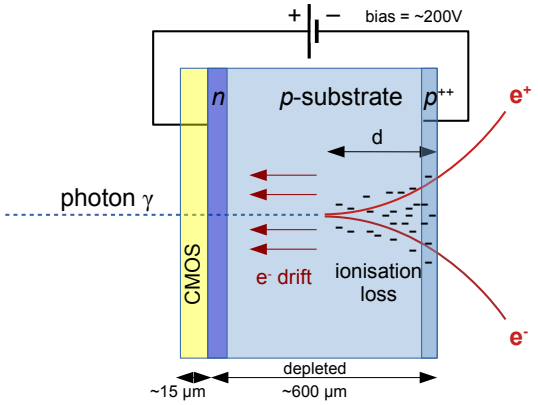

Figure 18: Sketch of an active converter silicon sensor implemented as HVMAPS. The ionisation loss is proportional to the measured signal amplitude. The active zone where the charge (electrons) is collected is about 40 times larger than the inactive zone where the CMOS circuits are placed for readout.

create an e^+e^- pair which undergoes ionisation loss. Electron-hole pairs are produced in the silicon. The electrons drift to the anode (n-well) and are registered by the readout circuitry which is implemented in CMOS. An interesting feature of this concept is that the active converter can also be used as high precision e^+e^- spectrometer if the pixel size is not too large. The goal is to reach an energy resolution of about $\sigma_E \approx 100\,\text{keV}$ for 53 MeV photons.

For the development of the active converter pixel sensor the following challenges need to be tackled. Assuming a substrate resistivity of about $\gtrsim 15\,\text{k}\Omega\text{cm}$ a depletion voltage of about 200 V is required to fully deplete 600 μm of silicon. The pixel and guard-ring design must therefore allow for a breakdown voltage $\geq 200\,\text{V}$. The pixel size should not be larger than 150 μm for the $B = 2\,\text{T}$ setup so that spatial hit uncertainties do not deteriorate the momentum resolution. The pixel sensor circuitry has to provide a time resolution of $\sigma_t \lesssim 100\,\text{ps}$. The TDC and the readout electronics has to be capable to provide a time resolution of a $\sigma_t \lesssim 100\,\text{ps}$. The amplitude of the signal should be measured with a relative accuracy of 10% or better. Furthermore all active converter layers must not have any significant amount of support material, making the detector design very challenging. Significant R&D effort will be required to realise such an active converter pixel sensor.

In summary, monolithic silicon detectors are a very promising detector technology for search for $\mu \to e\gamma$. They provide excellent tracking in a high-rate experiment at HIMB and can also be used as active muon stopping target and active photon converter.

2.4 Muon moments

Measurements of magnetic and electric dipole moments have historically provided unique insights into new physics as well as stringent tests of the SM. There is huge potential for

a future muon $(g-2)$ experiment at PSI, using re-accelerated muons from a new low-energy, high-brightness source (muCool) coupled to the future HIMB. This complements ongoing efforts at Fermilab and J-PARC, potentially further increasing the precision. Similarly, there is potential to improve the sensitivity of a search for a muon EDM to better than 1×10^{-23} ecm. A null result sets a stringent limit on a currently poorly constrained Wilson coefficient and a discovery of a muon EDM would prove the existence of physics beyond the SM.

2.4.1 $g-2$ and muon electric dipole moment

The AMM of the electron and muon have a long tradition as precision tests of the SM, going back to Schwinger's famous prediction $a_\ell = (g-2)_\ell/2 = \alpha/(2\pi)$ [62, 63]. For the electron, the precision at which SM prediction and direct measurement can be confronted is approaching 10^{-13}, with [64]

$$a_e^{\text{exp}} = 1\,159\,652\,180.73(28) \times 10^{-12}. \tag{2.4}$$

Regarding the SM prediction, the mass-independent 4-loop QED coefficient is known semi-analytically [65], so that the dominant uncertainties, both at the level of 10^{-14}, arise from the numerical evaluation of the 5-loop coefficient [66] and hadronic contributions [67].[7] The present limiting factor thus concerns independent input for the fine-structure constant α, with the current most precise measurements in atom interferometry [69, 70] differing by 5.4σ,

$$\begin{aligned} a_e^{\text{SM}}[\text{Cs}] &= 1\,159\,652\,181.61(23) \times 10^{-12}, \\ a_e^{\text{SM}}[\text{Rb}] &= 1\,159\,652\,180.25(10) \times 10^{-12}, \end{aligned} \tag{2.5}$$

i.e., 2.5σ above and 1.6σ below (2.4), respectively.

The value for the muon provides an intriguing hint of new physics given the 4.2σ discrepancy between the theoretical predication and current world's best measurement. The experimental value is

$$a_\mu^{\text{exp}} = 116\,592\,061(41) \times 10^{-11}, \tag{2.6}$$

with a combined precision of 0.35 ppm after averaging the Run-1 result from the Fermilab experiment [12, 71–73] and the Brookhaven measurement [13]. The resulting 4.2σ tension with the SM prediction [14]

$$a_\mu^{\text{SM}} = 116\,591\,810(43) \times 10^{-11} \tag{2.7}$$

will be scrutinised at subsequent runs at Fermilab [74] and at J-PARC [75], with a precision goal of 0.14 ppm and 0.45 ppm, respectively. In particular, the J-PARC experiment will pioneer a new experimental technique that does not rely on the so called "magic

[7] For the 5-loop QED coefficient there is a 4.8σ tension between [66] and [68] in the evaluation of diagrams without closed lepton loops.

momentum" in a storage ring, see also [76], with a set-up similar to the experiment proposed here, see Section 2.4.4.

The uncertainty in the SM prediction (2.7) is completely dominated by hadronic contributions, with hadronic vacuum polarisation (HVP) and hadronic light-by-light scattering (HLbL) at 0.34 ppm and 0.15 ppm producing a total precision of 0.37 ppm. This value reflects the current recommendation from the muon $g-2$ Theory Initiative [14], which is based on major input from [66, 67, 77–94]. While the current precision suffices for the comparison to the precision of the current measured value, further improvements both on HVP and HLbL are required to match the experimental projections, including new $e^+e^- \to$ hadrons data, consolidated lattice-QCD calculations of HVP, and direct input on space-like HVP from the proposed MUonE experiment [95, 96]. A first lattice calculation of HVP at sub-percent precision [97] has been reported recently, indicating a tension with the data-driven determination [98–102]. Other developments include new data for $e^+e^- \to \pi^+\pi^-$ from SND [103] and improved radiative corrections [104]. For HLbL, a recent evaluation in lattice QCD agrees with the phenomenological result at a similar level of precision [105], but the sub-leading contributions to HLbL [106–111] need to be better understood to meet the target precision set by experiment.

The current discrepancy between the measured and theoretical value is larger than the electroweak contribution and so requires some form of enhancement mechanism, but there are several well-motivated examples that provide this. One example concerns new light, weakly coupled models that provide an explanation via the small mass of the new particle [112–119]. Alternatively, solutions with new heavy particles above the electroweak scale are possible if the chirality flip originates from a large coupling to the SM Higgs, instead of the muon Yukawa coupling in the SM, leading to a chiral enhancement that allows for viable solutions for particle masses up to tens of TeV [120–123].

The most-studied theoretical framework of BSM physics above the electroweak scale that can explain $g-2$ of the muon is the MSSM. Here, the necessary chiral enhancement is provided by $\tan\beta \equiv v_u/v_d$, where v_u and v_d are the vacuum expectation values of the two Higgs doublets H_u and H_d, which give mass to up-type and down-type fermions, respectively. A large value of $\tan\beta \approx 50$ is suggested by top–bottom Yukawa coupling unification [124, 125], which can thus provide a natural explanation [126–128].

Another possible explanation, also motivated by the hints for lepton flavour universality violation in semi-leptonic B decays, are leptoquarks. In fact, two scalar leptoquark representations can provide a chiral enhancement factor of $m_t/m_\mu \approx 1600$ [129–134]. This allows for a BSM explanation with perturbative couplings that is not in conflict with direct Large Hadron Collider (LHC) searches. It is furthermore very predictive as it involves only two free couplings whose product is determined by $g-2$. Thus, correlated effects in $h \to \mu^+\mu^-$ [134], and, to a lesser extent, in $Z \to \mu^+\mu^-$ [133, 135] arise.

Alternatively, there exist many heavy BSM explanations such as composite or extra-dimensional models [136–138] or models with vector-like leptons [121, 122, 139–145], including in addition a second Higgs doublet [146–148](2HDM). Note that also a pure 2HDM can provide a solution, either via Barr–Zee diagrams in the 2HDM-X [149–154] or through a lepton-flavour-violating $\tau\mu$ coupling [155–158], which is, however, strongly

constrained from $h \to \tau\mu$ searches.

Unlike the magnetic dipole moment of the muon, the EDM is predicted to be well below the reach of current experiments and so any measurement would be an indication of new physics. In comparison to other EDM bounds [159], the limit on the muon EDM is particularly weak: the current direct limit $d_\mu < 1.5 \times 10^{-19}\,\text{ecm}$ [160] is ten orders of magnitude higher than the one for $d_e < 1.1 \times 10^{-29}\,\text{ecm}$ [161]. One reason for this is that in the past, the muon EDM was often discarded as a valuable BSM probe by rescaling the limits on d_e, assuming minimal flavour violation (MFV) [162–165] (by the ratio m_μ/m_e), with a resulting limit of $d_\mu < 2.3 \times 10^{-27}\,\text{ecm}$, which is orders of magnitude below the direct limit. However, MFV is, at least to some extent, an ad-hoc symmetry imposed to allow for light particle spectra, in particular within the MSSM, where this reduces the degree of fine-tuning in the Higgs sector while respecting at the same time flavour constraints. However, since the LHC did not discover any new particles directly [166, 167], the concept of naturalness is challenged. Furthermore, LHCb, Belle, and BaBar discovered significant tensions in semi-leptonic B decays [168–177] implying a discrepancy significantly above the 5σ-level within a global analysis [178–182]. These hints for BSM physics point towards a significant violation of lepton flavour universality and are therefore not compatible with MFV in the lepton sector [183].

Further, the 4.2σ tension in the muon $g-2$ sets the expected size for the muon EDM if the CP-violating phase in the respective Wilson coefficient is sizeable. That is, even though the value of $g-2$ is not directly related to the EDM, any BSM contribution would result from the real part of the Wilson coefficient whose imaginary part determines the EDM, with an $\mathcal{O}(1)$-phase (in case of a chirally enhanced explanation) leading to a muon EDM of the order of $10^{-22}\,\text{ecm}$. Moreover, while $g-2$ by itself does not conflict the MFV paradigm, solutions with chiral enhancement mentioned above can violate the MFV scaling [122, 139], and particularly in the case of leptoquarks they even must do so, in order to respect the bounds from $\mu \to e\gamma$ [133]. At the same time, such scenarios automatically provide an a priori free phase, leading to a large EDM unless the phase happens to be small.

Therefore, it is well-motivated that the BSM flavour structure goes beyond MFV, a notion sometimes contested on grounds of naturalness arguments. However, this does not mean that a conflict with $\mu \to e\gamma$ arises, as in the limit of vanishing neutrino masses lepton flavour is conserved, and thus it is possible to completely disentangle the muon from the electron EDM. This can even be achieved via a symmetry, such as $L_\mu - L_\tau$ symmetry [184–186], which, even after its breaking, protects the electron EDM and $g-2$ from BSM contributions [142]. Also from an EFT point of view [122, 187, 188], it is clear that the muon EDM can be large and that its measurement is the only way of determining the imaginary part of the associated Wilson coefficient.

For these reasons, both a high-precision measurement of the muon $g-2$ and a dedicated muon EDM experiment are highly motivated, and would be valuable contributions in the search for BSM physics in low-energy precision observables.

2.4.2 A $g-2$ / EDM measurement at PSI

Currently the most precise measurement of the muon $g-2$ is being performed at Fermilab, with an expected relative precision of 0.14 ppm. The second experiment proposed at J-PARC [75] will have a precision of about 0.45 ppm. Both experiments also intend to use the same data to search for the muon EDM with a precision of about 1×10^{-21} ecm [75, 189].

The possible experiment at PSI would provide an independent measurement of the muon $g-2$ with a different experimental technique and systematic uncertainties, as well as providing insight into uncharted terrain by improving on the sensitivity to a muon EDM.

Both measurements observe the spin precession $\vec{\omega}$ of a muon in a storage ring with an electric field $\vec{E}$ and magnetic field $\vec{B}$ given by

$$\vec{\omega} = \frac{q}{m}\left[a\vec{B} - \left(a + \frac{1}{1-\gamma^2}\right)\frac{\vec{\beta}\times\vec{E}}{c}\right] + \frac{q}{m}\frac{\eta}{2}\left(\vec{\beta}\times\vec{B} + \frac{\vec{E}}{c}\right). \tag{2.8}$$

Certain choices of the muon momentum and the combination of electric and magnetic fields permit measurements with strongly reduced systematic effects.

The muEDM collaboration at PSI proposes a search for the muon EDM with a sensitivity of about 6×10^{-23} ecm for a year of data taking using muons with a momentum of $|\vec{p}| = 125\,\mathrm{MeV}/c$, $|\vec{\beta}| = |\vec{v}|/c = 0.77$, and an average polarisation of better than $P = 93\%$ from the μE1 beam line at PSI with a particle flux of up to 2×10^8 μ^+/s. The concept is based on the frozen-spin technique [190, 191] combined with a spiral injection into a magnetic field of $B = 3\,\mathrm{T}$, similar as in the J-PARC $(g-2)$/muEDM experiment [75, 192]. A sketch of the experiment is shown in Figure 19.

The search profits from the large electric field in the rest frame of the muon $|E^*| = |\gamma c\vec{\beta}\times\vec{B}| = 1.1\,\mathrm{GV/m}$. A radial electrode system provides an electric field $\vec{E}_\mathrm{f}$ perpendicular to the motion of the muon and the magnetic field $\vec{B}$, hence $\vec{\beta}\cdot\vec{B} = \vec{\beta}\cdot\vec{E}_\mathrm{f} = 0$, and $\vec{B}\cdot\vec{E}_\mathrm{f} = 0$. By adjusting the strength of the electric field $\vec{E}_\mathrm{f}$ such that

$$a\vec{B} = \left(a - \frac{1}{\gamma^2-1}\right)\frac{\vec{\beta}\times\vec{E}_\mathrm{f}}{c}, \tag{2.9}$$

it is possible to cancel the anomalous precession term in (2.8), which simplifies the spin precession to

$$\vec{\omega} = \frac{q}{m}\frac{\eta}{2}\left(\vec{\beta}\times\vec{B} + \frac{\vec{E}_\mathrm{f}}{c}\right), \tag{2.10}$$

known as the frozen-spin technique.

The statistical sensitivity of this proposal is limited by the maximum muon momentum and the large lateral phase at μE1. As we outline in the following, by using a dedicated beam line with sub millirad divergence and a momentum of $P = 210\,\mathrm{MeV}/c$, this concept has the potential to improve the sensitivity of the muEDM search to better than 1×10^{-23} ecm. Without the electric field, i.e., with both electrodes grounded, this same setup measures the anomalous magnetic moment and could reach a relative statistical precision of the muon $g-2$ of about 0.1 ppm.

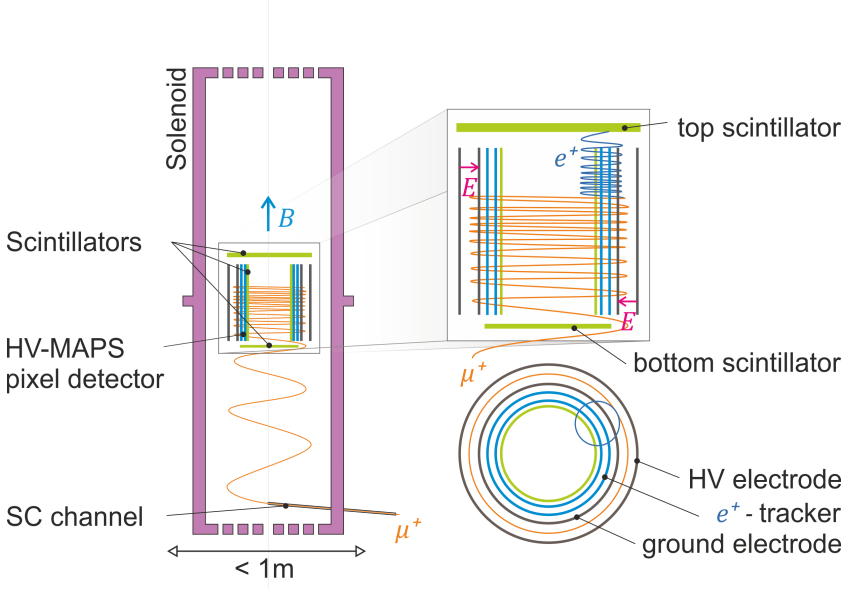

Figure 19: Sketch of the helix muEDM instrument, not to scale.

2.4.3 Prospects for a search of the muon electric dipole moment

The sensitivity for a muon EDM experiment deploying the frozen-spin technique [190] with $E \approx aBc\beta\gamma^2$ is given by

$$\sigma(d_\mu) = \frac{\hbar}{2\beta cP\gamma B\sqrt{N}\alpha\tau}. \tag{2.11}$$

Figure 20 illustrates expected sensitivities to a muon EDM in the case that a new dedicated beam could deliver muons with a phase space optimally adapted for injection. We assume an overall positron detection efficiency of 70%. As a benchmark case we consider the solenoid based layout described in the letter of intent [193] with a muon orbit of $r = 0.14\,\mathrm{m}$. Note that the sensitivity at $B = 3\,\mathrm{T}$, the nominal field value for the experiment proposed for the μE1 beamline, will be improved by a factor two if the next muon can be injected on request, whenever the previous positron decay was confirmed or a time-out of five times the laboratory lifetime is reached. In this single-muon-at-a-time scenario it is possible to improve the sensitivity to about $1 \times 10^{-23}\,\mathrm{ecm}$. Figure 20b shows that with a mean muon multiplicity above three, i.e. in average three muons are injected at a time, and a magnetic field above $B = 5\,\mathrm{T}$ a sensitivity of better than $8 \times 10^{-24}\,\mathrm{ecm}$, c.f. current limit $d_\mu < 1.5 \times 10^{-19}\,\mathrm{ecm}$ [160], in a year of measurement can be reached. This could be accomplished with a muon rate from muCool of $5 \times 10^5/\mathrm{s}$ and a repetition rate of 100 kHz (see Table 3 for a comparison of potential sensitivities).

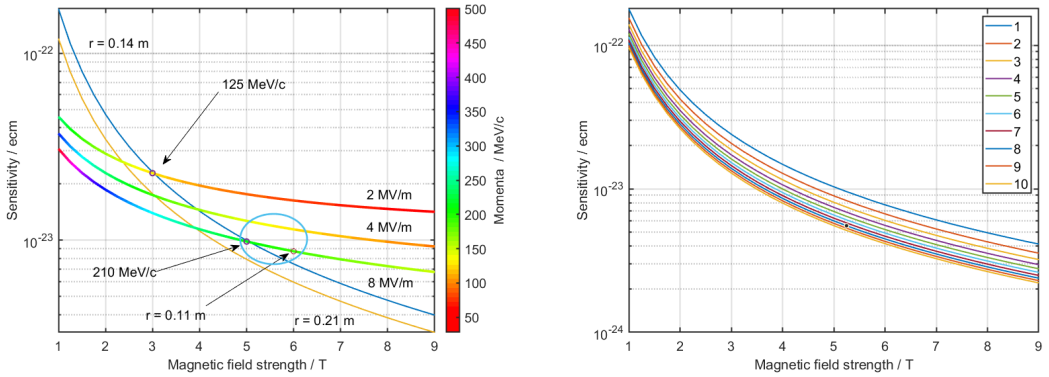

Figure 20: Sensitivity landscape for muon EDM searches. (a) Single muon-on-demand: Sensitivity increases with magnetic field strength keeping the radius constant. Electric fields above 8 MV/m are very difficult to obtain for large electrodes with extremely thin material thickness (positron transmission). The region within the circle indicates the possible parameter space for a future muEDM search using re-accelerated muons from muCool. (b) Increase in sensitivity with multiplicity of muons per injection for the case $r = 0.14$ m, as function of the magnetic field.

Table 3: Comparison of two future scenarios on a re-accelerated high-brightness muon beam with the concept proposed for μE1. A measurement with a sensitivity better than 1×10^{-23} ecm can only be realised with a larger magnetic field and higher momentum, which in turn also requires a higher electric field. Note that injection of more than one muon per measurement also requires a longer time-out, which partially compensates for the increase in injected muons.

	μE1	HIMB muCool	
	125 MeV/c	125 MeV/c	210 MeV/c
E-Field (MV/m)	2	2	8
B-Field (T)	3	3	5
radius (m)	0.14	0.14	0.14
e^+/year (1 muon)	7.3×10^{11}	4×10^{12}	3×10^{12}
Sensitivity/ year (1 muon) (1×10^{-23} ecm)	6	2.3	1
Sensitivity/ year (3 muons) (1×10^{-23} ecm)	-	1.9	0.8

2.4.4 Prospects for a high-precision measurement of the muon $g-2$

The HIMB in combination with a muon cooling stage and a re-acceleration beamline means that the same experimental setup, without the electric field applied, can be used to make a dedicated measurement of the magnetic moment of the muon. In this AMM measurement in the muEDM setup (AMMiED) no electric field will be applied and (2.8) will reduce to

$$\vec{\omega} = \frac{q}{m}\left(a\vec{B}\right) \tag{2.12}$$

in the absence of an EDM. In the case of using the same apparatus as for the search for an EDM the central electrode should be removed, to reduce multiple scattering, while the outer electrode is simply grounded.

The relative sensitivity of the anomalous frequency measurement is given by

$$\sigma(a_\mu)_{\mathrm{rel}} = \frac{\sqrt{2}\quad m_\mu}{P\sqrt{N}\gamma\tau\alpha\ ea_\mu B}. \tag{2.13}$$

Measurement of $g-2$ in muEDM setup

For the sensitivity calculation, shown in Figure 21, we assume the same values for P and α as in the muEDM scenario and a muon on request operation scheme with an integral positron detection efficiency of 70%. It can be seen that for a field strength of $B = 6\,\mathrm{T}$ a statistical sensitivity of 0.1 ppm can be reached, matching the expected final precision of the experiment at Fermilab. An improvement can be seen when the muon multiplicity is increased with the potential to achieve about 0.06 ppm, or to match the Fermilab sensitivity with a lower field strength of $B = 4\,\mathrm{T}$.

In terms of the systematic uncertainties, the experimental design benefits from the more compact magnet and hence a high field homogeneity is expected, as demonstrated in magnetic resonance imaging technologies. Further investigations need to be undertaken in order to fully understand the exact levels of these uncertainties.

Both previously discussed scenarios for a muon EDM and AMM measurement are based on the assumption of a highly efficient re-acceleration of muons to at least $125\,\mathrm{MeV}/c$ from the future low-energy, high-brightness source muCool. The caveat of such a scenario is the difficulty of a low loss extraction of muons from the high magnetic field region in muCool to the first acceleration stage and subsequent further acceleration. Although the initial phase space density and lateral extension within the muCool source are excellent, significant losses will appear due to muon decay and a mismatch of final beam and the experimental acceptance phase space, resulting in the likely situation of one single-muon-on-request-scenario.

Tiny all magnetic $g-2$ storage ring

An alternative concept, similar to first ideas presented during the PSI workshop 2010 by D. Taqqu, is to use non-relativistic muons, with an energy of $1\,\mathrm{MeV}/c$, in a tiny storage ring as depicted in Figure 22. This scenario circumvents the challenges of a long re-acceleration beam line by proposing to use only one radio frequency quadrupole (RFQ)

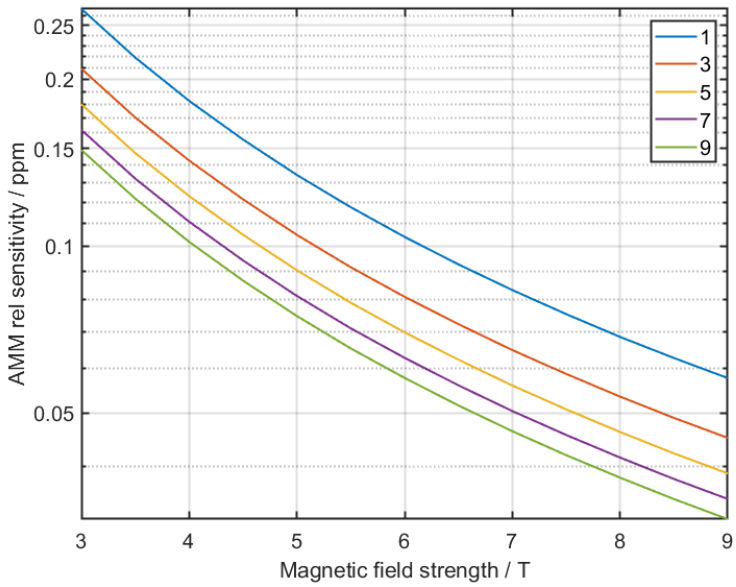

Figure 21: Statistical sensitivity in ppb for a measurement of the muon $g-2$. For this calculation the radius was fixed to $r = 0.14\,\mathrm{m}$ and $P = qBr$.

acceleration stage within the same high magnetic field of muCool and transporting the muons into a high magnetic solenoid field of 17 T. The muons longitudinal motion along the field lines is stopped by a short quadrupolar pulse similar as in the PSI muEDM concept. The muon is then confined to an orbit of about 6 mm diameter by using a weakly focusing magnetic field configuration. A combination of scintillating fibres and a segmented calorimeter detects the decay positron. Although, sub nanosecond timing resolution for scintillating fibres has been reported, a direct measurement of the muon spin precession frequency to extract g and not $g-2$ seems still too ambitious as it would require a resolution of better than 40 ps. Instead we propose to use a central scintillating fibre bundle within the tiny storage orbit to distinguish between in and outwards going positrons for a measurement of the anomalous precession frequency.

2.4.5 Conclusion

There is potential to investigate the tantalising hints of new physics by measuring the magnetic dipole moment of the muon using a different method and to reach four orders of magnitude below the current muon EDM limit using a novel low-energy, high-brightness muon source coupled to the proposed HIMB. In this section we discussed possible prospects for a muon EDM measurement, which will ideally require a highly efficient re-acceleration to muon momenta of about 210 MeV/c. For a measurement scheme based on a single-muon-on-request we show that a sensitivity of $\sigma(d_\mu) = 1 \times 10^{-23}$ ecm may be expected within one year of data taking, with a potential improvement if multiple muons are stored at the same time. Similarly, we presented two possible scenarios for a high-

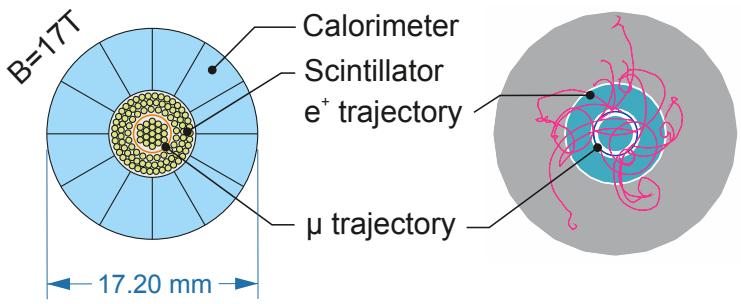

Figure 22: Sketch of a hyper compact $g-2$ storage ring experiment, TiAMMo, using muons with $E = 1\,\mathrm{MeV}$ from a moderately re-accelerated low-energy, high-brightness muon source in a $17\,\mathrm{T}$ magnetic field.

Table 4: Comparison of principle parameters of Fermilab E989 [74], J-PARC [75] and our proposals (AMMiED and TiAMMo).

	Fermilab E989	J-PARC	AMMiED	TiAMMo
Muon momentum	$30.9\,\mathrm{GeV}/c$	$300\,\mathrm{MeV}/c$	$125\,\mathrm{MeV}/c$	$14.6\,\mathrm{MeV}/c$
Lorentz γ	29.3	3	1.56	1
Polarisation	100%	50%	95%	95%
Magnetic field B	$1.45\,\mathrm{T}$	$3\,\mathrm{T}$	$6\,\mathrm{T}$	$17\,\mathrm{T}$
Focusing field	E-quadrupoles	weakly focusing (wf)	wf	wf
Cyclotron period	$149\,\mathrm{ns}$	$7.4\,\mathrm{ns}$	$3.8\,\mathrm{ns}$	$0.4\,\mathrm{ns}$
AMM precession period	$4.37\,\mu\mathrm{s}$	$2.11\,\mu\mathrm{s}$	$1.05\,\mu\mathrm{s}$	$0.37\,\mu\mathrm{s}$
Number of detected e^+	1.6×10^{11}	5.7×10^{11}	7×10^{12}	1.7×10^{12}
AMM precision (stat.)	$0.1\,\mathrm{ppm}$	$0.45\,\mathrm{ppm}$	$0.1\,\mathrm{ppm}$	$0.08\,\mathrm{ppm}$
AMM precision (sys.)	$0.1\,\mathrm{ppm}$	$0.07\,\mathrm{ppm}$	–	–

precision measurement of the muon $g-2$ with a statistical sensitivity better than 0.1 ppm in one year of data taking, matching or even surpassing the prospected sensitivity of the currently ongoing effort at Fermilab (see Table 4). Again higher sensitivity could be achieved if the source provided sufficient muons to permit a storage of more than one muon at a time within the storage ring. The tiny non-relativistic storage ring proposal has the advantage to avoid a long re-acceleration beam line. The price for this is a re-acceleration scheme within a solenoid guiding field and a high magnetic field for storage of $B = 17\,\mathrm{T}$ resulting in an orbit of less than 6 mm diameter.

2.5 Muonium

2.5.1 Development of novel muonium sources at PSI

A high-intensity, low-emittance atomic muonium $M = (\mu^+ e^-)$ beam is being developed at PSI, which would enable improving the precision of M spectroscopy measurements, and may allow a direct observation of the M gravitational interaction.

Improvements in measuring the 1S-2S transition frequency using state-of-the art laser spectroscopy techniques is strongly motivated by recent experiments measuring the muon AMM [12], and other searches for BSM physics. Measurement of the free fall of M atoms would be the first test of the weak equivalence principle using elementary antimatter (μ^+) and a purely leptonic system.

Both experiments rely on the high-intensity, continuous muon beams at PSI with significant benefits expected from the proposed HIMB upgrade. The especially challenging gravity experiment additionally relies on a proposed novel atomic M source, with cold atoms converted in the surface of superfluid helium (SFHe).

Present state-of-the-art vacuum muonium sources are room temperature, porous materials that allow combination of the muon with an electron from the bulk, and a following quick diffusion inside the nanoscopic pores, with laser ablated silica aerogel being one of the best room temperature converters. Such sources provide $\sim 3\%$ muon-to-vacuum M conversion using surface μ^+ beams of 28 MeV/c momentum [194].

Mesoporous materials have been shown to convert μ^+ to vacuum M with efficiencies of 40% (20%) at room temperature (down to 100 K) when using highly moderated, keV energy muons from the Low Energy Muons (LEM) beamline at PSI [195, 196]; this has an intensity four orders-of-magnitude lower than a surface muon beam. Future developments of moderated low-energy muons (the muCool experiment described in Section 4.2) may reach one to two orders of magnitude higher rates. However, such converters produce a M beam with broad (thermal) energy and angular ($\sim \cos\theta$) distributions. Improving the source quality by cooling these samples results in lower emission rates, with no observable emission below ~ 50 K due to the decreased diffusion constant, and to the sticking of M to the pore walls that occurs unavoidably with any conventional M converter [195, 197].

A newly proposed experiment at PSI plans to tackle the above difficulties by using SFHe as a vacuum M converter, due to its inert nature that rejects impurities from its bulk even at the lowest temperatures [198–200]. Based on the calculated and measured

chemical potentials of hydrogen isotopes in SFHe [201, 202], M atoms are expected to have a high chemical potential in the liquid compared to the thermal energies, implying that they would be ejected from the SFHe surface with a well defined longitudinal velocity of $v_M \sim 6300\,\mathrm{m/s}$ only broadened by the thermal spread which is expected to fall below the Landau velocity ($v_t \approx 50\,\mathrm{m/s}$).

Assuming high muon-to-vacuum-muonium conversion rates on the order of 10-20% in SFHe, the present πE5 beamline at PSI could provide a flux of $1 - 5 \times 10^5$ M/s from the cold atomic beam, while the HIMB beamline could offer up to an order of magnitude higher rates.

2.5.2 Spectroscopy

Pure leptonic systems, such as positronium and muonium are free of finite-size effects and therefore are ideal systems to test bound state QED [203]. They are essential to extract fundamental constants such as the muon mass and magnetic moment. Those systems can also be used to search for new physics, including dark-sector particles and new muonic forces [204], as well as testing Lorentz/CPT symmetries [205] or measure the effect of gravity on antimatter via the gravitational redshift [206].

Past M spectroscopy experiments were conducted between $1980 - 2000$ at TRIUMF, RAL and LAMPF (see [207] for a recent review). As a result of the difficulty in obtaining a high flux of μ^+ and the necessity to slow down the muons so that M into vacuum can be formed efficiently, all those experiments were essentially limited by statistics, or statistics-related systematic effects [207]. With its intense μ^+ beam, PSI harbours tremendous opportunities for improving M spectroscopy experiments. Higher statistics makes it possible to implement experimental techniques that are systematically more robust. In this respect the LEM beamline at PSI [208] plays a crucial role as recently demonstrated by the Mu-MASS collaboration [209] which improved the determination of the M Lamb shift (LS) by one order of magnitude [210].

A recent review of the ongoing measurements of the 1S-2S transition and the LS of muonium in the context of the Mu-MASS experiment at PSI is given in [211]. A description of the progress of the Muonium Spectroscopy Experiment Using Microwave (MuSEUM) that is ongoing at J-PARC aiming to improve the muonium hyperfine splitting (HFS) can be found in [212]. Here we point out the impact that HIMB would have on muonium spectroscopy. HIMB would increase by orders of magnitude the available statistics of these experiments. This will also allow for accurate studies of the systematic effects and for the implementation of new measurement schemes, such as the employment of an enhancement cavity with a larger laser beam to reduce AC-stark shift in the 1S-2S measurement or the use of separated oscillatory fields spectroscopy to measure Lamb shift, fine structure and HFS.

HIMB would allow to push the experimental projected accuracy of the ongoing Mu-MASS and MUSEUM experiment by an order of magnitude, below 1 kHz for the 1S-2S transition and to the few Hz level for the HFS. Assuming the theoretical accuracy could also be improved to match the experimental one, combining those measurement will result in a very stringent test of bound state QED [213]. It will also allow to improve

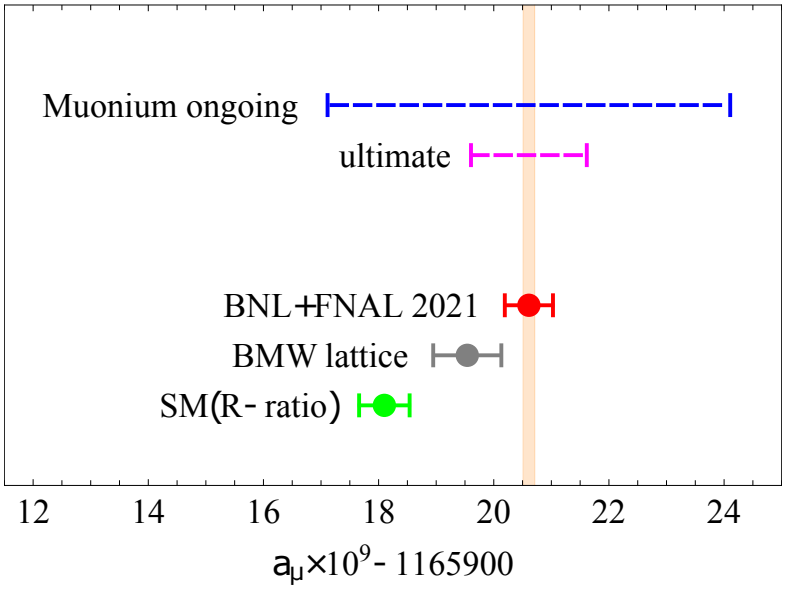

Figure 23: Muon AMM determined from the combined measurements at BNL and FNAL (red) [12], SM calculations with leading-order HVP evaluated from $e^+e^- \to$ hadrons data (green) [14] or using a recent lattice QCD result (gray) [97]. Also shown are the projected sensitivities in muonium (dashed) with the currently planned spectroscopy improvements (blue) and its ultimate improvement which could be reached at HIMB (magenta), centred around the current experimental average. The orange band shows the four-fold improved FNAL standard deviation expected in the near future. Adapted from [214].

the determination of fundamental constants such as the muon mass, the muon magnetic dipole moment, and a determination of the Rydberg constant independent of finite size effects as well as the determination of the fine structure constant at a level comparable with the current best determinations [69, 70] .

Moreover, as pointed out recently [214], M spectroscopy at this level of precision would provide an independent determination of the muon AMM with an uncertainty at the level of the current tension. This is illustrated in Figure 23.

M spectroscopy offers also the possibility to search for new light bosons coupled to electrons and muons [204]. This is very interesting since those could provide an explanation in terms of new physics of the muon AMM. In this case, a dark force between the electron and the antimuon could be mediated for example by a new scalar or a new

vector gauge boson giving rise to Yukawa-like attractive potentials [215]

$$V_{ss}(\vec{r}) = -g_e^s g_\mu^s \frac{e^{-m_s r}}{4\pi r} \tag{2.14}$$

$$\begin{aligned} V_{vv}(\vec{r}) = &-g_e^v g_\mu^v \frac{e^{m_v r}}{4\pi r} \\ &+\frac{g_e^v g_\mu^v}{4}\Bigg(\vec{\sigma}_e \cdot \vec{\sigma}_\mu \Big(\frac{1}{r^3} + \frac{m_v}{r^2} + \frac{m_v^2}{r} - \frac{8\pi}{3}\delta(\vec{r})\Big) \\ &\quad - (\vec{\sigma}_e \cdot \hat{r})(\vec{\sigma}_\mu \cdot \hat{r})\Big(\frac{3}{r^3} + \frac{3m_v}{r^2} + \frac{m_v^2}{r}\Big)\Bigg) \frac{e^{-m_v r}}{4\pi m_e m_\mu} \end{aligned} \tag{2.15}$$

where V_{ss} and V_{vv} are for scalar and vector potentials, respectively, m_s is the scalar boson mass, m_v is the vector boson mass, and $g_e^{s,v}, g_\mu^{s,v}$ are the coupling strengths to electrons and antimuons. The effect of such new forces on the measured transitions can be estimated by applying first order perturbation theory.

In Figure 24, we present the current and projected sensitivity with HIMB of muonium spectroscopy to new physics. The constraints on g_e^s, g_μ^s as a function of the scalar/vector mass, which are nearly identical in the mass range considered here, are compared to the region favoured by the $g-2$ muon anomaly, considering the bounds from the electron gyromagnetic factor [64]. However, as pointed out in Section 2.4.1, the situation for the electron AMM should be clarified since the two latest determinations of the fine structure constant using atom interferometry differ from each other by $5\,\sigma$ [69, 70]. We do not present results from experiments at the intensity frontier since those typically depend on assumptions on the decay channels. An example is the recent results of the NA64 experiment placing stringent bounds on new bosons with the assumption that those would decay invisibly [216]. The combination of the Lamb shift and 1S−2S M measurements provides the most stringent laboratory constraint excluding that a new scalar/vector boson with a mass $< 10\,\mathrm{keV}$ could contribute to the muon $g-2$ anomaly.

Another interesting application is that M spectroscopy is sensitive to Lorentz and CPT violating effects. In the context of the Standard Model Extension (SME) this would improve the current limits [205]. Moreover, a test of the gravitational behaviour of second generation leptons via the gravitational redshift [206] will become possible.

The realisation of HIMB would thus greatly expand the physics reach of M spectroscopy.

2.5.3 Gravitational free fall experiment of muonium

The novel cold atomic beam under development would enable the measurement of the gravitational fall of M atoms by means of atom interferometry. However, such an experiment is inherently challenging due to the short lifetime or the muon ($\tau \approx 2.2\ \mu$s) which allows a mere $\Delta x = \frac{1}{2} g t^2 = 600$ pm gravitational fall in a time of $t = 5\tau$. Measuring small deflections like this needs a precise knowledge of the initial momentum of the atoms, and requires strict momentum selection. Two periodic gratings (G1 and G2)

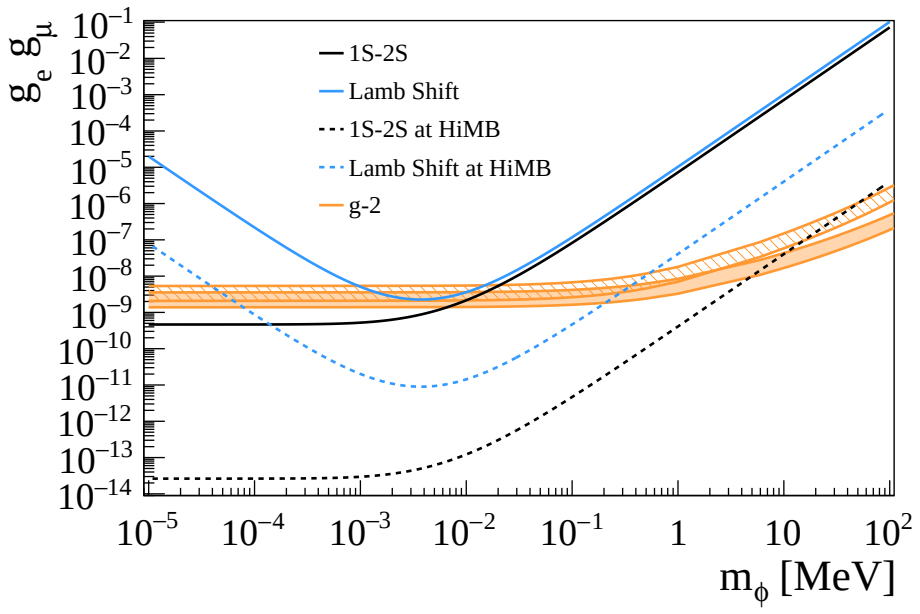

Figure 24: Constraints from M spectroscopy on g_e^s, g_μ^s as a function of the scalar/vector mass. The solid black line is the constraint from the M 1S$-$2S measurement [217] while the blue line is from the recent Lamb shift measurement at PSI [210]. The dashed lines are the projections of the uncertainty that would be enabled by HIMB. The orange band represents the region suggested by the $g-2$ muon anomaly considering the lower bound from the measurement of the electron gyromagnetic factor for the scalar case, while the hatched region is for the vector one.

with horizontal slits of pitch d and spaced by a distance L could be used to achieve this momentum selection as shown in Figure 25.

The classical and quantum regime of this device is characterised by the de Broglie wavelength of the atoms, $\lambda = h/p$, and grating pitch d in terms of the Talbot length, $L_T = d^2/\lambda$, which is approximately 18 microns for thermal M atoms with $\lambda_M \approx 0.56$ nm. Trajectory selection for both classical and quantum regimes of this device by G1 and G2 will result in an intensity pattern with the same periodicity d at a distance L after G2. Gravitational acceleration and deflection of the atoms causes a phase shift $\delta\phi$ of this pattern in the vertical direction as $\delta\phi = 2\pi g T^2/d$, where $T = L/v_M$ is the M time of flight between each pair of gratings.

Direct observation of this sub-micron pattern and sub-nanometer shifts needed for measuring M gravity would be extremely hard. It is possible however to carry out an indirect measurement using a third grating (G3) of the same pitch d, placed at distance L from G2. By counting the total rate of M atoms transmitted through G3 as a function of the G3 vertical position Δx the phase shift can be measured.

The contrast of the intensity pattern C is defined by the ratio of the amplitude and the average yield $C = A/A_0$ as shown in Figure 25. This contrast strongly depends on

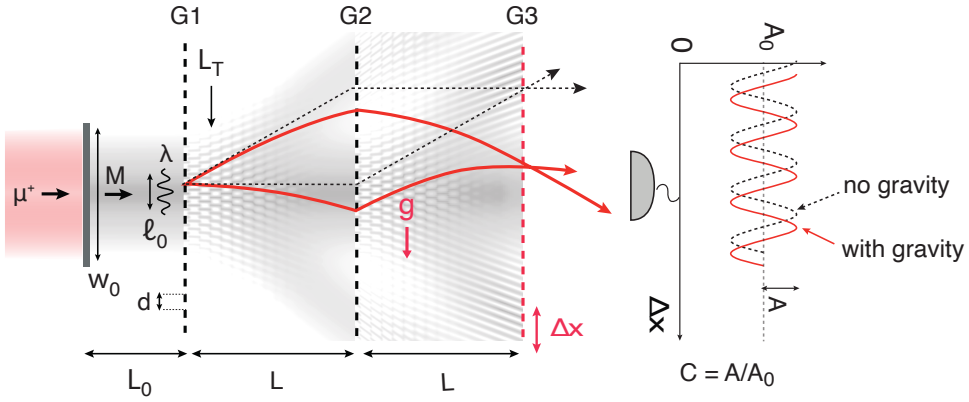

Figure 25: A three-grating interferometer used to measure the gravitational interaction of M atoms. The quantum diffraction pattern caused by the gratings G1 and G2 with a fully coherent beam is given in grey. Classical trajectories (red and dashed lines) are shown to illustrate the effect of gravity on the measured interference pattern appearing at G3. The vertical shift of the interference pattern caused by the gravitational acceleration g is detected by measuring the transmitted M rate while scanning G3 in vertical direction. See details in text.

the transverse coherence length of the beam, ℓ_0, that determines how many slits of G1 are illuminated with a coherent wavefront. This coherence length in relation to the beam width w_0 and the interferometer parameters (the grating periodicity d and distances L) together with the de Broglie wavelength (λ) of the atoms is sufficient to estimate the interferometer performance in the first approximation. In analogy to statistical optics (Van Cittert-Zernike theorem [218]), we can relate the transverse coherence length of the M beam to the transverse momentum distribution of the atoms as $\ell_0 = \frac{1}{2}\frac{\lambda}{\alpha} \approx 16$ nm, where α is the angular spread of the cold M source.

The sensitivity in measuring the gravitational acceleration g is given by [219]

$$\Delta g = \frac{1}{2\pi T^2}\frac{d}{C\sqrt{N}}\,, \tag{2.16}$$

where N is the number of M atoms transmitted through G3 and measured by the detector given by

$$N = N_0\,\varepsilon_0\,e^{-(t_0+2T)/\tau}\,(T_G)^3\,\varepsilon_{\rm det}\,, \tag{2.17}$$

with N_0 being the number of M atoms produced at the M source, and ε_0 the M transport efficiency from the source to G1. The M decay is accounted for by the third term $e^{-(t_0+2T)/\tau}$, where t_0 is the time of flight from the source to G1. The number of detected M atoms is further reduced by the M detection efficiency $\varepsilon_{\rm det}$, and by the limited transmission T_G of a single grating. The short lifetime of the muon necessitates a gain in sensitivity by using a small grating pitch d. Maximal sensitivity, as a tradeoff between phase shift $\delta\phi$ and statistics N, is obtained for $T \approx 6-8$ μs corresponding to an interferometer length of 40-50 mm.

A calculation of the interferometer parameters to extract the contrast C, uses an approximation of the M source with a Gaussian Schell-model beam [220], and adapted mutual intensity functions that are widely used to describe the propagation of partially coherent light [218]. Using realistic parameters on the initial beam size and quality expected from the superfluid source above, the fringe contrast of $C \approx 0.3$ at the exact position of G3 can be achieved, with a few μm high-contrast region along the beam axis. Such a measurement thus requires precise G3 positioning with μm-accuracy in the beam axis, and below-nm-accuracy in the vertical direction.

From (2.16) we see that determining the sign of g (more precisely to reach $\Delta g/g = 1$) in about one day, requires the detection of 3.2 M/s, assuming a contrast $C = 0.3$. Following (2.17), and taking pessimistic estimates from Monte-Carlo simulations and initial detector and grating studies studies by using $T_G = 0.3$, $\varepsilon_0 = 0.75$ and $\varepsilon_{\rm det} = 0.3$, at the source we need $N_0 \approx 1.4 \times 10^4$ M/s. As a comparison the πE5 beam line at PSI can presently deliver 3.6×10^6 μ^+/s at a momentum of 10 MeV/c within a transverse area of about 400 mm^2. At this muon momentum we may expect a muon-to-vacuum-M conversion efficiency of about 0.1-0.3 in the best case, when fast diffusion of the atoms can be assumed. This will result in M rates of up to $\sim 1.1 \times 10^6$ M/s. These high rates may allow a further collimation of the M beam to a 5×1 mm area, which would put less strain on grating production and alignment and would cut the number of useful M atoms conservatively by a factor 5 mm^2/400 mm^2 = 0.013. Using these parameters where there is room for contingency, we expect to produce the necessary rate of $\sim 5 \times 10^4$ M/s in an small area of $\sim 5 \times 1$ mm^2, and reach the goal sensitivity of $\Delta g = \frac{9.8\ \mathrm{m/s^2}}{\sqrt{\#\ \mathrm{days}}}$ with present μ^+ sources. An increase by two orders of magnitude in μ^+ rates expected by the proposed HIMB project at PSI will allow shorter measurement times and further improvements on the sensitivity to g.

2.6 Further particle-physics applications

2.6.1 Muon decays

LFV muon decays $\mu \to eee$ and $\mu \to e\gamma$ are flagship cases for HIMB. In this subsection we consider other SM and BSM muon decay processes that allow to further scrutinise the operator causing the decay of the muon, but also allows for a more general approach to look for low-mass BSM particles coupling e.g. to electrons or neutrinos. As we will describe there, has been a lot of activity in the past decades to use muons as a more general laboratory for BSM physics. Many of the results described here can in principle be improved upon with an increased rate provided by HIMB.

The Michel decay of muons $\mu^+ \to e^+(\nu_e \bar{\nu}_\mu)$ played an important role in many aspects of particle physics. Its description through the Fermi theory with a $V-A$ four-fermion interaction was an early application of effective theories and the determination of the Fermi constant via the muon lifetime [221] is a crucial ingredient for electroweak precision tests.

A more general analysis of muon decays is typically done allowing for right-handed neutrinos, but neglecting their mass [222, 223]. If no information on the positron po-

larisation is available, the energy spectrum of the decay positron can be expressed in terms of four decay parameters [224], usually denoted by ρ, δ, η and $P_\mu\,\xi$, with P_μ the polarisation of the muon. The presence of BSM physics results in deviations of these parameters from their SM value. Earlier searches for right-handed currents [225] have been generalised [226] and lead to stringent constraints on ρ, δ, η and ξ.

The most recent and most precise measurements of the muon decay parameters ρ, δ, and $\mathcal{P}_\mu\xi$ were obtained by the TWIST experiments stopping a highly polarised beam in a silver target located inside a 2 T solenoid and surrounded by tracking and timing detectors [227, 228]. These measurements were not statistically limited, but relied on a precise control of all relevant systematic effects. In that sense, such measurements will not profit from the increase in muon rates offered by HIMB. This is especially true when measuring $\mathcal{P}_\mu\xi$ where a very precise knowledge of the muon beam polarisation is paramount and which is almost impossible to achieve at a high-acceptance beamline such as HIMB. However, the measurements of ρ and δ could profit from a beam such as HIMB-muCool (see Section 4.2), which would allow to stop the beam in an extremely thin target thus greatly reducing systematic uncertainties related to the passage of the Michel positron through the target and would allow a very compact detector arrangement potentially reducing the systematic uncertainties related to detector response and calibrations.

Interpreting the muon decay parameters in terms of Wilson coefficients of a general EFT containing SM particles and some number of sterile neutrinos provides a framework to combine muon decay constraints with more general BSM explorations. Contrary to [222, 223] this requires to allow for non-negligible sterile neutrino masses, as e.g. in [229–231]. In addition to the Michel decay, also the RMD $\mu \to e(\nu\bar{\nu})\gamma$ and the rare muon decay $\mu \to e(\nu\bar{\nu})(ee)$ can be used. The additional visible final-state particles can help to analyse potential effects in more detail. On the other hand it has to be kept in mind that the low energy scale of the process severely limits the scale of BSM physics that can be tested.

While the rate of the RMD and rare decay with HIMB is no issue at all, analysing these processes would require to collect a certain amount of data disregarding the kinematic cuts used in cLFV searches. For the rare decay in connection with Mu3e this is probably more realistic than for the RMD in connection with a MEG-like experiment.

Regarding more general searches for low-mass BSM, in recent years theorists have actively explored new physics prospects below $\sim$ GeV [232], and various experiments have found hints for new particles below the muon mass. For instance, there are neutrino experiments which individually find evidence for an additional massive neutrino, and as a possible explanation for the ^{8}Be anomaly in nuclear decays [233] a 17 MeV boson has been suggested. The fact that a 17 MeV boson coupled to electrons is difficult to confirm or rule out motivates the search for deviations in SM muon decays.

There are also numerous theoretically well motivated scenarios with nearly massless axion-like particles (ALPs). They appear as Goldstone bosons and possibly have even LFV couplings. This can lead to muon decays where there are BSM particles among the invisibles [232, 234, 235]. Searches for the two-body decay $\mu \to eX$ with X an ALP were carried out at TRIUMF [225, 236]. For sufficiently large m_X such a process would lead

to a bump in the positron energy spectrum. For nearly massless X the endpoint of the spectrum is modified and a careful comparison to the SM prediction is required. In this context there is also the possibility to use a forward detector to increase the sensitivity, since the SM background is strongly suppressed in the forward direction [237–239]. The sensitivity of $\mu A \to eA$ experiments to emission of an ALP is explored in [240]. Several decades ago Cristal Box looked for $\mu \to eX\gamma$ [241] and $\mu \to e\gamma\gamma$ [242]. Regarding the latter, the two photons could arise from an ALP decay $X \to \gamma\gamma$ or a contact interaction (of dimension 8). More recently, MEG has looked for $\mu \to eX \to e\gamma\gamma$ [243] and improved the limits for the branching ratio $X \to \gamma\gamma$ in the range $m_X = 20 - 45\,\text{MeV}$.

Another prominent example of a BSM particle that can be looked for in muon decays is a dark photon. For Mu3e there are first studies [35] for dark photon and LFV two-body decays. While they can be carried out in phase I of Mu3e, a dedicated experimental search with HIMB would improve the sensitivity.

Astrophysics can constrain particles with masses $\lesssim$ few MeV that are feebly coupled to the first generation, and energy frontier experiments exclude new particles with large couplings — but for new particles coupled to the first and/or second generation, there remains an allowed triangle [232], beyond astrophysics, the energy frontier and current intensity frontier bounds, which precision μ decays could explore.

An X boson coupled to neutrinos could alleviate [244] the current H_0 tension [245, 246] in cosmology, and be produced via $\mu \to e\nu\bar{\nu}X$. Some current experimental constraints on this scenario have been discussed [247], but the theoretical study [248] suggests that meson decays could be more sensitive to such an X than $\mu \to e\nu\bar{\nu}X$, because X emission removes the chiral suppression of the meson decays.

To summarise, there are many low-mass BSM physics scenarios that can affect muon decay processes. A general EFT extension as well as a collection of simplified low-mass BSM models are being implemented for muon decay processes in the framework McMule [249]. Together with the precise prediction of SM muon decays this gives a theoretical basis for a detailed investigation of the potential impact of future measurements with HIMB.

2.6.2 Muonium - antimuonium oscillations

Bruno Pontocorvo predicted there might be $M\overline{M}$ oscillations [250], in analogy to $K^0\bar{K}^0$ mixing, even before M was discovered [251]. In the past, $M\overline{M}$ oscillations were searched for in Ar gas [252], at TRIUMF [253, 254], with foils at LAMPF [255] and also with SiO_2 powder targets at LAMPF [256–258], and most recently with the same approach at PSI [259, 260]. The current best upper limit for the probability of spontaneous muonium to antimuonium oscillation is $P_{M\overline{M}} < 8.3 \times 10^{-11}$ (90% CL) and was obtained with the MACS apparatus at PSI.

Muonium has a lifetime of $2.2\,\mu$s and decays into a fast positron (e^+_μ) from the muon decay and a slow electron (e^-_A) from the bound electron. The decay of an antimuonium is signalled by a final state with the opposite electrical charges, *i.e.*, a fast electron (e^-_μ) and a slow positron (e^+_A).

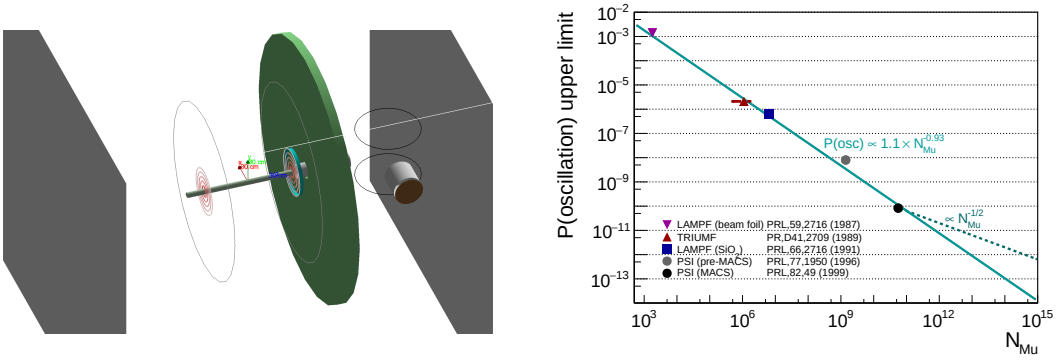

Figure 26: (left) Straw-man GEANT4 setup emulating the MACS apparatus. The μ^+ beam enters from the left and hits a target (hidden in the beam pipe) inside the 5-layer tracker. (right) Development of the upper limit of the $M\overline{M}$ oscillation probability vs. the number of produced $N_M (= N_{\mathrm{Mu}})$ in the acceptance of the experiments. The results are taken verbatim from the publications and consist of upper limits at 90%CL and 95%CL (no re-scaling has been performed as the difference is not visible on this plot). The lines are to guide the eye.

To study the different beam setups in more detail, a straw-man GEANT4 [261] simulation setup emulating the MACS apparatus was developed as shown in Figure 26 (left). A target is embedded inside a five-layer tracker with total length of 1m. In a region extending over 2 cm along the μ^+ beam direction, an electric field of 1.5 kV/cm provides acceleration for e^+_{A}, and a solenoidal magnetic volume bends the accelerated e^+_{A} onto a sensitive volume. This simulation allows the modelling and estimation of (1) the decay characteristics of the M, (2) the acceptance (defined as the fraction of M decays inside the active detector volume), and (3) the detection efficiency as a function of the M kinetic energy (E_M^{kin}) and production divergence. For a real detector, a configuration allowing the simultaneous measurement of M and $\overline{M}$ (e.g. with the accelerating electric field perpendicular to the μ^+ direction) would be chosen.

In all setups, the simulated detector setup was kept constant. Therefore, the fraction of M decays inside the active volume (f_D) decreases strongly with increasing E_M^{kin}. Table 5 illustrates this behaviour.

To significantly improve on the current best upper limit $P_{M\overline{M}} < 8.3 \times 10^{-11}$ (90% CL) of [260], a minimum of $N_M^{\mathrm{decay}} = 10^{12}$ is required, cf. Figure 26 (right). This is reachable with aerogel targets with relatively short measurements, and may also be achieved with foils.

2.6.3 Atomic parity violation in muonic atoms

A muonic atom is formed when a negative muon comes to rest in a material and subsequently gets captured by a nearby atom. After this atomic capture, the muon quickly cascades down to the $1s$ atomic orbital, emitting Auger electrons and X-rays. Due to its relatively large mass, there is significant overlap between the muon wave function and

Table 5: Expected M decays per second (N_M^{decay}) in vacuo for different beam intensities N_{μ^+} and $\mu^+ \to M$ (in vacuo) conversion efficiencies η_M. The factor f_D specifies the fraction of M decaying inside the detector volume corresponding to the M kinetic energy E_M^{kin}.

Target	N_{μ^+} [s^{-1}]	η_M	E_M^{kin} [eV]	f_D	N_M^{decay} [s^{-1}]
HIMB-3/Al[(a)]	1.0×10^{10}	0.001	20000	0.07	7.0×10^5
HIMB-3/SiO_2[(b)]	1.0×10^{10}	0.028	0.026	1.00	2.8×10^8
HIMB-3/aerogel	1.0×10^{10}	0.015	0.026	1.00	1.5×10^8

[(a)]Assuming η_M as in [255] [(b)]Target not stable over time.

the atomic nucleus. This makes this system particularly attractive to study short range interactions between the muon and a nucleus/nucleon.

Muonic atoms are being used to determine absolute nuclear charge radii, most recently by the CREMA collaboration for low Z nuclei [262–264] and by the muX collaboration for high-Z radioactive elements [265].

Another compelling physics case for muonic X-rays is atomic parity violation (APV) which arises from the mixing of the opposite parity $2s_{1/2}$ and $2p_{1/2}$ atomic levels, resulting in an E1 admixture in the otherwise pure M1 $2s_{1/2} - 1s_{1/2}$ transition [266]. The most straightforward parity violation (PV) observable is the angular correlation between the $2s - 1s$ X-ray and the electron from the μ^- decay in orbit.

Observing the single photon $2s-1s$ transition is a challenge however. For Z$\backsimeq$30 nuclei, this transition has a BR of $\mathcal{O}(10^{-4})$. At lower Z two-photon and Auger transitions completely dominate the depopulation of the 2s level. A clean detection of this X-ray is hampered by a dominant background from Compton scattered $(n > 2)p - 1s$ X-rays. In addition, the SM amplitude of a PV observable is expected to be smaller than 10^{-3}. For boron (Z=5) or neon (Z=10) the PV $e^-\gamma$ correlation is expected to be at the 10^{-2} or 10^{-3} level, respectively. Additional challenges arise however due to the Auger depopulation of the $2s$ level, necessitating a low pressure gas target to avoid repopulating the electric orbitals [267]. Furthermore, the small energy difference between the $2s$ and $2p$ levels, responsible for the large APV, makes it hard to resolve the $2p-1s$ and $2s-1s$ transitions with traditional X-ray detectors.

The muX collaboration has been investigating the reach of a $2s - 1s$ APV experiment for Z$\backsimeq$30 nuclei. Deploying a high-purity germanium (HPGe) detector array at the πE1 beamline, the transition was observed in Kr and Zn for the first time [265]. Despite being the photon detector of choice for many applications in the 0.1 to 10 MeV energy range, HPGe detectors have long charge collection times and are susceptible to neutron damage, limiting the instantaneous and integrated rate, which in turns limits a muX-style APV experiment (Figure 27) to a sensitivity of $\mathcal{O}(10^{-3})$ on a PV observable such as the $e^-\gamma$ correlation.

To fully profit from the high μ^- rates at HIMB, or even from the current intensities

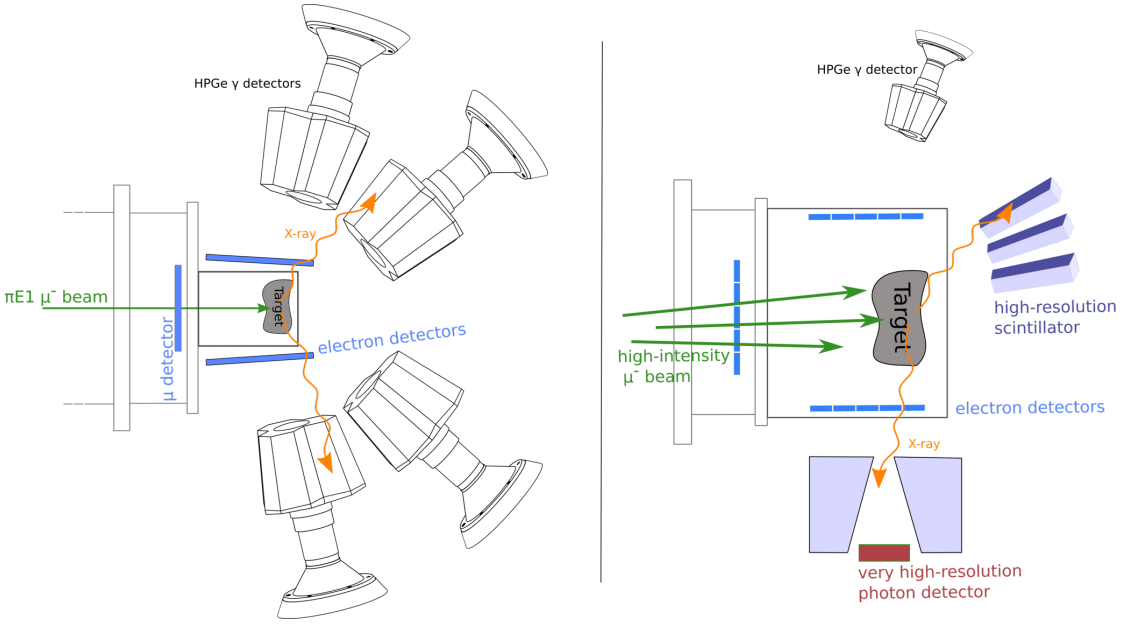

Figure 27: Left: Sketch of the muonic X-ray setup currently used at the πE1 beam area, with a thin muon counter, a small target surrounded by Michel electron detectors, and a HPGe detector array. Right: Accepting higher incoming muon rate requires the development of larger targets and/or a confining magnetic field, and the use of novel high-resolution photon detectors such as $LaBr_3$ detectors and microcalorimeters.

available at the πE5 beam area, alternative high-resolution photon detector technologies have to be considered. One promising technology are high-resolution inorganic scintillators such as doped $LaBr_3$ detectors, where resolutions of better than 2 % at 1 MeV are on the horizon. A rough estimate with 50 1×1 inch detectors placed 25 cm from a muon target shows that a statistical precision on the $e^-\gamma$ correlation of better than 10^{-3} is possible.

For Z$\backsimeq$30 nuclei this would mean an $\mathcal{O}(1)$ SM test. Searching for muon-specific dark forces, as suggested in [268], this level of sensitivity can be competitive when only taking the low-energy μ two-loop constraints from normal APV. Taking into account LHC bounds from non-resonant di-lepton data [269], the sensitivity of a muon APV experiment to Q_W needs to be similar as the ^{133}Cs APV measurement, which is at the 1% level. As a consequence, from this perspective only a measurement with low-Z nuclei is worth pursuing as the APV amplitude is experimentally accessible due to the near degeneracy of the $2s_{1/2}$ and $2p_{1/2}$ states. This energy split quickly increases with a Z^4 dependence, yielding APV amplitudes $< 10^{-3}$ for Z$\geq$30 nuclei. To realize such APV measurement with sufficient sensitivity, R&D efforts need to be put into novel detector technologies, as well as in efficient low-pressure gas-targets.

The HIMB μ^- intensities also open up the opportunity to apply ultra-high resolution γ detectors such as crystal spectrometers (see e.g. [270]) and state of the art cryogenic microcalorimeters (see e.g. [271, 272]) to muonic X-rays spectroscopy. A first possible

physics case are bound-state QED tests using exotic atoms as suggested in [273]. Such a measurement can probably be done with a fairly simple target station.

2.6.4 Muon conversion

Searches for the conversion of the muon into an electron in the field of the nucleus have been performed at PSI in the past and indeed the current best limit on this so far unobserved process is given by the SINDRUM II collaboration in [24]. Large efforts are currently being undertaken by the Mu2e and COMET collaborations [27, 28] to perform these measurements at Fermilab and J-PARC, respectively, aiming at improving the sensitivity of the SINDRUM II experiment by a factor 10^4. The search for muon conversion profits from the pulsed structure of the Fermilab and J-PARC proton accelerators as after the formation of the muonic atom a certain amount of time can be waited until the background events stemming from the proton pulse on the muon production target has significantly dropped.

The experiments at PSI needed to adopt a different method to reduce such backgrounds, as the quasi-continuous 50 MHz structure of the proton accelerator at PSI does not allow to implement this strategy. Instead the experiment relied on making the muon beam as pure as possible by strongly reducing the amount of pions transported by the beamline responsible for the largest backgrounds. Figure 28 shows the setup employed by the SINDRUM II experiment. It consisted of the actual spectrometer shown at the end of the beamline used to accurately track and measure the particles emitted from the muon conversion gold target placed at its centre. A transport solenoid connected the spectrometer to the πE5 beamline. At the beginning of the transport solenoid an 8 mm thick CH_2 degrader was placed. The degrader was used to separate the surviving pions in the beam at the momentum of 52 MeV/c through their much shorter range in material compared to muons. The thickness was chosen to stop all pions while most of the muons continued further downstream – guided by the transport solenoid – to the spectrometer. Figure 1 in [24] shows the difference in range for muons and pions in the degrader (however keep in mind that this simulation was performed for monoenergetic beams thus exaggerating the separation power).

In order to see how such an experiment could be improved by HIMB at PSI, let us examine what the improvement in muon rate could be and what strategies could be employed to combat backgrounds at the same time:

- **Muon rate:**
  SINDRUM II was running at a beam momentum of 52 MeV/c in the πE5 area of PSI with an estimated rate of around 2×10^6 μ^-/s available at that time. Due to the limited focusing power of the solenoids used in the HIMB beamline compared to quadrupoles, the momentum reach of the HIMB muon beamlines are limited. Good transmission should be achieved up to a momentum of about 40 MeV/c, at which point it is expected to reach about 10^8 μ^-/s. At this momentum the muon/pion separation separation through a degrader is obviously not as good as in the case of SINDRUM II – see Figure 29. However, due to the lower momentum

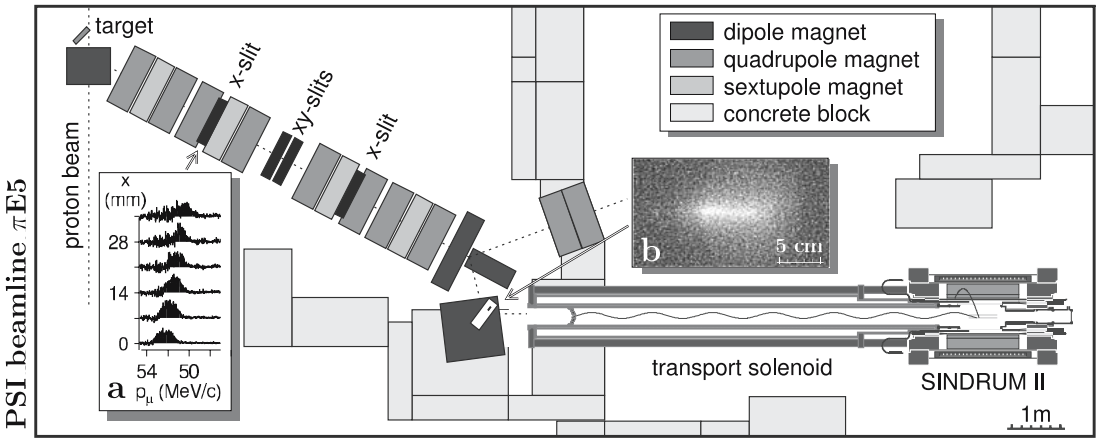

Figure 28: Experimental setup of the SINDRUM II experiment. Muons and pions are produced by the proton beam at Target E and are transported by the πE5 beamline. A degrader located at the beginning of the transport solenoid separates the pions and muons and guides the muons to the SINDRUM II spectrometer located at its end. Picture reproduced from [24], where also more details can be found.

the pion content of the beamline is approximately an order of magnitude lower to start with.

- **Backgrounds:**
  BGs in the SINDRUM II experiment originated mostly from pions decaying in front of or stopping in the degrader. High-energy electrons generated in these decays could reach the spectrometer and mimic the electron produced in the muon conversion process. Different strategies can be employed to reduce the BG to levels much below the ones achieved by SINDRUM II to fully exploit the increased muon rate. i) A spectrometer with modern detector technology as, e.g., employed by the Mu3e experiment (see Section 2.2) will much improve the identification of the electron emitted in the muon conversion process and thus allow for tighter cuts and correspondingly reduced backgrounds. ii) Developments on active targets for such kind of experiments will also provide an additional handle to reduce BGs by uniquely identifying events originating from the conversion target. iii) Using a curved transport solenoid with the degrader at its entrance would eliminate a direct line-of-sight between the degrader and the spectrometer thus stopping any high-energy electrons originating at the degrader from reaching the spectrometer. Similar concepts are also employed by the Mu2e and COMET experiments [27, 28].

Based on the above considerations an improvement of around two orders of magnitude over the sensitivity of the SINDRUM II experiment seems feasible by performing a dedicated and new experiment at HIMB. Given the fact that both Mu2e and COMET aim at reaching four orders of magnitude improved sensitivity, the reach of such an

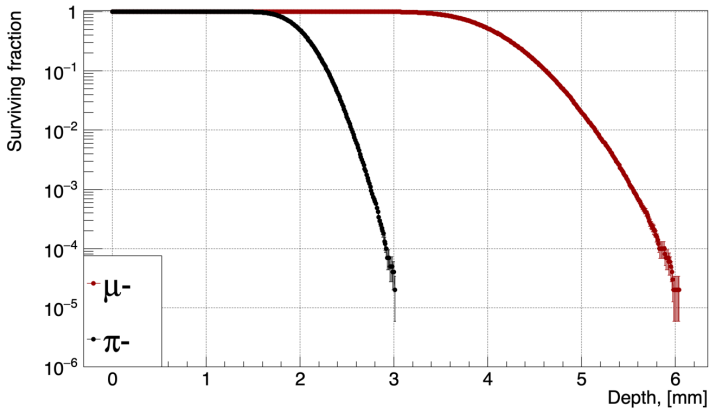

Figure 29: Range of negative pions and muons in a CH_2 degrader at 40 MeV/c and with a momentum resolution of 3%. A degrader with a thickness a bit above 3 mm would be appropriate to nicely separate pions and muons.

experiment at PSI is certainly very limited. The situation could of course change if either these experiments are not able to reach their ultimate sensitivity or detect the muon conversion process with a relatively high branching ratio. At this point, an experiment at HIMB could become interesting – especially as it is hard for the experiments at pulsed beams to work with high-Z conversion targets, which would reveal some insights into the underlying physics of the conversion process [274].

3 Muon spin spectroscopy and material science with HIMB

Muon spin spectroscopy typically uses positive muons as highly sensitive local magnetic probes to study a broad range of research topics in solid-state physics, chemistry and materials science [275]. The experimental techniques referred to as muon spin rotation (μSR) (for Muon Spin Rotation, Relaxation, Resonance or Research) are universally applicable since muons can be implanted in any material. The spin-$\frac{1}{2}$ muons are produced with 100% spin polarisation, providing μSR with a great advantage compared to other local probe methods such as nuclear magnetic resonance (NMR) or electron spin resonance which typically rely upon a tiny thermal equilibrium spin polarisation. The muon is a very sensitive probe of local static and dynamic magnetic properties of materials. Its short mean lifetime of 2.2 μs and relatively large gyromagnetic ratio of $2\pi \times 135.5$ MHz/T makes it suitable for measurements of magnetic fields ranging from $\sim \mu$T to several Tesla, and fluctuating on a time scales from pico- to microseconds. The muon decays into two neutrinos and an energetic positron which is emitted preferentially along the direction of the muon spin, thus providing information on the time evolution of the muon spin polarisation in the investigated material.

Applications of μSR include a large variety of topics in condensed matter research with a focus on the investigation of novel and unconventional magnetic and superconducting

materials. As a local probe, μSR is a powerful tool in this context since it allows studying the detailed nature of magnetic and superconducting phases on a microscopic scale and as a function of control parameters such as doping, temperature, applied magnetic field or pressure. One of the particular advantages of μSR in such measurements is its sensitivity to both the superconducting and magnetic volume fractions, and to their respective order parameters. In the case of superconductors, fundamental microscopic parameters such as the magnetic penetration depth can be determined absolutely. In magnetic materials, μSR is extremely sensitive to small magnetic moments and short range magnetic order. In addition, it is possible to discriminate between static and dynamic magnetism and to characterise magnetic fluctuations within a unique time window, which falls between that of neutron scattering and NMR. Thanks to the volume fraction sensitivity of μSR, the technique is often used to complement scattering probes like X-ray diffraction and neutron scattering where phase volume information is difficult to obtain.

In addition to the common applications of μSR in magnetism and related subjects, it is used to investigate molecular dynamics, charge transport phenomena such as polaron motion in conducting polymers, electron and spin transport as well as ion conduction in technologically relevant battery materials. As a "light isotope" of the proton the μ^+ can form the hydrogen-like exotic atom muonium $[M = (\mu^+ e^-)]$ which may substitute for hydrogen in insulators, semiconductors and organic materials and provide accurate spectroscopic information on hydrogen levels in these materials and their potential for practical applications. As a "light proton isotope", the muon can also serve as a test model for light particle diffusion, radical formation, and chemical reactions with the largest known kinetic isotope effect [276].

The majority of the μSR experiments use one of the following experimental setups, which vary in the orientation of the initial muon spin direction with respect to the external field and the physical information that can be obtained. Very roughly speaking, zero-field μSR allows studying the static magnetic order parameter, the volume fraction and magnetic correlation times. Longitudinal-field (LF, a magnetic field is applied along the initial muon spin direction) μSR is used to discriminate between static and dynamic ground states and to investigate magnetic fluctuations, as well as spin or ion diffusion rates. Transverse-field (TF, a magnetic field is applied perpendicular to the initial muon spin direction) μSR is often used to determine fundamental length scales in superconductors and to measure the q-integrated local susceptibility (Knight shift).

In time-integrated measurements the time evolution of the polarisation is not determined, and the measurements can be carried out at very high muon rates (also at continuous mean beams, because one does not need to have only one muon at a given time in the sample as in time-differential measurements, see Section 3.1). Time-integrated experiments provide information about the energy-level scheme of the muon spin coupled to other spins species (electrons and/or nuclei). Examples are avoided-level-crossing spectroscopy (ALC) or radio-frequency μSR (RF-μSR).

3.1 Different muon sources around the world

Condensed matter research using μSR requires intense muon beams which at present are available at four large scale facilities: the ISIS facility at the Rutherford Appleton Laboratory (UK), the MUSE facility at J-PARC (Japan), the CMMS facility at TRIUMF (Canada) and the Swiss Muon Source (SμS) facility at PSI. The first two are pulsed muon sources with 50 Hz and 25 Hz repetition rates, respectively, while those at TRIUMF and at PSI deliver continuous muon beams. Pulsed and continuous muon sources complement each other allowing for different kinds of experiments. At pulsed sources it is possible to determine very small muon spin relaxation rates due to the virtually zero background between the pulses, but these sources are strongly limited in time resolution due to the 50 – 80 ns width of the muon pulses. In contrast, at continuous sources the time resolution can be up to a factor of thousand better since it is solely determined by the detector construction and the read-out electronics. However, the incoming muon rate has to be reduced compared to a pulsed beam facility to minimise pile-up events. In a traditional μSR setup at a continuous beam, an incoming muon is registered in a muon counter, which opens a data gate of typically 10 μs length. A valid μSR event is given after the detection of the decay positron in one of the scintillators of the positron spectrometer. In case of a pileup event, where a second muon or a second positron is observed within the data gate, it is not possible to determine which muon belongs to which positron, and the event is discarded. At a beam rate of 4×10^4/s, the accepted rate of 1.8×10^4/s is at maximum for a data gate of 10 μs. At beam rates $> 4 \times 10^4$/s, the increasing pile-up probability causes a reduction of the accepted rate to $< 1.8 \times 10^4$/s. In contrast, at pulsed beams, the accepted rate of incoming muons can easily exceed 10^5/s.

The rate limitation at a continuous muon beam could be overcome, if the stopping position of the incoming muon in the studied sample could be detected and the corresponding emitted positron tracked. In this case, each decay positron could be assigned unambiguously to its parent muon by vertex reconstruction, thus allowing for multiple muons to stop in the sample at any given moment. This makes μSR measurements with at least ten times higher incoming muon rates feasible. This paradigm shift for μSR measurements at a continuous source will be discussed in detail in Section 3.3.

3.2 Current status of μSR at PSI

The Laboratory for Muon Spin Spectroscopy (LMU) develops and operates six state-of-the-art instruments of the SμS facility, the worldwide most powerful muon source for condensed-matter research. The six instruments are permanently installed at five separate secondary muon beamlines of the high-intensity proton accelerator cyclotron complex. The different instruments provide the users with a variety of experimental capabilities with respect to temperature, magnetic field, pressure, time resolution, measurement geometry, probing depth and minimal sample size to fulfil the various requirements for the broad scientific spectrum addressed by the Swiss and international user community (see Table 6). To maintain the leading international research position, the μSR instruments need to be kept at the state-of-the-art. This requires a continuous

Instrument	μ^+ energy	T-range	B-range	Comments
DOLLY	4 MeV	0.25 – 300 K	0 – 0.6 T	Unique device for uniaxial strain up to 1 GPa.
FLAME	4 MeV	0.02 – 300 K	0 – 3.5 T	Flexible and Advanced μSR Environment. Begin operation in 2022.
GPD	15 – 60 MeV	0.30 – 500 K	0 – 0.6 T	Unique hydrostatic pressure up to 2.8 GPa.
GPS	4 MeV	1.60 – 1000 K	0 – 0.78 T	General Purpose Instr. Unique MORE capability (Muons On REquest).
HAL-9500	4 MeV	0.01 – 300 K	0 – 9.5 T	Unique combination of low T and very high B. Record time resolution in μSR of 60 ps.
LEM	1 – 30 keV	2.30 – 600 K	0 – 0.3 T	Unique low-energy muon (LE-μ^+) beam and low-energy muon spin rotation (LE-μSR) spectrometer. Thin films & heterostructures. μ^+ range up to 200 nm.
s-Ne	1 – 20 keV			23 kHz moderated μ^+.
s-Ar				14 kHz moderated μ^+.

Table 6: The instruments of SμS with several unique features. T-range and B-range denote the available range of temperatures and magnetic fields, respectively. At all instruments, the muon spin can be rotated between 10° and 90° by so-called spin-rotators ($\vec{E} \times \vec{B}$ fields), or special asymmetric quadrupole settings of the muon beam line (GPD instrument). This allows zero-field-, LF-, and TF-μSR measurements. LEM, s-Ne: solid neon moderator; s-Ar: solid argon moderator. The low-energy muon (LE-μ^+) rates are for a proton current of 2 mA, "slanted" target E [277].

development of new experimental capabilities to be able to address topical and novel research questions.

The research programme at Laboratory for Muon Spin Spectroscopy/SμS includes the "classical" applications of μSR in magnetic materials, superconductors, and semiconductors, as described at the beginning of Section 3 but also goes well beyond this scope. Frontier research topics of recent years include high-spin molecules [278–280], low-dimensional magnets [281, 282], quantum spin liquids [283, 284], organic superconductors [285], conducting polymers [286, 287], liquid crystals [288], topological materials [289–292], defect regions in novel solar-cell materials [293, 294], and defects in semiconductor device heterostructures and near-surface regions [295–297].

Despite the very successful research program at SμS, there are limitations of μSR for the further evolution of the technique towards novel applications and research directions. These limitations, summarised below, are determined by the muon beam and detection characteristics of the μSR spectrometers.

- **Large sample area**: The sample area must be $> 4 \times 4$ mm^2 due to the large phase space of typical muon beams, the limited incoming muon rate and the difficulty in determining whether the muon stopped in the sample or not. For example, this makes it difficult to contribute to the field of some novel quantum materials, which often can be grown with high quality or single crystalline form only in small amounts and small cross sections ($\leq 1 \times 1$ mm^2).

- **Limited muon rate:** As discussed in Section 3.1, the maximum incoming muon rate is limited to about 4×10^4/s due to the pileup problem at continuous muon beams, and the inability of detecting the muon/positron vertex. The accepted muon rate, i.e. those events without pileup, is then limited to only 1.8×10^4/s for a 10-μs data gate of a typical μSR experiment at a continuous beam. This limits the statistical precision of an experiment, compared to pulsed muon sources with $> 10^5$/s accepted muon rate, and it makes it often impossible to investigate very subtle effects like very slow magnetic dynamics or time reversal symmetry breaking in unconventional superconductors.

- **Limited data gate:** Due to the continuous beam, uncorrelated muon-positron events produce a small time-independent background in the μSR spectra. Therefore, the signal to noise ratio gets progressively worse for longer measurement times limiting the available data gate length. This obstructs the measurement of long relaxation times and reduces the frequency resolution for ultra precise Knight shift measurements. These problems can partially be avoided by the use of the so-called Muons On REquest system (MORE) [298] which however reduces the count rate.

- **Limited pressure:** SμS has the world leading μSR high-pressure facility. Due to the limitations in beam spot size and sample size – causing problems with background of muons stopping in the pressure cells, or problems with the mechanical stability of large samples in the device for applying uniaxial pressure – the maximum pressures are 1 GPa and 2.8 GPa for uniaxial and hydrostatic pressures, respectively.

- **Inaccessible depth range:** Due to available beam energies at reasonable rates, the depth range of muons is limited to either < 200 nm [low-energy muon (LE-μ^+)], or ≥ 100 μm by μ^+ with energies > 4 MeV, provided by the surface- or decay-muon beams. The currently accessible depth ranges are shown in Figure 30. There is a big inaccessible gap in the so-called sub-surface muon beam region, which is at energies E_μ between 30 keV and ~ 3.0 MeV, corresponding to muon momenta p_μ of 2.5 MeV/c and 25 MeV/c, respectively.

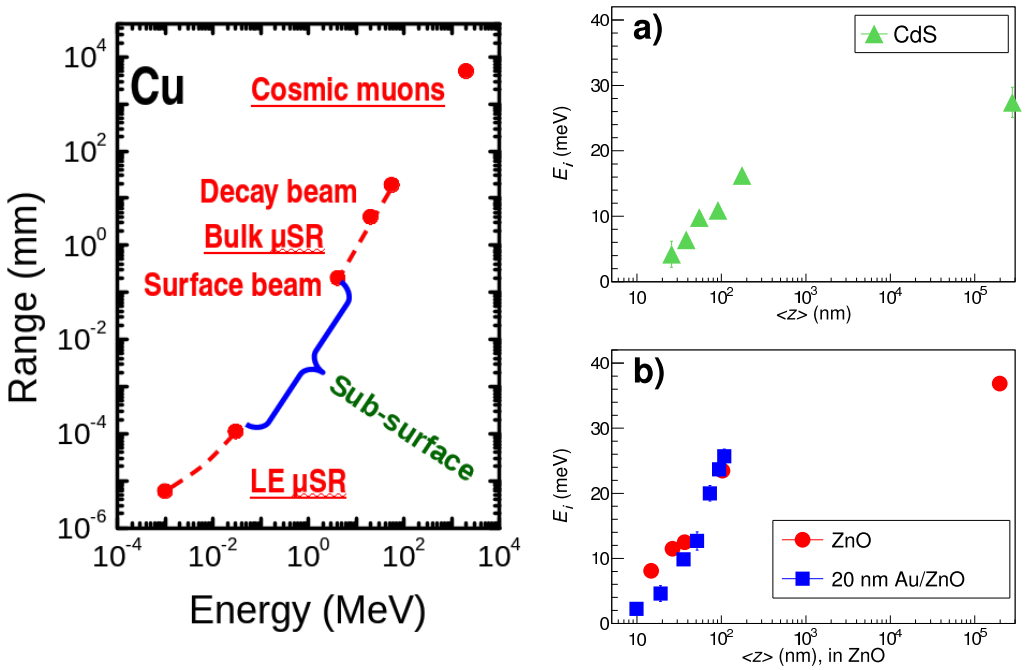

Figure 30: Left: calculated muon stopping ranges in Cu as a function of muon energy. Right: example for the range gap in the determination of the activation energy E_i of shallow muonium as a function of mean depth $\langle z \rangle$ in CdS and ZnO (Reprinted figure with permission from [300]. Copyright 2014 by the American Physical Society.).

The reason for the range gap is the strong dependence on momentum of sub-surface muon beam intensity $I(p)$ [299]

$$I(p) \propto p^{3.5}. \tag{3.1}$$

Already at 25 MeV/c, the beam intensity drops by a factor of two, making it unfeasible to go to even lower beam momenta/energies for μSR applications. Additional complications arise due to the fact that in a standard μSR spectrometer, the muons have to cross a 200-μm-thin scintillator to detect the incoming muon, plus additional thin metal windows in the radiation shield of the cryostat where the sample is located. In these materials, the muons lose tens to hundreds of keV, which requires an incoming beam energy in the MeV range. Note, that this momentum dependence of beam intensity does not apply to the low-energy muon beam at $E_\mu < 30$ keV: these muons are generated by the moderation of a highest-intensity surface muon beam with a $I > 2 \times 10^8$/s in a cryogenic solid moderator (solid argon or solid neon) to generate LE-μ^+ with a rate up to 2.3×10^4/s at the moderator target, see Table 6, and [208, 301, 302].

3.3 New opportunities for μSR at HIMB: key science drivers

HIMB in combination with the novel vertex reconstruction (see Figure 31) – based on the development of a new generation of Si-Pixel detectors (see Section 4.3) – will lead

to a "quantum leap" of the μSR technique, enabling new research directions/science for μSR by much faster, higher statistics and more efficient measurements, extending the depth range of μSR, introducing lateral spatial resolution, and by being able to apply external stimuli with unprecedented levels. The envisaged determination of the muon decay vertex with a precision of $\lesssim 1$ mm will

- enable to measure small samples of cross section ≤ 1 mm^2, at least twenty times smaller than currently possible. It will also allow measuring multiple samples in parallel, thus, for example, determining the phase diagram as a function of doping in one measurement. This is extremely important for the efficient and fast characterisation of novel quantum materials, which can be often grown in small amounts only.

- enable to avoid the pile-up problem by tracking each muon and its corresponding decay positron. The incoming muon beam rate can be significantly increased by at least one order of magnitude compared to the current limit of $\sim 4 \times 10^4$/s. Experiments can be carried out much faster, therefore more efficiently using precious beam time at the two to three times oversubscribed instruments. Due to the significantly enhanced statistics, subtle effects can be detected, for example to measure very slow magnetic fluctuations in quantum materials or detect ultra weak magnetic fields in time reversal symmetry breaking superconductors.

- enable to avoid uncorrelated background in the μSR spectra which allows extending the accessible data gate by at least a factor two. This opens the possibility to measure significantly longer relaxation times and to increase the frequency resolution for high field measurements (Knight shift).

- enable the mapping of imposed lateral variation with $\sim$ mm resolution of sample parameters under chemical, thermal or pressure gradients. This allows measuring extended portions of phase diagrams in one sample or stimulating gradient induced properties like time reversal symmetry breaking in superconductors by thermal gradients.

- enable new opportunities for μSR under extreme conditions. With smaller samples of $\sim$ mm size, the application of about ten times larger uniaxial strain (10 GPa) and hydrostatic pressures (30 GPa) will become possible, allowing the exploration of so far inaccessible regions in the phase diagrams of novel materials.

  Other external stimuli such as illumination or the study under direct current (DC) or radio frequency (RF) electromagnetic fields will become possible with at least one order of magnitude higher intensities/fields. The use of small samples will ease the mitigation of sample heating by more efficient cooling, and it will allow building very compact and mechanically stable and reliable setups. Possible applications are, e.g., novel investigations of charge carrier lifetimes and dynamics in semiconductors by photo-generated carriers, vortex dynamics in superconductors

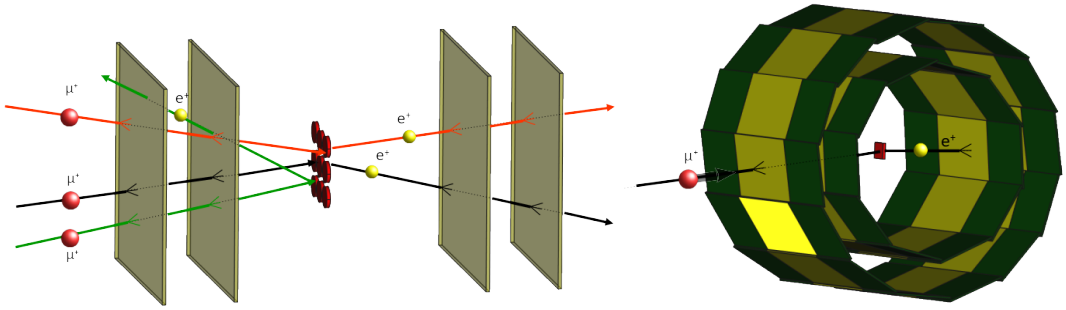

Figure 31: Sketch of the vertex detection scheme for future μSR instruments.

under DC currents, skyrmion dynamics under DC or RF fields, or quantum information processing using molecular spins or skyrmions in pump-probe experiments (see Section 3.3.3).

Besides the exciting new opportunities offered by the combination of HIMB and vertex reconstruction, HIMB will enable i) novel applications in energy materials by closing the range gap between 200 nm and 200 μm (Section 3.3.2 and Table 7), ii) new pump-probe experiments at continuous muon beams (Section 3.3.3), iii) low-energy muon applications with an order of magnitude intensity gain (Section 3.3.4), and iv) significantly improved applications of negative muons in non-destructive, depth-selective elemental analysis studies (Section 3.3.5).

3.3.1 Novel quantum materials

Core activities in condensed matter physics and materials science are the search for, understanding and tuning of phases of quantum materials. μSR as a powerful local probe technique can provide unique insights in the properties of unconventional magnetic and superconducting materials. A large variety of new materials, including those with topologically non-trivial band structures, offer the possibility of realising interesting phenomena, where μSR is a very sensitive experimental technique for their characterisation.

The possibility of measuring ten to hundred times smaller samples, at ten to hundred times higher rates, will have a huge impact on the use of μSR for the investigation of novel quantum materials. In the following, we give a short overview of possible μSR applications with HIMB, which currently can only be carried out to a limited extent or are even unfeasible.

- Higher uniaxial pressure up to 10 GPa due to smaller sample size, which means higher mechanical stability of sample and setup and better homogeneity of samples as well as higher hydrostatic pressure of up to 30 GPa by using high-pressure anvil cells with small sample volumes.
  - Realisation and detection of quantum spin liquids by systematic and symmetry-lowering control of the magnetic interactions by uniaxial strain in kagome,

triangular and Kitaev systems.

  - Tuning of flat-band superconductivity in kagome-lattice systems, for example in $LaRu_3Si_2$, XV_3Sb_5 (X=K, Rb, Cs) and investigation of the interplay of time-reversal symmetry breaking (TRSB), charge density wave (CDW) order and superconductivity in these systems.
  - Investigation of 3D CDW order beyond 1 GPa uniaxial strain in $YBa_2Cu_3O_7$, where only small high quality crystals are available.
  - Hydrostatic and uniaxial pressure tuning of the competition of CDW and superconductivity, e.g. in $NbSe_2$.
  - Uniaxial pressure tuning of stripe order and pair density wave superconductivity in $La_{2-x}Ba_xCuO_4$.
  - Tuning of semiconductor to metal transitions in magnetic layered transition metal dichalgoneides (TMC), e.g. 2H-$MoTe_2$.
  - Pressure tuning of superconducting Weyl semi-metal 1T-$MoTe_2$.
  - Stabilisation and control of topological fermions by tuning of magnetic competition, e.g. in the ferromagnetic Weyl semi-metal $Co_3Sn_2S_2$.
  - Novel low-temperature topological magnetic states in $TbMn_6Sn_6$: pushing topological properties towards room temperature.
  - Strain-induced topological magnon transition in ferromagnetic kagome systems.
  - Tuning of mechanically soft quantum magnets, e.g. $CsFeCl_3$ and $TlCuCl_3$ which is only possible with small specimens.
  - Lifting degeneracy of multi-component unconventional superconductivity, e.g. study of TRSB in Sr_2RuO_4 under strain.
  - Elucidating the source of unconventional high temperature magnetism in Sr_2RuO_4 using high pressure.
  - Local probe investigation of the magnetic and superconducting phase diagram of FeSe under hydrostatic pressures larger than 2 GPa.
  - Strain-tuning of nematicity in Fe-based superconductors.
  - Investigation of two-dome superconductivity in the temperature-pressure phase diagram of $K_{0.8}Fe_{1.7}Se_2$.
  - Black phosphorus as an emerging 2D material: Superconducting phases at pressures up to 20 GPa.
  - Pressure induced superconductivity in elemental Fe.

- Small samples allow application of stronger external stimuli (higher current densities, electric fields or luminosity).
  - Current induced tuning of magnetic properties of iridates.

  - Current induced modification of charge order in the quantum chain systems, e.g. in $(La,Sr,Ca)_{14}Cu_{24}O_{41}$.
  - Microwave / RF induced Skyrmion motion.
  - Current induced vortex lattice dynamics.
  - Manipulation of spin states in molecular magnets using light and microwave irradiation.
  - Spectroscopic investigation of muonium states in semiconductors and insulators.

- Simultaneous measurements of multiple and high quality samples.
  - Much more efficient exploration of phase diagrams (transition temperatures and order parameters) of unconventional superconductors and novel magnets, while thermal and magnetic history are identical for all samples.
  - Precise measurements of Knight shifts and line shapes in superconductors, spin liquids and topological materials, using a reference sample (e.g. Ag) for *in-situ* calibration of magnetic field and detection of field drifts.

- High statistics measurements and low positron background (allows long data gates of 20 μs).
  - Small changes in relaxation rates and internal magnetic fields to investigate TRSB in superconductors.
  - Subtle features in μSR depolarisation function at long times: quantum entanglement and quantum decoherence in F-Mu-F systems.
  - Measurement of decoherence times of spin states in single molecule/ion magnets.
  - Volume fraction of spontaneous magnetic fields in TRSB in unconventional superconductors.
  - Thermal gradients as a source of TRSB fields in unconventional superconductors.

- Laterally resolved μSR measurements.
  - Thermal gradient effects on materials, e.g. spin Seeback effect.
  - Homogeneity of phases in magnetic and superconducting sample.
  - Measurement of the effect of light irradiation intensity on properties of materials in a single shot, e.g. by irradiating with a gradient of light intensity.

This list – although by far not complete – demonstrates the versatile future opportunities for μSR with HIMB combined with vertex reconstruction, allowing a significantly increased access to sample phase space of quantum materials by μSR and thus enabling the exploration of new research avenues by μSR.

3.3.2 Energy materials

In recent years, low-energy muon spin rotation (LE-μSR) has been successfully extended to the study of semiconductor interfaces to provide valuable information – with unprecedented depth resolution of a few nanometres – about charge carrier profiles/gradients and their manipulation by illumination, as well as defect regions in technologically relevant Si and SiC and its oxide interfaces, and defect regions in copper indium gallium selenide (CIGS) based solar cell heterostructures [293–297, 303]. The goal of these studies is to obtain a better microscopic characterisation of device interfaces with a depth resolution superior to standard characterisation techniques, in order to be able to adapt the growth conditions and achieve optimum device efficiency.

Another important extension of μSR demonstrated its capability to measure the Li^+ ion diffusion coefficient, D, in battery materials [304, 305]. In contrast, conventional NMR is unable to provide useful information due to the dominant effect of localised magnetic moments on the NMR spin-lattice relaxation. With the knowledge of D, other crucial parameters relevant for the performance of battery materials can be derived, such as the reactive surface area, diffusion pathway, and density of mobile ions.

So far, these μSR studies are either limited to thin layers/heterostructures with a thickness < 200 nm, or to bulk material. In many cases, semiconductor and solar cell devices as well as real life battery devices have thicknesses in the range of hundreds of nanometres to tens of μm. Therefore, it would be highly appealing to use such a sensitive local probe technique as μSR to study interface and bulk regions in real devices in-operando, to gain unparalleled insights into their function and to enable the development of better devices in future. With the expected intensities of low momentum sub-surface muons at HIMB, as shown in Table 7, the study of buried layers in so far inaccessible depth ranges will become possible, allowing the extension of μSR to become a new in-operando technique for contributing to the solution of important societal problems in energy research.

Table 7: Expected sub-surface muon rates at HIMB for μSR applications, where we assume a surface muon rate of 10^8/s being available in the new μH3 beamline, where the GPS and FLAME instruments are located. This rate is expected downstream of the μH3 spin-rotator. Beam rates calculated using (3.1). Such low beam energies will require the development of new muon entrance detectors.

μ^+ momentum	μ^+ energy	beam rate	mean implantation depth
2.5 MeV/c	30 keV	1.7×10^4/s	$\sim$ 180 nm
3.2 MeV/c	50 keV	4.0×10^4/s	$\sim$ 350 nm
3.8 MeV/c	70 keV	7.4×10^4/s	$\sim$ 500 nm
4.6 MeV/c	100 keV	1.5×10^5/s	$\sim$ 700 nm

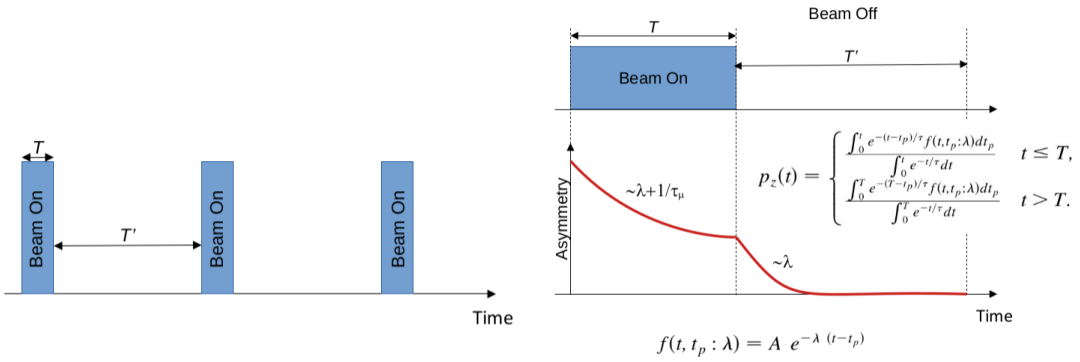

Figure 32: Left: pulsing scheme for chopping the surface muon beam. A possible timing scheme, adjusted to the muon life time, is T = 1 μs, and T$'$ = 19 μs, resulting in a 50 kHz repetition rate. During the pulse of length T, on average about 100 μ^+ will stop in the μSR spectrometer. Right: expected polarisation functions $p_z(t)$ [306].

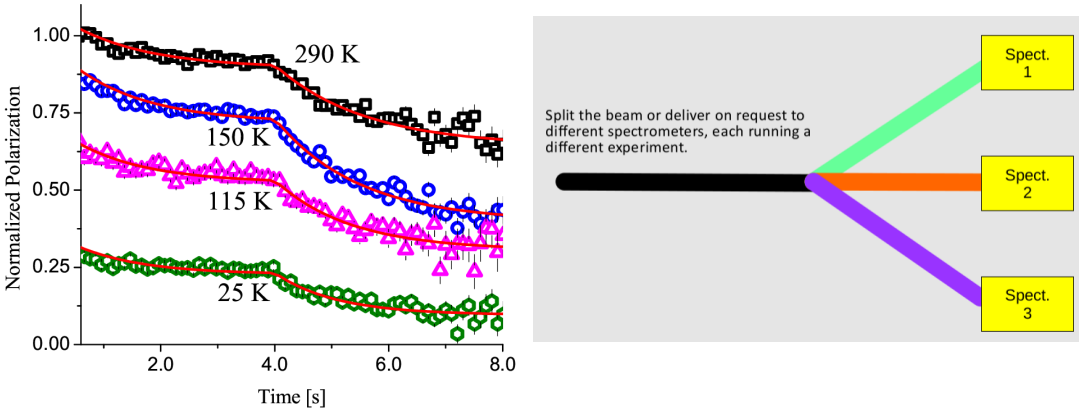

Figure 33: Left: Example for the measurement of spin-lattice relaxation in pulsed β-NMR using radioactive ^{8}Li$^+$ implanted in $SrTiO_3$ (Reprinted figure with permission from [306]. Copyright 2006 by the American Physical Society.). Right: Scheme of multiple instruments on the same muon beamline.

3.3.3 Pulsed beam and pump-probe

The new μH3 beamline at HIMB is expected to deliver a surface muon rate of $> 10^8$/s downstream of the μH3 spin-rotator (see also Table 7). The spin-rotator will significantly cut the initially large phase space, allowing for pulsing/chopping of the continuous surface muon beam. A possible pulse scheme is sketched in Figure 32. During the pulse of a length of T = 1 μs, about 100 μ^+ will enter the μSR spectrometer on average at an incoming rate of 10^8/s. Between the pulses, the measurement is free of accidental background, similar to a pulsed muon beam facility. This technique is already in use at the β-NMR facility at TRIUMF, where a beam of radioactive ^{8}Li$^+$ ions with tunable energies between 1 and 30 keV is used for depth-resolved condensed matter physics

applications in thin films or near-surface regions, see Figure 33, similar to LE-μSR. Compared to μSR, $^8Li^+$ β-NMR is sensitive to much longer times scales due to its orders of magnitude longer lifetime of 1.2 s. For a much more efficient use of beamtime in this scheme, the beam could be split to serve different spectrometers at the same time, as shown on the right side of Figure 33.

Such a scheme of pulsed muon beams, with an average muon rate of 5×10^6/s, will enable new research directions at a continuous muon beam facility:

- The possibility of measuring the effect of external stimuli synchronised with the muon pulse will allow novel μSR applications in quantum information processing with molecular spin systems, magnetic skyrmions etc. For example, quantum states can be prepared in molecular magnet systems and the decoherence time of these states can be measured by μSR. Magnetic skyrmions have the potential to be used as information carriers in future spintronics devices, susceptible to manipulation by very small electric currents or magnetic/electric field pulses. In a magnetic skyrmion system, collective magnon modes can be resonantly stimulated by GHz microwave excitation – ferromagnetic resonance (FMR) – and probed by its effect on the μSR polarisation and the local internal field at the muon site. This combination of FMR-μSR has the potential to examine magnon modes while accessing the internal fields and fluctuations by μSR.

- In general, such a pump-probe scheme can be applied to many systems to gain information about the dynamics in the MHz to GHz range by using light or microwave stimuli, and probe with the muon as a very sensitive local magnetic field sensor. For example, excess carrier lifetimes in semiconductors can be measured by photoexcited μSR [307].

- With this kind of a pulsed beam – similar to a pulsed muon beam facility but with much better time resolution – a long data gate of 20 μs width can be employed due to the very low positron background to measure very small relaxation rates, low muon spin precession frequencies and better resolved split frequencies (e.g. in semiconductors with shallow muonium states). High-statistics measurements would become possible – without vertex reconstruction – to measure very small changes of μSR parameters (see also Section 3.3.1).

- In this pulsing scheme with an effective muon rate in the MHz range, a μSR spectrum can be recorded with sufficient statistics within seconds. This will allow to extend μSR to a new field of applications: the study of transient states with seconds lifetimes. Examples are slow magnetic dynamics, slow chemical reactions and diffusion processes, and vortex creep in superconductors.

3.3.4 Low-energy muons

The current techniques for generating low-energy μ^+ with energies in the eV- and keV-range at continuous muon beam facilities are based on the moderation of a 4-MeV surface muon beam in either a thin film of a solid rare gas (argon or neon) [208, 301] or

in low-pressure He gas placed in superimposed electric and magnetic fields (muCool, see Section 4.2 and [308]). The conversion efficiencies to the eV range are typically small, between 10^{-5} and 10^{-4} per incoming μ^+. This requires very high surface muon beam intensities of $> 10^8$/s to be able to generate 10^3/s – 10^4/s low-energy μ^+. This order of magnitude of LE-μ^+ rates is at the lower limit for practical LE-μSR applications. Obviously, an increase of the 4-MeV surface muon beam rate on the moderator target by one or even two orders of magnitude would have an enormous impact on the entire research program with low-energy muons.

The PSI LEM facility is the leading facility for low-energy μ^+ applications, delivering up to 23 kHz moderated muons. However, taking into account beam transport and detection efficiencies of the LEM facility, the maximum recorded LE-μSR event rate is less than 2.7 kHz at the moment, far below the pile-up limit at a continuous muon beam. This reduces the available statistics of a typical LE-μSR measurement to 10^6 to 10^7 recorded muon decays in the μSR histograms, and thus the investigation of small μSR signals or subtle changes in depolarisation rates and local magnetic fields is not feasible. An additional limitation is the large LE-μ^+ beam spot with a root mean square (RMS) width of 6 – 7 mm. This requires a minimum sample cross section of 10×10 mm^2. For optimum usage of the beam, samples with sizes of 25×25 mm^2 are required. Using a collimator in front of the LE-μSR start detector with 10 mm or 15 mm diameter reduces the beam spot size to RMS values of 3 – 4 mm, while losing 45 – 60% of beam rate.

- An increase of LE-μ^+ rate by one order of magnitude obviously leads to significantly improved LE-μSR experiments with much better statistics and faster measurements. Small samples with 5×5 mm^2 cross section or even smaller will become possible using beam collimation, while compensating the beam loss in the collimator by the increased initial rate after moderation. Such small samples will enable new LE-μSR applications on novel, small size quantum materials and device structures. In addition, experiments under external stimuli such as illumination, electric fields or electric currents can be carried out with much higher light intensities and current densities without excessive heating, therefore expanding the parameter range of LE-μSR to new regions. Current experiments to directly measure the local magnetic field generated by current-induced spin accumulation at the surface/interface (spin Hall effect) are limited by sample heating in the large cross section samples [309]. In samples with 5 times smaller area, the current densities can be increased by a factor 5 (in-plane current) or even a factor 25 (out-of-plane current), therefore bringing the local magnetic field generated by spin accumulation closer to the detection limit of LE-μSR. Furthermore, the quality and homogeneity of electrical contacts can be much better controlled with small sample areas $\ll 25 \times 25$ mm^2, which is the ideal sample size at LEM at the moment. This is important for experiments on new device structures, such as reversible spin storage in metal/metal-oxide/fullerene heterojunctions [310], but also for future applications to study charge carrier dynamics and accumulation/depletion in the presence of defects at technologically important semiconductor interfaces [303] and solar cell devices [293, 294]. For the latter, LE-μSR is used as a local probe technique to

characterise these interfaces with a resolution of a few nanometre with the overall goal to obtain important insights in optimising the growth conditions of these devices.

- With a significant increase of LE-μ^+ rate, about twenty times lower temperatures of $\sim$ 100 mK will become feasible at the LEM facility. At the moment, the lowest temperature of $\sim$ 2.3 K is achieved with a home-made ^{4}He cryostat, where the 6-cm-diameter opening in the radiation shield of the cryostat[8] leads to a thermal load of $\sim$ 200 mW on the sample. A dilution refrigerator (DR), needed to reach $\leq$ 100 mK, has a cooling power of only $\sim \mu$W. This requires a cooling of all surfaces "seen" by the sample to 4 K. Since one needs an opening of several cm diameter in the radiation shield, all the beam pipes with direct view on the sample have to be cooled with liquid ^{4}He. This means, that the existing LE-μ^+ beam at LEM needs to be extended by a section with another bend, where from the bend towards the DR the entire beam section will be cooled. This extension of the beamline will cause a significant loss of at least 50% in transmission, which can be compensated by an increase of the initial LE-μ^+ rate. The possibility of achieving twenty times lower temperatures down to 100 mK or less will open new fascinating applications of LE-μSR in various fields of condensed matter physics, for example:
  - Direct determination of the magnetic penetration depth and coherence length in low temperature superconductors, e.g. the type-I superconductor Al with large κ and a T_c of 1.6 K.
  - Magnetic and superconducting properties of 2D electron gases at interfaces, where coexistence of magnetic and superconducting order at $LaAlO_3/SrTiO_3$ interfaces ($T_c \sim$ 200 mK) was observed [311, 312]. LE-μSR can measure the vortex broadening of the magnetic field distribution in the superconducting state to determine the magnetic penetration depth as a function of temperature. This allows determining the symmetry of the superconducting order parameter.
  - Direct probing of TRSB magnetic fields at the surface of unconventional superconductors with low T_c, e.g. $SrRuO_4$ with $T_c \sim$ 1.5 K [313].
  - Extension of LE-μSR to determine the magnetic penetration depth in unconventional heavy-fermion superconductors. For example, UTe_2 with $T_c \sim$ 1.6 K is showing signs of spin-triplet pairing, TRSB, multiple order parameters and chiral surface states [314].
  - Proximity effects with low-temperature superconductors.
  - Low-temperature magnetism: frustrated magnetic systems, spin-ice and quantum spin liquid systems, and its properties near surfaces or interfaces.
- A beam of LE-μ^+ can be used to efficiently generate muonium in vacuum, which is essential for performing high-precision muonium spectroscopy to provide strin-

[8] LE-μ^+ would stop in any of the typically used μm-thick radiation shield windows.

gent tests of bound state QED and to determine fundamental parameters of the Standard Model (such as muon mass, muon magnetic moment, etc.), as described in Section 2.5. At the LEM facility, the efficient generation of thermal muonium in vacuum has been demonstrated [195, 196], which will enable a new muonium 1s-2s experiment with up to hundred times improved precision [209]. Recently, the efficient generation of a muonium beam in the metastable 2s state [315] has been achieved in the LEM facility, which enabled a ten times more precise measurement of the 2s-Lamb shift in muonium [210]. It is obvious, that the precision of muonium spectroscopy would tremendously benefit from an order of magnitude increase in LE-μ^+ rate.

- A very exciting future opportunity – also pursued at the MUSE facility at J-PARC [316] – is the generation of muon microbeams by re-acceleration of the small phase space of the moderated muon beams to hundreds of keV or even MeV. The moderated muons from muCool might be better suited for this purpose compared to the moderation in a solid argon or neon layer due to the smaller phase space of muCool. However, the extraction of muons from the muCool apparatus and routine operation at a large phase space surface muon beam still need to be demonstrated. A re-accelerated beam of moderated muons would have a much smaller phase space compared to the existing sub-surface and surface muon beams. This would allow focusing the beam on spot sizes of < 1 mm^2, tunable implantation depths from hundreds of nanometre to the μm range, and the realisation of a transmission muon microscope [317] – a novel extension of muon applications to material science. Obviously, this is a further route to completely new muon applications offered by HIMB.

An upgrade of the μE4 beamline is currently being studied, where the use of solenoids instead of quadrupole magnets can yield an improved transmission and focusing on the moderator target. With this upgrade, an increase of about a factor of two of muons on moderator [318] can be expected. However, for full exploitation of the capabilities of LE-μ^+ experiments, LE-μ^+ rates of $> 10^5$/s are highly desirable.

3.3.5 Elemental analysis and μSR

The use of negative muons for non-destructive, elemental analysis by the detection of element-specific muonic X-rays has been tested some decades ago [319, 320], while its routine use has been initiated since 2010 at the pulsed muon sources at J-PARC [321] and ISIS [322]. A main drawback of these studies at pulsed muon sources to date is the use of HPGe detectors, which have long dead times of 5 - 10 μs. This means, that per muon pulse of width 50 - 100 ns, on average only one muonic X-ray can be detected, resulting in an event rate determined by the repetition rate of the muon facility (50 Hz at ISIS, and 25 Hz at J-PARC). This pile-up problem does not exist at a continuous muon beam with a rate of even 100 kHz, where the average distance in time between two muons is 10 μs. A feasibility study at PSI in 2018 has demonstrated (for the setup, see Figure 27, that at the existing πE1 beamline with μ^- rates of about 30 kHz and beam

momentum of ~ 30 MeV/c, the statistics can be increased by more than three orders of magnitude compared to the pulsed muon beam facilities. In addition, active collimation is possible at a continuous muon beam leading to a significant reduction of background. This enables faster measurements with much better signal-to-background ratio, higher sensitivity to low-concentration elements, and the resolution of fine structure splittings and a much better separation of adjacent muonic X-ray lines from different elements.

HIMB has the potential to lead to a significant boost of μ^- applications in elemental analysis:

- With the higher rates, even faster measurements will be possible, and in-operando measurements of devices such as Li-batteries will become feasible, where the diffusion of Li ions through charging/discharging cycles can be monitored as a function of depth.
- Lower beam momenta < 10 MeV/c will become feasible, extending the range of muon stopping depths from ~ 1 μm to > 1 mm.
- Due to the high rates, it will become possible to perform tomography, a very exciting novel extension to image the distribution of elements inside bulky samples and artefacts.
- With HIMB, μ^- could potentially be used in "parasitic mode": the extraction of muons from the new production target H is made by solenoids, transporting μ^+ and μ^- in the same way. At the first bending magnet, a "parasitic beamline" can be installed to transport μ^- – deflected by the opposite angle with respect to the μ^+ – into a separate beamline, where the momentum can be adjusted by a second bending magnet. In this way, a dedicated experimental area for μ^- research would become available without the need to share the beamtime with one of the overbooked μ^+SR instruments.

With higher intensity μ^- beams, a new kind of μ^-SR experiments will become possible: "X-ray triggered μ^-SR" with routing of histograms for individual elements, i.e. "element-specific" μ^-SR. This will open new possibilities to measure element specific diffusion rates and local magnetic fields at element specific lattice sites.

4 The HIMB project & related beam and detector developments

4.1 The HIMB project

The HIMB project aims at delivering $\mathcal{O}(10^{10})$ surface muons per second (positive muons stemming from pion decays at rest close to the surface of the production target [299]) to experiments. To do so, the existing TgM station located in the experimental hall at PSI on the high-energy proton beamline of the HIPA accelerator and its connected beamlines πM1 and πM3 will be completely rebuilt. Figure 34 shows how the layout of

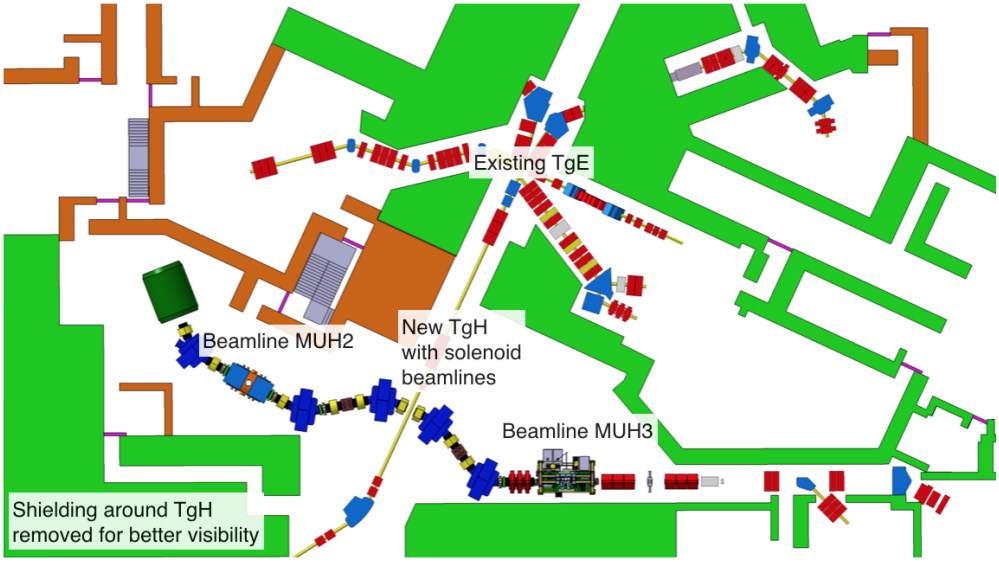

Figure 34: Layout of the new solenoid beamlines in the experimental hall of PSI. The new 20-mm long target TgH is located at the same place as the previous 5-mm long target TgM. The two new beamlines MUH2 and MUH3 replace the two existing beamlines πM1 and πM3.

the new target and beamlines will look like. While the existing graphite target features a length of 5 mm, this will be increased to 20 mm in order to achieve the required rate. Additionally, the target is slanted at 10 degrees with respect to the proton beam such that the overall length of the graphite slab can be increased to 100 mm, while keeping the effective length as seen by the proton beam at 20 mm. This optimisation of the target geometry increases the rate of emitted surface muons by about a factor of two.

The key to reach the intensity goal is to use capture solenoids with a 500-mm aperture located only 250 mm away from the target. Figure 35 shows a cross-section through the two capture solenoids overlaid by the trajectories of surface muons emitted from the target. Already from this picture alone it is clear that a large fraction of the emitted surface muons can be captured by this arrangement and transported further. The capture solenoids will be radiation-hard and are based on the design of two existing solenoids built for the μE4 beamline at PSI [208]. In order to transport the large phase space accepted by the capture solenoids the rest of the beamline also relies on solenoids for focusing combined with large-aperture dipoles. Overall a combined capture and transport efficiency of around 10% is achieved compared to the typical efficiencies of much less than 1% found in the other secondary beamlines of PSI.

HIMB is embedded in the larger IMPACT project that combines two major upgrades of the PSI facilities: HIMB and TATTOOS [323]. The IMPACT project team consisting of people from the PSI divisions NUM (Research with Neutrons and Muons), NES (Nuclear Energy and Safety), BIO (Biology and Chemistry), GFA (Large Research Facilities), and LOG (Logistics) is currently preparing its Conceptual Design Report to be completed by the end of 2021 with the aim of having the project accepted to the 2023

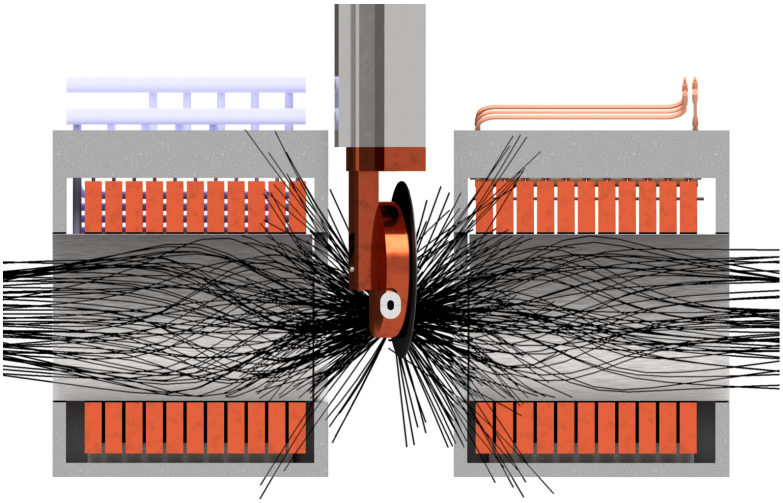

Figure 35: Cross-sectional view of the two capture solenoids together with the new target TgH in the foreground. The black lines show trajectories of surface muons emitted from the target.

Swiss Roadmap for Research Infrastructures. If accepted, its implementation would occur during the period 2025-2028 with regular user operations starting in 2029.

Based on the transported phase space, two scenarios for the beam spot at the final focus were formulated for the HIMB science case workshop depending on the final divergence achievable at the end of the beamline.

HIMB-5:

- 10^{10} μ^+/s at 28 MeV/c and ∼10% momentum-bite (FWHM)
- beam spot $\sigma_{x,y} \sim 50$ mm

HIMB-3:

- 10^{10} μ^+/s at 28 MeV/c and ∼10% momentum-bite (FWHM)
- beam spot $\sigma_{x,y} \sim 30$ mm

These scenarios and especially the achievable rate of 10^{10} μ^+/s formed the basis for the different science cases developed for the workshop and described in this document.

Of course the HIMB beamlines do not only transport surface muons, but also other particles such as negative muons, electrons, positrons, and pions. Figure 36 shows the momentum spectrum of all these particles at the entrance to the capture solenoid. The beamlines are designed for a good transport efficiency up to about 40 MeV/c with the dipoles capable of reaching 80 MeV/c. This allows, e.g., the use of pion beams for calibration purposes albeit not at the highest intensities.

At 28 MeV/c the rates at the end of the beamline are expected to be 2×10^8/s for negative muons, 2×10^{10}/s for positrons, and 7×10^9/s for electrons.

One interesting suggestion raised during the workshop was the notion to study the option of creating a parasitic μ^- beam by splitting at the first dipole of the channel

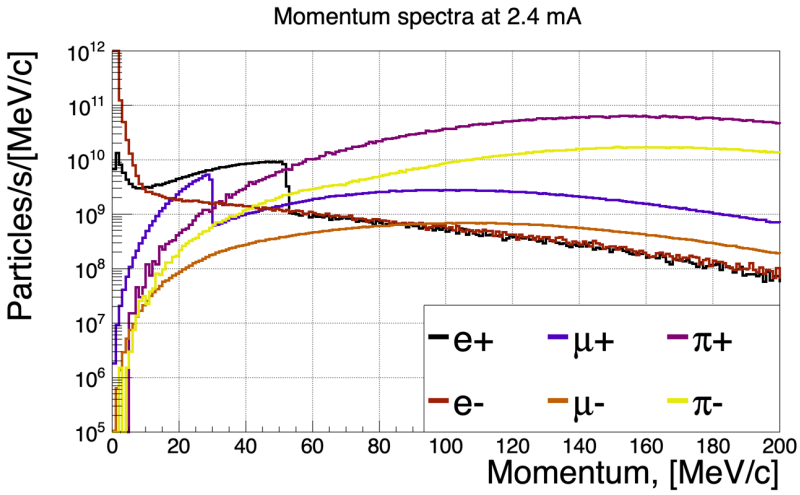

Figure 36: Momentum spectra of positive and negative particles registered at the entrance of the capture solenoid.

the positive and negative muons and thus creating the possibility to simultaneously run experiments with positive and negative muons in two legs of the beamline (see also Section 3.3.5). The feasibility of such an approach is currently under investigation.

4.2 muCool beam development

Experiments with muons at the high-intensity frontier, as experiments searching for lepton flavour violation (see Section 2.1), typically make use of secondary beam lines with large acceptance tuned to transport surface muons with momentum $p = 28$ MeV/c (equivalent to 4 MeV kinetic energy). These muons are copiously created by π^+-decay from pions stopping close to the surface of the pion production target (proton target). Muons of lower momenta, from π^+ decaying below the target surface, can also be extracted and transported by tuning the secondary beam lines for the corresponding momentum. However, because of the momentum straggling in the target, the intensity of these sub-surface muon beams decreases rapidly with momentum ($p^{3.5}$-dependence [299]). The muon scattering in the production target, combined with the large area of the production target and the large acceptance of the secondary beamline, results in muon beams with poor phase space quality. For example the μE4 beam line which has presently the largest muon flux of about 5×10^8 μ^+/s at the moderator is having $\sigma_{x,y} \approx 20$ mm, $\theta_{x,y} \approx 150$ mrad at a momentum of 28 MeV/c and a momentum spread $\Delta p/p \approx 7\%$ (at FWHM) [208]. Other beamlines have slightly smaller phase space at the cost of muon flux [277, 324].

The muCool project aims to transform these beams of 28 MeV/c momentum to a beam with momentum of about 1.5 MeV/c (10 keV kinetic energy) with 0.1 keV energy spread and a phase space of $\sigma_x \sigma_{\theta_x} = 20$ mm mrad with an efficiency ranging from $2 \cdot 10^{-5}$ to $2 \cdot 10^{-4}$. Because such a beam can be easily focused to a sub-mm size it is

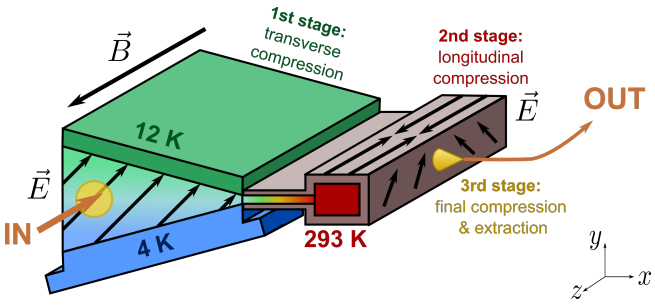

Figure 37: Schematic diagram of the muCool device. A surface muon beam is stopped in a cryogenic He gas target with a vertical temperature gradient inside a 5-T field. The extent of the stopped muons is reduced first in the transverse (y), then in the longitudinal (z) direction using a complex arrangement of E-field and gas density gradient. The compressed muon beam is then extracted through an orifice into vacuum and re-accelerated along the $-z$-direction.

well suited for precision experiments requiring a target with small transverse area and small stopping power or requiring muons to be stopped close to the surface. Moreover, such a beam is well suited for re-acceleration: beams from few keV to 100 MeV energy can be thus obtained by combining the muCool device with a suited acceleration stage opening various possibilities including storage experiments such as the muon EDM and the muon $g-2$ where a small phase space is required.

The proposed muCool compression scheme

In the proposed muCool scheme [325], a surface muon beam propagating in the $-z$-direction is slowed down in a He gas target featuring a strong electric (E) field inside a strong magnetic (B) field as shown in Figure 37. In the slowing-down process, the muon energy is rapidly reduced to the eV range where the E-field becomes important. The E-field, in conjunction with the B-field and gas density gradients, leads to drifting of the slowed-down muons drastically reducing their initially large spatial extent. In this drift process in the gas, the muons are guided to a mm-sized spot. The drift velocity of the μ^+ in a gas with E- and B-fields is given by [326]

$$\vec{v}_D = \frac{\mu|\vec{E}|}{1+\omega^2/\nu^2}\left[\hat{E} + \frac{\omega}{\nu}\hat{E}\times\hat{B} + \frac{\omega^2}{\nu^2}\left(\hat{E}\cdot\hat{B}\right)\hat{B}\right]. \tag{4.1}$$

In (4.1) μ is the muon mobility, $\omega = eB/m$ the cyclotron frequency of the muon, ν the average μ^+–He collision rate, and $\hat{E}$ and $\hat{B}$ the unit vectors of the electric and magnetic fields, respectively.

The spatial extent of the muon stop distribution decreases by making $\vec{v}_D$ position-dependent, so that μ^+ stopped at different locations in the target drift in different directions, and converge to a small spot. This can be achieved by applying a complex E-field pointing in different directions at different positions, and by making the collision frequency ν position-dependent through gas density gradients.

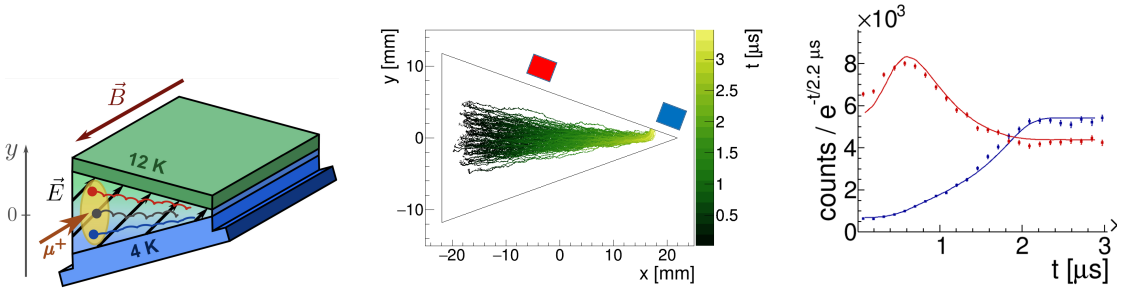

Figure 38: (Left) Sketch of the target used to test the transverse compression at cryogenic temperature with temperature gradient. (Middle) Geant4 simulation of muon trajectories starting at $x \approx -15$ mm and drifting with time in $+x$-direction while compressing in the y-direction. The approximate positions of two plastic scintillators (red, blue) used to measure decay positrons are indicated. (Right) Measured and simulated time spectra for the two plastic scintillators of middle panel. The time zero is given by a counter detecting the muon entering the target. The counts are lifetime compensated.

The muCool setup has been conceived as a sequence of stages having various density and electric field conditions. In the first stage, which is at cryogenic temperatures, the muon beam is stopped and compressed in y-direction (transverse compression). In the second stage, which is at room temperature, the muon beam is compressed in z-direction (longitudinal compression). In the third stage, the muons are extracted from the gas target into vacuum. This extraction is followed by re-acceleration in $-z$-direction to keV energy, and extraction from the B-field.

Demonstration of transverse, longitudinal and mixed compressions

The technology and principle at the core of the muCool cooling scheme, i.e., the ability to move the muon in the He gas with B-field and complex arrangements of E-field and gas density, has been validated in various experiments [308, 327, 328]. The time evolution of the number of decay-positrons hitting the plastic scintillators placed around the targets were used in these experiments to reveal the average motion of the muon ensemble with increasing (decreasing) number of counts indicating muons approaching (leaving) the acceptance region of the considered scintillator. Figure 38 shows a schematic of the setup, a simulation of muon trajectories in the target, and two measurements of the transverse compression [328]. Good agreement between simulated and measured time spectra was observed confirming the validity of our simulation tools and target technology. Similarly Figure 39 demonstrates longitudinal compression.

To avoid the challenging connection between transverse (at cryogenic T) and longitudinal (at room T) stages, a target has been developed and commissioned in which both transverse and longitudinal compressions occur simultaneously (see Figure 40) [329]. Data analysis is still ongoing, but the measured time spectra indicate that a muon stop distribution with volume $\Delta x \times \Delta y \times \Delta z = 10 \times 10 \times 60$ mm^3 can be transformed in

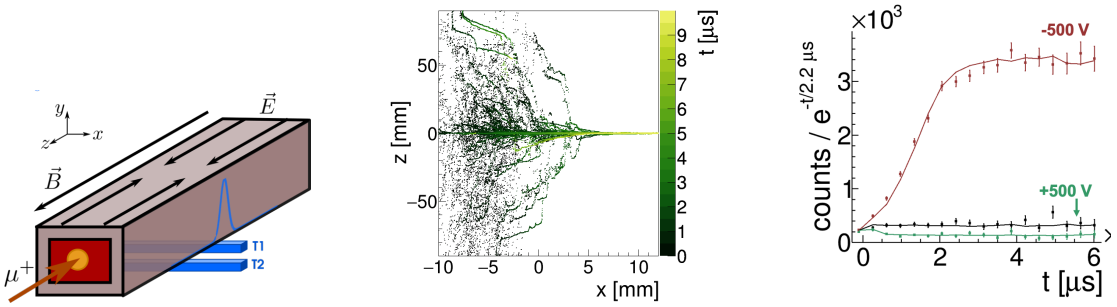

Figure 39: (Left) Sketch of the setup used to test the longitudinal compression at room temperature. The scintillators T1 and T2 in coincidence detect the μ^+ accumulating around $z \approx 0$. The blue curve indicates the region of acceptance for coincident events. (Middle) Simulated μ^+ trajectories. (Right) Measured and simulated time spectra for various HV at the target mid plane: negative HV (red) attracting the muons to the central plane, positive HV (green) repelling them and no HV (black).

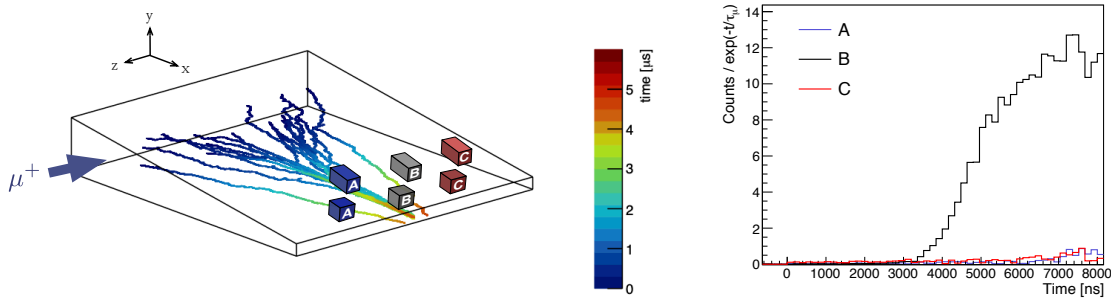

Figure 40: (Left) Simulated muon trajectories in the mixed transverse-longitudinal compression target with a vertical density gradient at cryogenic temperatures, E_x and E_y components as in the transverse compression target, and an E_z component pointing to the target mid-plane at $z = 0$. The positions of the plastic scintillators pairs (A,B,C) used to expose the compression are also shown. (Right) Measured time spectra in the scintillator pairs in coincidence.

5 μs into a beam drifting in x-direction with 10 eV kinetic energy capable of passing an aperture of $\Delta y \times \Delta z = 1 \times 1\,\mathrm{mm}^2$ size with an efficiency of about 50% (excluding muon decay losses).

Vacuum extraction and re-acceleration

A possible extraction scheme that we are presently simulating is shown in Figure 41. It is based on a mixed-compression target modified to allow μ^+ extraction from the gas target into "vacuum" (low density gas region) through an orifice of $1 \times 1\,\mathrm{mm}^2$ aperture. To compensate for the He atoms leaving the target through the same orifice, new He gas is continuously injected at the orifice perpendicular to the μ^+ motion which acts as a gas barrier for the target gas. The injected gas needs to be efficiently evacuated through a system of differentially pumped regions to maintain a good beam quality

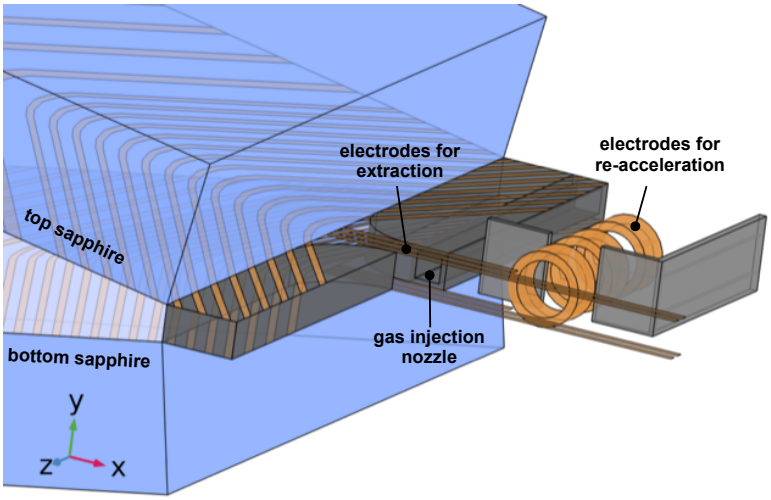

Figure 41: 3D-rendering of the mixed-compression target modified to include an orifice, a He gas inlet, strips of electrodes for muon extraction and drift in $+x$-direction and ring-electrodes for re-acceleration in $-z$-direction. In blue the sapphire plates are shown defining the temperature of the top and bottom target walls, in orange the electrodes defining the electric fields, and in grey the plastic frame of the target.

while the muons are drifted in $+x$-direction using suited electrodes. These muons are eventually coupled into the re-acceleration stage where acceleration in $-z$-direction using ring-shaped electrodes biased at decreasing potentials is occurring.

Projected performance of the complete muCool beam

This section briefly discusses the estimated performance of the HIMB-muCool scheme assuming a muCool target with a single active region for mixed-compression with a performance based on the commissioned mixed-compression target. The efficiencies of the various stages are also summarised in Table 8.

- **Coupling the beam into the solenoid**
  The HIMB beam has an average momentum of 27.7 MeV/c, a large transverse phase space $\sigma_x\sigma_{\theta_x} = 1910$ mm mrad and a large momentum spread of 3.5 MeV/c (FWHM) corresponding to 12.6% momentum bite. Geant4 simulations show that 36% of the muons are back-reflected when injecting on-axis the HIMB beam into a 5 T solenoid of 60 mm inner coil diameter. This fraction becomes 44% for 14° tilt between solenoid and beamline axis to inject the muons 50 mm off the solenoid axis.

- **Coupling the beam into the target**
  Geant4 simulations show that the fringe field of a 5 T solenoid with 60 cm inner-coil diameter focuses the HIMB beam to $\sigma_x \approx \sigma_y \approx 11$ mm. Hence, only a fraction

of 48% of the muons entering the solenoid would impinge on the entrance face (end-cap) of the already commissioned mixed-compression target. For a mixed target with a three times larger side wall (but same target extent in x-direction) this fraction increases to 83%. The feasibility to realise this larger target with the adequate electric field has still to be demonstrated by R&D.

- **Stopping in the active region of the gas target**
  The large momentum spread and transverse momentum distribution of the HIMB beam, in conjunction with the short length of the active region and low density of the target leads to an overall small stopping probability in the region of interest. Geant4 simulations predict that with an optimised moderation at the target entrance, 0.41% of the muons impinging on the entrance face (end-cap) of the target eventually stop in the target's active region. Here we assumed a 50 mm long active region as realised in the commissioned mixed-compression target with a pressure of 10 mbar and a temperature gradient from 6 K to 22 K. We should be able to improve this stopping probability by at least a factor of 1.7 by operating the target at colder temperatures (4 to 16 K gradient) and by elongating the extent of the active region from 50 mm to 60 mm while keeping the same compression efficiency. Moreover, we are presently evaluating a possible reduction of the momentum spread by introducing some dispersion in the HIMB beam in conjunction with a position-dependent moderation.

- **Compression and drift to the orifice region**
  Preliminary analysis of data taken with the commissioned mixed-compression target demonstrates that muons drift and compress with an average kinetic energy smaller than 10 eV from the stopping region of 50 mm length and 10 mm height to the orifice region with an efficiency of 80% in about 5 μs. When including lifetime losses this efficiency is reduced to 8%.

- **Extraction from the gas target through the orifice**
  From preliminary electric fields layouts, Geant4 simulations predict that the compressed muon beam can be extracted from the target with an efficiency of about 50% (neglecting lifetime losses) in about 0.7 μs though an orifice with 1 mm^2 aperture. Including lifetime-losses, this probability becomes thus 40%.

- **Coupling to the re-acceleration region**
  Preliminary simulations of the muon motion from the orifice to the first accelerating ring (where the electrostatic re-acceleration is starting) show that a transport with 90% efficiency (without decay-losses) in 0.5 μs can be obtained. This efficiency is thus about 70%, when accounting for the muon lifetime. The performance of this transport strongly depends on the electric field that can be applied, and the distance muons have to travel before a gas density suited for re-acceleration is reached. Note that muons are injected in the first ring with transverse energies of $\mathcal{O}(20$ eV) and sub-mm size.

Table 8: The first column shows estimated baseline efficiencies of the various muCool stages using the commissioned mixed-compression target as a reference point. We assume here a target with only a single active region (10 mbar, 6-22 K, 50 mm long). The second column shows the room for possible improvements after dedicated R&D, still assuming a single active compression region. All numbers include muon-decay losses.

Baseline Efficiency	Possible Improvements	Description
$5.6 \cdot 10^{-1}$		Coupling to the 5 T solenoid with 60 mm coil diameter
$4.8 \cdot 10^{-1}$	$\times 2$	Impinging on the target entrance-face
$4.1 \cdot 10^{-3}$	$\times 1.6$	Stopping probability in active region of the target
$8 \cdot 10^{-2}$	$\times 1.5$	Compression towards the orifice (within 5 μs)
$4 \cdot 10^{-1}$	$\times 1.3$	Extraction from the orifice
$7 \cdot 10^{-1}$		Drift from orifice to re-acceleration region (in ~ 0.5 μs)
$8 \cdot 10^{-1}$		Re-acceleration and transport to the iron grid
$7 \cdot 10^{-1}$		Transmission through the iron grid terminating the B-field
$1.4 \cdot 10^{-5}$	$\times 6$	Total baseline compression efficiency (and possible improvement)

- **Re-acceleration to 10 keV energy**
  In the static re-acceleration process guided by a series of ring electrodes at decreasing (positive) HV, the only losses are the ones related to the decay during the time of flight. They have been estimated to be about 20%. Some degradation of the beam quality might occur in this stage due to collisions with the rest gas (to be investigated).

- **Extraction from the B-field**
  The extraction of the 10 keV muons from the solenoid is obtained by transporting the muons from the central region of the solenoid at 5 T to a region of 0.01 T field where a grid with 70% transmission terminates abruptly the magnetic field lines. In this transport from high-field to low-field, the transverse beam energy is decreased by a factor of 500 while the beam radius increases by $\sqrt{500}$. At the grid the abrupt termination of the B-field produces a radial field component that impart an azimuthal momentum to the muons of about 3 keV/c (assuming a grid with 2 mm wide apertures) resulting effectively in a beam of 2 mrad divergence. Hence the beam is extracted into a field-free region with a phase space of $\sigma_x \sigma_{\theta_x} \approx 20$ mm mrad (unnormalised) at 10 keV.

As can be seen from Table 8, which summarises the baseline efficiencies of the various muCool stages, a total baseline compression efficiency of $1.4 \cdot 10^{-5}$ is expected from the muCool setup applied to the HIMB. Still assuming a target with a single active region, we expect some room for improving this efficiency with dedicated R&D up to a value of $1 \cdot 10^{-4}$. Moreover, because the stopping probability in the active region of the commissioned mixed-compression target is smaller than 1%, a long muCool target

could be realised having multiple active regions in series along the z-direction, each of them with its own extraction orifice. With some degradation of the 6D phase space, the various outputs can be combined to produce a single more intense muon beam. Alternatively, each of the outputs can be extracted individually from the magnet and sent to various experiments operating simultaneously. The number of active regions in a muCool target in principle can be as high as 100, but practically the required vacuum quality in the acceleration stage will probably limit their number to a few.

In summary, the muCool target transforms the HIMB input beam of 4 MeV energy, with 1 MeV energy spread (at FWHM), and $\sigma_x\sigma_{\theta_x} = 1910$ mm mrad (unnormalised) into a beam of 10 keV with < 0.1 keV energy spread (at FWHM) and $\sigma_x\sigma_{\theta_x} \approx 20$ mm mrad (unnormalised) with an efficiency ranging from $2 \cdot 10^{-5}$ to $1 \cdot 10^{-4}$ assuming a target with a single active region. Such a beam can be focused to sub-mm sized targets and after re-acceleration is well suited for storage-ring experiments. Its efficiency can be further improved by implementing multiple active regions in the same elongated target.

Post-acceleration from 1 to 60 MeV energy

The muon beam delivered by the muCool setup can be further accelerated to the energy appropriate for experiments such as the muon EDM and the muon $g-2$ measurements, where the required muon beam energy ranges from around 1 MeV to 60 MeV or higher. One of the most important parameters of the muon accelerator is the transmission rate: the path length should be minimised because muons are quickly decaying. Circular accelerators therefore may not be optimal, at least in our energy range, due to the fact that the length allocated for acceleration is quite short in comparison to the total path length. Conversely, the linear accelerator (linac) is efficient in this aspect and thus is our baseline choice. As described above, the initial acceleration up to several tens of keV energy will be accomplished simply by setting the ground of the muCool target at positive HV so that the muons leaving the muCool setup are at a kinetic energy basically given by this HV. This electrostatic pre-acceleration provides muons to the linac at a proper energy in a continuous way. For some experiments it may be more convenient to have an extraction in bunches containing several muons. Accumulating the muons for several microseconds before letting them enter the re-acceleration stage is feasible, but at the cost of a largely reduced muon flux due to the 2 μs muon lifetime.

In any case, we design the downstream linacs to be compatible with CW operation as well as a pulsed operation. Among various types of linacs, an RFQ would be well suited to take over the muon beam after the initial acceleration because an RFQ acts like an "all-in-one" cavity, which focuses, bunches and accelerates the beam. An acceleration of negative muonium atoms using an RFQ has been demonstrated in [330]. Our preliminary investigation arrived at a parameter set shown in Table 9. It is proposed to divide the RFQ into two parts, one for capturing and bunching, and the other for the acceleration. This increases flexibility in parameter optimisation drastically.

Two scenarios with a 352-MHz RF system and a 750-MHz RF system are currently considered. The higher frequency system offers a shorter accelerator at the expense of a smaller acceptance and a slightly higher RF power consumption. The transmission

Table 9: RFQ main parameters for two RF frequencies. The normalised emittance corresponds to a geometrical emittance of 40 mm mrad at 10 keV. The intermediate energy is the kinetic energy of the muon beam at the end of the capture section.

Parameters	Values for RF=352 MHz	Values for RF=750 MHz
Input emittance (rms, normalised)	0.55 mm mrad	0.55 mm mrad
Input energy, kinetic	20 keV	20 keV
Intermediate energy, kinetic	170 keV	190 keV
Output energy, kinetic	2 MeV	2 MeV
Output energy spread	0.75%	0.55%
Capture section voltage, vane-to-vane	21 kV	28 kV
Acceleration section voltage, vane-to-vane	65 kV	50 kV
Total length (Capturing/bunching + Accel.)	2.4 + 3.0 m	2.0 + 2.4 m
Beam power	Negligible	Negligible
Power consumption	300 kW (CW)	340 kW (CW)
Transmission efficiency μ-decay not included	96%	94%

efficiency can be sufficiently high for the estimated emittance of 0.55 mm mrad rms (normalised). The muon flux degradation is about 10% for an accelerator length of 5 m. A rough estimation of the costs to build such an accelerator is 250k CHF/m for the accelerating structure and 2.3 million CHF for the 352-MHz RF system. The cost of the RF system includes estimates for a 300-kW solid state power amplifier, waveguides, cooling infrastructure, a local signal source with LLRF-and interlock-system, support structures and cabling. Not included are shielding, manpower, maintenance and running cost. The 750-MHz RF system would be as expensive as the 352-MHz RF system.

In case where the above estimated cost is prohibitive, we may consider to reuse the 500-MHz system of the Swiss Light Source (SLS) which is currently in operation but will be available after the ongoing SLS upgrade provided that the performance of the RFQ is similar at 500 MHz. We need to clarify if this option is cost-effective: how long it can keep up and how much it costs to be refurbished if necessary. Another option is to reduce the duty factor from CW (100%) to a lower value that can be accepted by the experiments. Obviously, this will save running costs, and we also expect a lower cost for the accelerating structure since the cooling part can be simplified.

The power dissipation is estimated for CW operation and fully dominated by the RF wall loss since the muon beam power is negligible. A consumption of several hundred kW is feasible as already demonstrated in high power proton linacs [331]. It is also possible to utilise a superconducting cavity, which offers a highly energy-efficient operation at the expense of higher initial construction cost and increased engineering complexity.

The obtained parameters are for the final energy of 2 MeV. Although it is hard to change the output energy once we built the RFQ, it is straightforward at the design

stage. We simply decrease(increase) the length of the second part of the RFQ cavity if the desired beam energy is lower(higher) than 2 MeV. The final energy is a key parameter driving the overall costs.

The beam is further accelerated for the higher energy applications. The Lorentz beta is still $\ll 1$ at the exit of the RFQ, hence a drift tube linac may be employed. The accelerator chain proposed here is indeed similar to an established layout of proton linac facilities, see e.g. [332]. Other options are, however, to be considered before finalising the accelerator design.

Selected applications for muCool beams (with or without re-acceleration):

This new beam opens the way for next generation experiments with muons and muonium where the reduced phase-space is of great advantage spanning applications in fundamental particle physics, atomic physics and materials science through the μSR technique.

Materials science. The muCool beam can greatly benefit μSR investigations by delivering muons simultaneously to several μSR instruments at the maximum rate allowed by pile-up effects with energy tunability and sub-mm size. Because the pile-up effects in the typically 10 μs-long observation time window become increasingly unsustainable for rates exceeding $4{\cdot}10^4$ μ/s (without vertexing, see Section 3.3), the full HIMB-muCool potential could be exploited by distributing the keV-energy sub-mm beam between several μSR instruments operating simultaneously.

Even assuming the baseline efficiency of $1.4 \cdot 10^{-5}$, the muCool setup injected with $10^{10}\mu$/s from HIMB and provided with an appropriate muon distribution system would be able to deliver muons simultaneously to several μSR instruments with keV energies similar to the present LEM beamline [208] (best performing low-energy beam-line worldwide) but with a sub-mm transverse size instead of the presently cm-size. The number of beams that could be extracted from the muCool setup can be further increased by improving the overall efficiency of the muCool setup and by realising a long muCool target having multiple active regions in series along the z-direction, each of them with its own extraction orifice. Owing to the limited rate acceptance of the μSR instruments (for cw beams), there is no need to merge the beams exiting the various orifices. Each of these beams could be extracted from the solenoid at slightly different off-axis positions with negligible distortion of their beam quality (relative to on-axis extraction).

Hence, the HIMB-muCool scheme would be able to deliver numerous beams, with their number limited only by the technical capability of realising the needed vacuum requirements at the re-acceleration stages. Each of these beam could be easily transported to a compact μSR instrument in a background-free environment capable of analysing sub-mm samples at 50 kHz rate and keV energies. Pile-up effects could be further reduced because the sub-mm low-energy beams can be easily "kicked away" to prevent "second muons" entering the setup in the measurement time window of the "first muon". Combined with high-rates capability, this feature allows the implementation of a muon-on-demand scheme that minimises the dead time of the μSR spectrometer: as soon as a

decay-positron is detected in the spectrometer the next muon is allowed to enter.

The small phase space of the muCool beam is also well suited for efficient re-acceleration to higher energies as discussed previously. Among others, the energy range between 30 keV to a few hundred keV presently not accessible at PSI could be covered.

To reduce the number of μSR instruments, it would also be possible to focus several of the extracted beams from the same muCool target into various samples (or at various locations of a larger sample) mounted in the same μSR spectrometer. Using a positron tracking system (as described in Section 3) it would then be possible to distinguish uniquely the muon decays originating from the various samples in order to disentangle the corresponding time spectra.

Summarising, the HIMB-muCool scheme would improve by an order of magnitude the sample throughput of the PSI μSR facility especially in the keV-energy regime because the muCool device could deliver multiple low-energy beams with 50 kHz rates clean of "second muons". At the same time the transverse beam size would be reduced by more than two orders of magnitude, tremendously benefiting investigations of small samples (see Section 3). Moreover, it also allows muon re-acceleration to energies that are presently not accessible.

High quality muonium sources. Muon to vacuum-muonium conversion is very efficient for keV-energy muons [195]. Hence, the sub-mm muCool beam at keV-energy could be converted into a high-brightness muonium source. This novel muonium source could be exploited to vastly improve on the precision of muonium spectroscopy [209], and for the investigation of the gravitational interaction of muonium [333].

As detailed in Section 2.5, the HIMB-muCool beam opens the way for improving by an order of magnitude the ongoing spectroscopy measurements in muonium: below 1 kHz for the 1S-2S transition and down to few Hz for the HFS. The high muonium rates from the HIMB-muCool will allow accurate studies of systematic uncertainties, the implementation of novel experimental schemes less prone to it, and laser spectroscopy of other transitions.

The combination of the various transition measurements in muonium will lead to: stringent tests of bound-state QED (purely leptonic systems), the best determination of fundamental constants such as the muon mass and the muon magnetic moment, an independent determination of the muon $g-2$ with uncertainty comparable with the present discrepancy, and searches for possible new (beyond the standard model) muon-electron couplings.

As detailed in Section 2.5, the HIMB-muCool beam will also greatly benefit the measurement of the muonium acceleration in the Earth's gravitational field, as a test of the equivalence principle for anti-matter and second-generation particles.

Note in conclusion that several output beams delivered by the muCool setup could be merged on the same spot of a muon-to-muonium converter yielding a muonium source with a flux of several 10^5 muonium/s emitted from a 1 mm spot size.

Storage ring experiments. As detailed in Section 2.4, the search for a muon EDM and the precise measurement of the muon $g-2$ represent well motivated channels for physics beyond the Standard Model. The currently ongoing experiment at Fermilab aims at a measurement of $g-2$ with statistical uncertainty of 0.1 ppm and a similar uncertainty from systematics [189]. With the same apparatus, searches of the muon EDM with a final sensitivity of $1 \cdot 10^{-21}$ e cm will be accomplished. A second collaboration at J-PARC also aims at the same quantities with a combined (statistics + systematic) precision of 0.45 ppm for the $g-2$, and a sensitivity of $1 \cdot 10^{-21}$ e cm for the muon EDM.

The muonEDM collaboration at PSI proposes (see Section 2.4) a search for the muon EDM based on the frozen-spin technique applied to a compact muon storage ring [193]. Preliminary studies show that a sensitivity of $6 \cdot 10^{-23}$ e cm could be reached in the PSI experiment using the μE1 beam at 125 MeV/c delivering $2 \cdot 10^8$ μ^+/s with an average polarisation of better than 93% and assuming a B-field of 3 T. Because of the small phase space acceptance of the storage ring, the coupling efficiency for the μE1 beam is only $2.5 \cdot 10^{-4}$ so that only $5 \cdot 10^4$ μ^+/s are eventually stored in orbit.

The sensitivity to the muon EDM is given by (see Section 2.4)

$$\sigma(d_\mu) = \frac{\hbar}{2\beta\gamma c B P \sqrt{N} \alpha \tau} \tag{4.2}$$

where B is the field strength, P the muon polarisation, N the number of stored muons, α the average decay-asymmetry, τ the muon lifetime, and can be improved with the muCool beam for two reasons: Firstly, owing to its small phase-space the muCool beam can be efficiently coupled into the storage ring resulting in a larger rate of stored muons N. Secondly, owing again to its small phase-space the muCool beam can be efficiently accelerated to larger momenta to increase γ and β. With larger γ and β also the B-field can be increased to keep the optimal radius of curvature. For a storage ring with 5 T field the optimal momentum is around 190 MeV/c.

A muCool target performing approximately at the baseline efficiency followed by a post-acceleration stage would deliver muons with a rate of about $1.4 \cdot 10^5$ s^{-1} so that the rate of muons injected in orbit is increased by a factor of 3 compared to the experiment at the μE1 beamline. R&D on the muCool target has the potential to significantly improve the muon rate delivered to the storage ring. Yet, using a cw beam, i.e., in the scenario where a single muon at a time is analysed in the storage ring, it is essentially impossible to improve the sensitivity beyond $1 \cdot 10^{-23}$ e cm per year of data taking (here we assumed 5 T field and 190 MeV/c momentum). This limitation is originating from pile-up effects.

A small improvement can be obtained by bunching the muCool beam: 5 muons per bunch with 100 kHz repetition rate would result for example in a sensitivity of $8 \cdot 10^{-24}$ e cm per year of measurement. While formation of these bunches is technically possible, the muon-decay losses over the needed accumulation period are severe due to the 2 μs lifetime of the muon. These losses can only be compensated by realising a muCool target with several active regions and by recombining the various outputs at the cost of some energy spread of $\mathcal{O}$(1 keV).

The same setup used to search for the muon EDM can be used, with minor modifications, to measure the muon $g-2$. As detailed in Section 2.4 with a field strength of 6 T and muon on request at 125 MeV/c (that requires in concrete terms a cw beam delivering about $5 \cdot 10^5 \mu$/s) a statistical sensitivity of 0.1 ppm can be reached similar to the ongoing Fermilab experiment. Also in this case, bunching of the muCool beam could be used to improve the measurement down to 0.06 ppm.

An alternative layout is being investigated in which the $g-2$ measurement is performed by injecting muons of only 1 MeV energy into a 17 T solenoid that is acting as mini storage ring. One of the advantages of this scheme is that it requires only the RFQ-acceleration stage but not the linac, reducing size and cost.

Hence, HIMB-muCool has the capability to contribute to two flagship quantities of the present particle physics landscape with high potential for new physics.

In conclusion, the HIMB-muCool complex provides a beam (or multiple beams) that push forward our capabilities where we are already world-leading such as μSR, muonium spectroscopy and fundamental particle physics with muons, while expanding our activities to include storage-ring and gravity experiments.

4.3 Detector developments

To take full advantage of the increased rate of muons provided by HIMB, a new generation of silicon pixel detectors is required. Silicon pixel detectors are used in particle physics for the reconstruction of trajectories of charged particles (tracking) and the identification of vertices from the decay of non-stable particles. Tracking is based on pattern recognition and track fitting and thus requires detectors with high granularity and excellent spatial resolution.

PSI has a long-standing tradition in the design, development and construction of silicon pixel detectors. These detectors have proven their functionality for example in the CMS experiment at the CERN LHC [334–336] and in applications in x-ray photon science at SLS and SwissFEL [337–339]. The pixel detectors used in this context are built using the so-called hybrid technology, in which the particle sensing element and the necessary readout electronics are separate entities, connected using the bump-bonding technique [340].

An alternative approach for pixel detectors is the monolithic technology, where the sensor and readout electronics are parts of the same entity. While CMOS based monolithic active pixel sensor [341] are well known in particle physics, only recently commercially available technologies enable depleted substrates and thus depleted monolithic active pixel sensor (D-MAPS) [31, 342]. The depleted substrate is mandatory for a radiation resistant and fast signal generation and thanks to the full amplification stage and readout architecture being implemented in the silicon sensor chip, much smaller active thickness can be used as the smaller charge signal can be processed without performance degradation. The material budget per layer is significantly reduced as only a single silicon layer is needed and the reduced leakage current due to the lower silicon volume results in relaxed cooling requirements. This makes D-MAPS the most attractive pixel detector concept for future experiments.

In fact, the pixel detector for the Mu3e experiment is being constructed in an HVMAPS technology [32], which allows a high voltage being applied to the silicon substrate to achieve the depletion zone. The MuPix family of chips that has been developed over the past few years [61] allows to build a tracking detector with an unprecedented low-material design [26]. Low-material detectors are key for the reconstruction of the trajectory of the decay positrons to minimise the effect of multiple scattering on the spatial resolution.

The MuPix chips have an active area of $20 \times 20\,\mathrm{mm}^2$ and are thinned down to a thickness of $50\,\mu$m. Using thin high-density interconnect circuits, made of two layers of a substrate of polyimide ($10\,\mu$m) and aluminium ($12\,\mu$m), a detector layer ends up with a radiation length of $\approx 1.15 \times 10^{-3} X_0$. The pixel readout is triggerless and always-on, i.e., every hit in a chip is read out with a time-stamp having a resolution of 15 ns or better. With a pixel pitch of $80\,\mu$m, a position resolution of $23\,\mu$m is achieved.

The next generation of pixel detectors will provide increased granularity in space and time to distinguish particle locations and their interaction times, which is necessary to cope with the high muon flux delivered by HIMB. The evolution of these detector concepts in view of particle physics experiments at HIMB are discussed in Section 2.2.4, Section 2.3.5, and Section 2.4.2.

Pixel detectors also enable new scientific approaches in muon experiments in solid-state physics and materials science, in particular μSR. The spatial and temporal resolution provided by the pixel detector allows for example the measurement of multiple samples in parallel in the same exposure, the separation of domains with different magnetic properties in custom samples as well as to overcome the current limitation in muon rate (as discussed in Section 3).

A concept for a prototype pixel detector for the general purpose surface muon instrument GPS is shown in Figure 42. The pixel detector is built from two concentric cylinders surrounding the cryostat in which the sample is placed. The cylinder axis is placed perpendicular to the muon beam. The pixel detector is used to measure the trajectory of the incoming muon and the outgoing positron, and to reconstruct the muon decay vertex in the sample.

Due to the low momentum of the muons ($< 30\,\mathrm{MeV}$), the spatial resolution of the detector will be dominated by multiple scattering effects and building the detector from minimum material will be crucial. The prototype detector uses a D-MAPS chip of the MuPix family as a sensitive element and all components needed for readout, power and cooling of the detector are placed outside the active area. The prototype detector is built from 34 modules with a total active area of $136\,\mathrm{cm}^2$. The radius of the inner and outer pixel layers are 21 mm and 31 mm, respectively. The detector acceptance determined for a sample of 100'000 simulated muons with an average momentum of 27 MeV is 56%.

The effect of multiple scattering on the resolution has been studied assuming a sensor thickness of $50\,\mu$m and was found to be about 0.65 mm at the muon decay point. The possibility of thinning the sensors to thicknesses of less than $50\,\mu$m is currently being studied. With thinner sensors with a thickness of $30\,\mu$m the resolution can be improved to less than 0.50 mm.

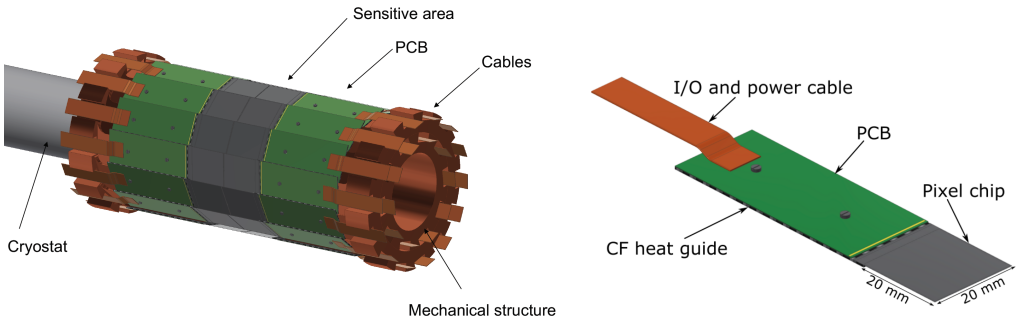

Figure 42: (Left) Drawing of a prototype pixel detector for the general purpose surface muon instrument. The pixel detector is built from two cylindrical layers surrounding the cryostat in which the samples is placed. (Right) Drawing of a pixel detector module. The sensitive element is a D-MAPS chip of the MuPix family developed in the context of the Mu3e experiment.

5 Conclusions

Two new high-intensity muon beams HIMB at PSI with up to two orders of magnitude higher and completely unprecedented intensities of surface muons will boost muon science in many ways. Flavour physics is a hot topic in particle physics, with charged lepton flavour searches and muon electromagnetic moment measurements in particular. Such experiments at HIMB will remain at the forefront of research for the next two decades or longer. Other fundamental atomic, nuclear and particle physics experiments will complement these flagship experiments, testing essentially all known interactions with considerable discovery potential for physics beyond the current Standard Model of particle physics. Likewise, in condensed matter physics HIMB will open up completely new regions of experimental phase space, for smaller sample sizes, for faster spatially and time-resolved measurements, and for depth profiling in so far inaccessible regions. All experiments at HIMB will considerably benefit from technological advances in detector technology, target technology and sample environment. Application of novel technologies, in particular of thin and fast tracking detectors and of new muon beam cooling schemes will further push the boundaries of what is presently possible in muon physics. The physics case for HIMB will continue to develop over time and lead to a definition of an initial physics program at this eagerly awaited new facility. The cases presented here already motivate a very strong and unique program for the next two decades.

Acknowledgements

The science case presented here is built on the work of numerous people over many years and is a true community effort. It is a pleasure to thank all our colleagues at PSI and the external users for their contributions and support. A special thank you goes to all speakers and other participants of the HIMB Science Case workshop of April 2021.

We gratefully acknowledge support by the Swiss National Science Foundation (SNF)

through the grants PCEFP2_181198, PCEFP2_181117, PP00P2_176884, 200441, 197052, 197346; by the European Research Council (ERC) through CoG. 725039, 818053; by the European Union's Horizon 2020 research and innovation programme through grant 858199; by the German Research Foundation (DFG) under Project WA 4157/1; and by the JSPS Core-to-Core Program, A. Advanced Research Networks JPJSCCA20180004 and JSPS KAKENHI Grant Number JP21H04991 (Japan).

References

[1] Joachim Grillenberger et al. "The High Intensity Proton Accelerator Facility". In: *SciPost Phys. Proc.* 5 (2021), p. 002. DOI: 10.21468/SciPostPhysProc.5.002.

[2] "Particle Physics at PSI". In: *SciPost Phys. Proc.* 5 (2021). Ed. by Adrian Signer et al. DOI: 10.21468/SciPostPhysProc.5.

[3] A. Amato. "Heavy-fermion systems studied by μSR technique". In: *Rev. Mod. Phys.* 69 (4 Oct. 1997), pp. 1119–1180. DOI: 10.1103/RevModPhys.69.1119.

[4] Elvezio Morenzoni et al. "Low-Energy Muons at PSI: Examples of Investigations of Superconducting Properties in Near-Surface Regions and Heterostuctures". In: *Proceedings of the International Symposium on Science Explored by Ultra Slow Muon (USM2013)*. DOI: 10.7566/JPSCP.2.010201.

[5] A. Amato et al. "Probing the ground state properties of iron-based superconducting pnictides and related systems by muon-spin spectroscopy". In: *Physica C: Superconductivity* 469.9 (2009). Superconductivity in Iron-Pnictides, pp. 606–613. ISSN: 0921-4534. DOI: 10.1016/j.physc.2009.03.017.

[6] R. Khasanov et al. "High pressure research using muons at the Paul Scherrer Institute". In: *High Pressure Research* 36.2 (2016), pp. 140–166. DOI: 10.1080/08957959.2016.1173690.

[7] Z. Guguchia. "Unconventional Magnetism in Layered Transition Metal Dichalcogenides". In: *Condensed Matter* 5.2 (2020). ISSN: 2410-3896. DOI: 10.3390/condmat5020042.

[8] Tian Shang et al. "Time-Reversal Symmetry Breaking in Re-Based Superconductors: Recent Developments". In: *Frontiers in Physics* 9 (2021), p. 270. ISSN: 2296-424X. DOI: 10.3389/fphy.2021.651163.

[9] Elena Graverini. "Flavour anomalies: a review". In: *J. Phys. Conf. Ser.* 1137.1 (2019). Ed. by Fernando Barão et al., p. 012025. DOI: 10.1088/1742-6596/1137/1/012025. arXiv: 1807.11373 [hep-ex].

[10] Yasmine Sara Amhis et al. "Averages of b-hadron, c-hadron, and τ-lepton properties as of 2018". In: *Eur. Phys. J. C* 81.3 (2021), p. 226. DOI: 10.1140/epjc/s10052-020-8156-7. arXiv: 1909.12524 [hep-ex].

[11] Oliver Fischer et al. "Unveiling Hidden Physics at the LHC". In: (Sept. 2021). arXiv: 2109.06065 [hep-ph].

[12] B. Abi et al. "Measurement of the Positive Muon Anomalous Magnetic Moment to 0.46 ppm". In: *Phys. Rev. Lett.* 126 (Apr. 2021), p. 141801. DOI: 10.1103/PhysRevLett.126.141801. arXiv: 2104.03281 [hep-ex].

[13] G. W. Bennett et al. "Final Report of the Muon E821 Anomalous Magnetic Moment Measurement at BNL". In: *Phys. Rev. D* 73 (2006), p. 072003. DOI: 10.1103/PhysRevD.73.072003. arXiv: hep-ex/0602035.

[14] T. Aoyama et al. “The anomalous magnetic moment of the muon in the Standard Model”. In: *Phys. Rept.* 887 (2020), pp. 1–166. DOI: 10.1016/j.physrep.2020.07.006. arXiv: 2006.04822 [hep-ph].

[15] Lorenzo Calibbi et al. “Charged Lepton Flavour Violation: An Experimental and Theoretical Introduction”. In: *Riv. Nuovo Cim.* 41.2 (2018), pp. 71–174. DOI: 10.1393/ncr/i2018-10144-0. arXiv: 1709.00294 [hep-ph].

[16] S. Weinberg. “Baryon and Lepton Nonconserving Processes”. In: *Phys.Rev.Lett.* 43 (1979), pp. 1566–1570. DOI: 10.1103/PhysRevLett.43.1566.

[17] B. Grzadkowski et al. “Dimension-Six Terms in the Standard Model Lagrangian”. In: *JHEP* 1010 (2010), p. 085. DOI: 10.1007/JHEP10(2010)085. arXiv: 1008.4884 [hep-ph].

[18] Elizabeth E. Jenkins et al. “Low-Energy Effective Field Theory below the Electroweak Scale: Operators and Matching”. In: *JHEP* 03 (2018), p. 016. DOI: 10.1007/JHEP03(2018)016. arXiv: 1709.04486 [hep-ph].

[19] Giovanni Marco Pruna et al. “The $\mu \to e\gamma$ decay in a systematic effective field theory approach with dimension 6 operators”. In: *JHEP* 10 (2014), p. 014. DOI: 10.1007/JHEP10(2014)014. arXiv: 1408.3565 [hep-ph].

[20] Andreas Crivellin et al. “Renormalisation-group improved analysis of $\mu \to e$ processes in a systematic effective-field-theory approach”. In: *JHEP* 05 (2017), p. 117. DOI: 10.1007/JHEP05(2017)117. arXiv: 1702.03020 [hep-ph].

[21] Robert H. Bernstein et al. “Charged Lepton Flavor Violation: An Experimenter’s Guide”. In: *Phys. Rept.* 532 (2013), pp. 27–64. DOI: 10.1016/j.physrep.2013.07.002. arXiv: 1307.5787 [hep-ex].

[22] U. Bellgardt et al. “Search for the Decay $\mu^+ \to e^+e^+e^-$”. In: *Nucl. Phys. B* 299 (1988), pp. 1–6. DOI: 10.1016/0550-3213(88)90462-2.

[23] A. M. Baldini et al. “Search for the lepton flavour violating decay $\mu^+ \to \mathrm{e}^+\gamma$ with the full dataset of the MEG experiment”. In: *Eur. Phys. J. C* 76.8 (2016), p. 434. DOI: 10.1140/epjc/s10052-016-4271-x. arXiv: 1605.05081 [hep-ex].

[24] Wilhelm H. Bertl et al. “A Search for muon to electron conversion in muonic gold”. In: *Eur. Phys. J. C* 47 (2006), pp. 337–346. DOI: 10.1140/epjc/s2006-02582-x.

[25] A. M. Baldini et al. “The design of the MEG II experiment”. In: *Eur. Phys. J. C* 78.5 (2018), p. 380. DOI: 10.1140/epjc/s10052-018-5845-6. arXiv: 1801.04688 [physics.ins-det].

[26] K. Arndt et al. “Technical design of the phase I Mu3e experiment”. In: *Nucl. Instrum. Meth. A* 1014 (2021), p. 165679. DOI: 10.1016/j.nima.2021.165679. arXiv: 2009.11690 [physics.ins-det].

[27] R. Abramishvili et al. “COMET Phase-I Technical Design Report”. In: *PTEP* 2020.3 (2020), p. 033C01. DOI: 10.1093/ptep/ptz125. arXiv: 1812.09018 [physics.ins-det].

[28] L. Bartoszek et al. "Mu2e Technical Design Report". In: (Oct. 2014). DOI: 10.2172/1172555. arXiv: 1501.05241 [physics.ins-det].

[29] Gilberto Colangelo et al. "A theory vade mecum for PSI experiments". In: *SciPost Phys. Proc.* 5 (2021), p. 005. DOI: 10.21468/SciPostPhysProc.5.005. arXiv: 2109.11948 [hep-ph].

[30] A. Blondel et al. "Research Proposal for an Experiment to Search for the Decay $\mu \to eee$". In: (Jan. 2013). arXiv: 1301.6113 [physics.ins-det].

[31] Ivan Peric. "A novel monolithic pixelated particle detector implemented in high-voltage CMOS technology". In: *Nucl. Instrum. Meth. A* 582 (2007). Ed. by Giovanni Ambrosi et al., pp. 876–885. DOI: 10.1016/j.nima.2007.07.115.

[32] Ivan Perić et al. "High-voltage pixel detectors in commercial CMOS technologies for ATLAS, CLIC and Mu3e experiments". In: *Nucl. Instrum. Meth. A* 731 (2013). Ed. by Yoshinobu Unno et al., pp. 131–136. DOI: 10.1016/j.nima.2013.05.006.

[33] N. Grefkes. "Mu3e Final Focus Study". Bachelor Thesis. Heidelberg University, 2021.

[34] Ann-Kathrin Perrevoort. "Sensitivity Studies on New Physics in the Mu3e Experiment and Development of Firmware for the Front-End of the Mu3e Pixel Detector". PhD thesis. Heidelberg University, 2018. DOI: 10.11588/heidok.00024585.

[35] Ann-Kathrin Perrevoort. "The Rare and Forbidden: Testing Physics Beyond the Standard Model with Mu3e". In: *SciPost Phys. Proc.* 1 (2019), p. 052. DOI: 10.21468/SciPostPhysProc.1.052. arXiv: 1812.00741 [hep-ex].

[36] Wilhelm H. Bertl et al. "Search for the Decay $\mu^+ \to e^+e^+e^-$". In: *Nucl. Phys. B* 260 (1985), pp. 1–31. DOI: 10.1016/0550-3213(85)90308-6.

[37] G.M. Pruna et al. "Fully differential NLO predictions for the rare muon decay". In: *Phys. Lett. B* 765 (2017), pp. 280–284. DOI: 10.1016/j.physletb.2016.12.039. arXiv: 1611.03617 [hep-ph].

[38] Sean Hughes. "Background studies for the Mu3e experiment". PhD thesis. Liverpool University. In preparation.

[39] L. Paolozzi et al. "Characterization of the demonstrator of the fast silicon monolithic ASIC for the TT-PET project". In: *Journal of Instrumentation* 14.02 (2019), P02009–P02009. DOI: 10.1088/1748-0221/14/02/p02009.

[40] D. vom Bruch. "Pixel Sensor Evaluation and Online Event Selection for the Mu3e Experiment". PhD thesis. Heidelberg University, 2017.

[41] Dorothea vom Bruch. "Track and Vertex Reconstruction on GPUs for the Mu3e Experiment". In: *GPU Computing in High-Energy Physics*. June 2015. DOI: 10.3204/DESY-PROC-2014-05/13.

[42] Dorothea vom Bruch. "Online Data Reduction using Track and Vertex Reconstruction on GPUs for the Mu3e Experiment". In: *EPJ Web Conf.* 150 (2017). Ed. by C. Germain et al., p. 00013. DOI: 10.1051/epjconf/201715000013.

[43] Alexandr Kozlinskiy. "Track reconstruction for the Mu3e experiment based on a novel Multiple Scattering fit". In: *EPJ Web Conf.* 150 (2017). Ed. by C. Germain et al., p. 00005. DOI: 10.1051/epjconf/201715000005.

[44] Niklaus Berger et al. "A New Three-Dimensional Track Fit with Multiple Scattering". In: *Nucl. Instrum. Meth. A* 844 (2017), p. 135. DOI: 10.1016/j.nima.2016.11.012. arXiv: 1606.04990 [physics.ins-det].

[45] A. Kozlinskiy et al. "A new track reconstruction algorithm for the Mu3e experiment based on a fast multiple scattering fit". In: *JINST* 9.12 (2014), p. C12012. DOI: 10.1088/1748-0221/9/12/C12012.

[46] S. Schenk. "A fast vertex fit for the Mu3e experiment". Bachelor Thesis. Heidelberg University, 2013.

[47] G. Aad et al. "The ATLAS Fast TracKer system". In: *JINST* 16 (2021), P07006. DOI: 10.1088/1748-0221/16/07/P07006. arXiv: 2101.05078 [physics.ins-det].

[48] Sebastian Dittmeier. "The ATLAS Hardware Track Trigger design towards first prototypes". In: *PoS* Vertex2019 (2020), p. 049. DOI: 10.22323/1.373.0049.

[49] H. Leuschner. "Mu3e-γ upgrade simulations for the Mu3e experiment". Master Thesis. Heidelberg University, 2019.

[50] MEG II collaboration A. M. Baldini et al. "The Search for $\mu^+ \to e^+\gamma$ with 10^{-14} Sensitivity: The Upgrade of the MEG Experiment". In: *Symmetry* 13 (2021), p. 19. DOI: 10.3390/sym13091591.

[51] G. F. Tassielli et al. "The Drift Chamber of the MEG II experiment". In: *JINST* 15.09 (2020), p. C09051. DOI: 10.1088/1748-0221/15/09/C09051. arXiv: 2006.02378 [physics.ins-det].

[52] G. Chiarello et al. "Application of the Cluster Counting/Timing techniques to improve the performances of high transparency Drift Chamber for modern HEP experiments". In: *JINST* 12.07 (2017). Ed. by Lev Shekhtman, p. C07021. DOI: 10.1088/1748-0221/12/07/C07021.

[53] Giovanni F. Tassielli. "A proposal of a drift chamber for the IDEA experiment for a future e+e- collider". In: *PoS* ICHEP2020 (2021), p. 877. DOI: 10.22323/1.390.0877.

[54] G. Bencivenni et al. "An ultra-light cylindrical GEM detector as inner tracker at KLOE-2". In: *Nucl. Instrum. Meth. A* 581 (2007). Ed. by Josef Hrubec et al., pp. 221–224. DOI: 10.1016/j.nima.2007.07.082.

[55] G. Bencivenni et al. "The micro-Resistive WELL detector: a compact spark-protected single amplification-stage MPGD". In: *JINST* 10.02 (2015), P02008. DOI: 10.1088/1748-0221/10/02/P02008. arXiv: 1411.2466 [physics.ins-det].

[56] Bernhard Ketzer. "A Time Projection Chamber for High-Rate Experiments: Towards an Upgrade of the ALICE TPC". In: *Nucl. Instrum. Meth. A* 732 (2013). Ed. by T. Bergauer et al., pp. 237–240. DOI: 10.1016/j.nima.2013.08.027. arXiv: 1303.6694 [physics.ins-det].

[57] M. Ahmed et al. "Search for the lepton family number nonconserving decay $\mu^+ \to e^+\gamma$". In: *Phys. Rev. D* 65 (2002), p. 112002. DOI: 10.1103/PhysRevD.65.112002. arXiv: hep-ex/0111030.

[58] P. A. Zyla et al. "Review of Particle Physics". In: *PTEP* 2020.8 (2020), p. 083C01. DOI: 10.1093/ptep/ptaa104.

[59] Atsushi Oya et al. "Development of high-rate capable and ultra-low mass Resistive Plate Chamber with Diamond-Like Carbon". In: Sept. 2021. arXiv: 2109.13525 [physics.ins-det].

[60] Naoki Tsuji et al. "Study on Granularity Optimization for ILD Hadron Calorimeter". In: *JPS Conf. Proc.* 27 (2019), p. 012015. DOI: 10.7566/JPSCP.27.012015.

[61] A. Schöning et al. "MuPix and ATLASPix – Architectures and Results". In: *PoS* Vertex2019 (2020), p. 024. DOI: 10.22323/1.373.0024. arXiv: 2002.07253 [physics.ins-det].

[62] Julian S. Schwinger. "On Quantum electrodynamics and the magnetic moment of the electron". In: *Phys. Rev.* 73 (1948), pp. 416–417. DOI: 10.1103/PhysRev.73.416.

[63] P. Kusch et al. "The Magnetic Moment of the Electron". In: *Phys. Rev.* 74.3 (1948), p. 250. DOI: 10.1103/PhysRev.74.250.

[64] D. Hanneke et al. "New Measurement of the Electron Magnetic Moment and the Fine Structure Constant". In: *Phys. Rev. Lett.* 100 (2008), p. 120801. DOI: 10.1103/PhysRevLett.100.120801. arXiv: 0801.1134 [physics.atom-ph].

[65] Stefano Laporta. "High-precision calculation of the 4-loop contribution to the electron g-2 in QED". In: *Phys. Lett. B* 772 (2017), pp. 232–238. DOI: 10.1016/j.physletb.2017.06.056. arXiv: 1704.06996 [hep-ph].

[66] Tatsumi Aoyama et al. "Theory of the Anomalous Magnetic Moment of the Electron". In: *Atoms* 7.1 (2019), p. 28. DOI: 10.3390/atoms7010028.

[67] Alexander Keshavarzi et al. "The $g-2$ of charged leptons, $\alpha(M_Z^2)$ and the hyperfine splitting of muonium". In: *Phys. Rev.* D101 (2020), p. 014029. DOI: 10.1103/PhysRevD.101.014029. arXiv: 1911.00367 [hep-ph].

[68] Sergey Volkov. "Calculating the five-loop QED contribution to the electron anomalous magnetic moment: Graphs without lepton loops". In: *Phys. Rev. D* 100.9 (2019), p. 096004. DOI: 10.1103/PhysRevD.100.096004. arXiv: 1909.08015 [hep-ph].

[69] Richard H. Parker et al. "Measurement of the fine-structure constant as a test of the Standard Model". In: *Science* 360 (2018), p. 191. DOI: 10.1126/science.aap7706. arXiv: 1812.04130 [physics.atom-ph].

[70] Léo Morel et al. "Determination of the fine-structure constant with an accuracy of 81 parts per trillion". In: *Nature* 588.7836 (2020), pp. 61–65. DOI: 10.1038/s41586-020-2964-7.

[71] T. Albahri et al. “Measurement of the anomalous precession frequency of the muon in the Fermilab Muon $g-2$ experiment”. In: *Phys. Rev. D* 103 (2021), p. 072002. DOI: 10.1103/PhysRevD.103.072002. arXiv: 2104.03247 [hep-ex].

[72] T. Albahri et al. “Magnetic Field Measurement and Analysis for the Muon $g-2$ Experiment at Fermilab”. In: *Phys. Rev. A* 103 (2021), p. 042208. DOI: 10.1103/PhysRevA.103.042208. arXiv: 2104.03201 [hep-ex].

[73] T. Albahri et al. “Beam dynamics corrections to the Run-1 measurement of the muon anomalous magnetic moment at Fermilab”. In: *Phys. Rev. Accel. Beams* 24 (2021), p. 044002. DOI: 10.1103/PhysRevAccelBeams.24.044002. arXiv: 2104.03240 [physics.acc-ph].

[74] J. Grange et al. “Muon $(g-2)$ Technical Design Report”. In: (Jan. 2015). arXiv: 1501.06858 [physics.ins-det].

[75] M. Abe et al. “A New Approach for Measuring the Muon Anomalous Magnetic Moment and Electric Dipole Moment”. In: *PTEP* 2019.5 (2019), p. 053C02. DOI: 10.1093/ptep/ptz030. arXiv: 1901.03047 [physics.ins-det].

[76] T. P. Gorringe et al. “Precision Muon Physics”. In: *Prog. Part. Nucl. Phys.* 84 (2015), pp. 73–123. DOI: 10.1016/j.ppnp.2015.06.001. arXiv: 1506.01465 [hep-ex].

[77] Tatsumi Aoyama et al. “Complete Tenth-Order QED Contribution to the Muon $g-2$”. In: *Phys. Rev. Lett.* 109 (2012), p. 111808. DOI: 10.1103/PhysRevLett.109.111808. arXiv: 1205.5370 [hep-ph].

[78] Andrzej Czarnecki et al. “Refinements in electroweak contributions to the muon anomalous magnetic moment”. In: *Phys. Rev.* D67 (2003). [Erratum: Phys. Rev. D73, 119901 (2006)], p. 073006. DOI: 10.1103/PhysRevD.67.073006. arXiv: hep-ph/0212229 [hep-ph].

[79] C. Gnendiger et al. “The electroweak contributions to $(g-2)_\mu$ after the Higgs boson mass measurement”. In: *Phys. Rev.* D88 (2013), p. 053005. DOI: 10.1103/PhysRevD.88.053005. arXiv: 1306.5546 [hep-ph].

[80] Michel Davier et al. “Reevaluation of the hadronic vacuum polarisation contributions to the Standard Model predictions of the muon $g-2$ and $\alpha(m_Z^2)$ using newest hadronic cross-section data”. In: *Eur. Phys. J.* C77.12 (2017), p. 827. DOI: 10.1140/epjc/s10052-017-5161-6. arXiv: 1706.09436 [hep-ph].

[81] Alexander Keshavarzi et al. “Muon $g-2$ and $\alpha(M_Z^2)$: a new data-based analysis”. In: *Phys. Rev.* D97.11 (2018), p. 114025. DOI: 10.1103/PhysRevD.97.114025. arXiv: 1802.02995 [hep-ph].

[82] Gilberto Colangelo et al. “Two-pion contribution to hadronic vacuum polarization”. In: *JHEP* 02 (2019), p. 006. DOI: 10.1007/JHEP02(2019)006. arXiv: 1810.00007 [hep-ph].

[83] Martin Hoferichter et al. "Three-pion contribution to hadronic vacuum polarization". In: *JHEP* 08 (2019), p. 137. DOI: 10.1007/JHEP08(2019)137. arXiv: 1907.01556 [hep-ph].

[84] M. Davier et al. "A new evaluation of the hadronic vacuum polarisation contributions to the muon anomalous magnetic moment and to $\alpha(m_Z^2)$". In: *Eur. Phys. J.* C80.3 (2020). [Erratum: Eur. Phys. J. C80, 410 (2020)], p. 241. DOI: 10.1140/epjc/s10052-020-7792-2. arXiv: 1908.00921 [hep-ph].

[85] Alexander Kurz et al. "Hadronic contribution to the muon anomalous magnetic moment to next-to-next-to-leading order". In: *Phys. Lett.* B734 (2014), pp. 144–147. DOI: 10.1016/j.physletb.2014.05.043. arXiv: 1403.6400 [hep-ph].

[86] Kirill Melnikov et al. "Hadronic light-by-light scattering contribution to the muon anomalous magnetic moment revisited". In: *Phys. Rev.* D70 (2004), p. 113006. DOI: 10.1103/PhysRevD.70.113006. arXiv: hep-ph/0312226 [hep-ph].

[87] Pere Masjuan et al. "Pseudoscalar-pole contribution to the $(g_\mu - 2)$: a rational approach". In: *Phys. Rev.* D95.5 (2017), p. 054026. DOI: 10.1103/PhysRevD.95.054026. arXiv: 1701.05829 [hep-ph].

[88] Gilberto Colangelo et al. "Dispersion relation for hadronic light-by-light scattering: two-pion contributions". In: *JHEP* 04 (2017), p. 161. DOI: 10.1007/JHEP04(2017)161. arXiv: 1702.07347 [hep-ph].

[89] Martin Hoferichter et al. "Dispersion relation for hadronic light-by-light scattering: pion pole". In: *JHEP* 10 (2018), p. 141. DOI: 10.1007/JHEP10(2018)141. arXiv: 1808.04823 [hep-ph].

[90] Antoine Gérardin et al. "Lattice calculation of the pion transition form factor with $N_f = 2 + 1$ Wilson quarks". In: *Phys. Rev.* D100.3 (2019), p. 034520. DOI: 10.1103/PhysRevD.100.034520. arXiv: 1903.09471 [hep-lat].

[91] Johan Bijnens et al. "Short-distance constraints for the HLbL contribution to the muon anomalous magnetic moment". In: *Phys. Lett.* B798 (2019), p. 134994. DOI: 10.1016/j.physletb.2019.134994. arXiv: 1908.03331 [hep-ph].

[92] Gilberto Colangelo et al. "Longitudinal short-distance constraints for the hadronic light-by-light contribution to $(g-2)_\mu$ with large-N_c Regge models". In: *JHEP* 03 (2020), p. 101. DOI: 10.1007/JHEP03(2020)101. arXiv: 1910.13432 [hep-ph].

[93] Thomas Blum et al. "The hadronic light-by-light scattering contribution to the muon anomalous magnetic moment from lattice QCD". In: *Phys. Rev. Lett.* 124.13 (2020), p. 132002. DOI: 10.1103/PhysRevLett.124.132002. arXiv: 1911.08123 [hep-lat].

[94] Gilberto Colangelo et al. "Remarks on higher-order hadronic corrections to the muon $g-2$". In: *Phys. Lett.* B735 (2014), pp. 90–91. DOI: 10.1016/j.physletb.2014.06.012. arXiv: 1403.7512 [hep-ph].

[95] G Abbiendi et al. *Letter of Intent: the MUonE project*. Tech. rep. CERN-SPSC-2019-026, SPSC-I-252. June 2019. URL: https://cds.cern.ch/record/2677471.

[96] Pulak Banerjee et al. "Theory for muon-electron scattering @ 10 ppm: A report of the MUonE theory initiative". In: *Eur. Phys. J. C* 80.6 (2020), p. 591. DOI: 10.1140/epjc/s10052-020-8138-9. arXiv: 2004.13663 [hep-ph].

[97] Sz. Borsanyi et al. "Leading hadronic contribution to the muon magnetic moment from lattice QCD". In: *Nature* 593.7857 (2021), pp. 51–55. DOI: 10.1038/s41586-021-03418-1. arXiv: 2002.12347 [hep-lat].

[98] Christoph Lehner et al. "Consistency of hadronic vacuum polarization between lattice QCD and the R-ratio". In: *Phys. Rev. D* 101 (2020), p. 074515. DOI: 10.1103/PhysRevD.101.074515. arXiv: 2003.04177 [hep-lat].

[99] Andreas Crivellin et al. "Hadronic Vacuum Polarization: $(g-2)_\mu$ versus Global Electroweak Fits". In: *Phys. Rev. Lett.* 125.9 (2020), p. 091801. DOI: 10.1103/PhysRevLett.125.091801. arXiv: 2003.04886 [hep-ph].

[100] Alexander Keshavarzi et al. "Muon $g-2$ and $\Delta\alpha$ connection". In: *Phys. Rev. D* 102.3 (2020), p. 033002. DOI: 10.1103/PhysRevD.102.033002. arXiv: 2006.12666 [hep-ph].

[101] Bogdan Malaescu et al. "Impact of correlations between a_μ and $\alpha_{\rm QED}$ on the EW fit". In: *Eur. Phys. J. C* 81.1 (2021), p. 46. DOI: 10.1140/epjc/s10052-021-08848-9. arXiv: 2008.08107 [hep-ph].

[102] Gilberto Colangelo et al. "Constraints on the two-pion contribution to hadronic vacuum polarization". In: *Phys. Lett. B* 814 (2021), p. 136073. DOI: 10.1016/j.physletb.2021.136073. arXiv: 2010.07943 [hep-ph].

[103] M. N. Achasov et al. "Measurement of the $e^+e^- \to \pi^+\pi^-$ process cross section with the SND detector at the VEPP-2000 collider in the energy region $0.525 < \sqrt{s} < 0.883$ GeV". In: *JHEP* 01 (2021), p. 113. DOI: 10.1007/JHEP01(2021)113. arXiv: 2004.00263 [hep-ex].

[104] Francisco Campanario et al. "Standard model radiative corrections in the pion form factor measurements do not explain the a_μ anomaly". In: *Phys. Rev. D* 100.7 (2019), p. 076004. DOI: 10.1103/PhysRevD.100.076004. arXiv: 1903.10197 [hep-ph].

[105] En-Hung Chao et al. "Hadronic light-by-light contribution to $(g-2)_\mu$ from lattice QCD: a complete calculation". In: *Eur. Phys. J. C* 81.7 (2021), p. 651. DOI: 10.1140/epjc/s10052-021-09455-4. arXiv: 2104.02632 [hep-lat].

[106] Martin Hoferichter et al. "Asymptotic behavior of meson transition form factors". In: *JHEP* 05 (2020), p. 159. DOI: 10.1007/JHEP05(2020)159. arXiv: 2004.06127 [hep-ph].

[107] Johan Bijnens et al. "Short-distance HLbL contributions to the muon anomalous magnetic moment beyond perturbation theory". In: *JHEP* 10 (2020), p. 203. DOI: 10.1007/JHEP10(2020)203. arXiv: 2008.13487 [hep-ph].

[108] Johan Bijnens et al. "The two-loop perturbative correction to the $(g-2)_\mu$ HLbL at short distances". In: *JHEP* 04 (2021), p. 240. DOI: 10.1007/JHEP04(2021)240. arXiv: 2101.09169 [hep-ph].

[109] Marvin Zanke et al. "On the transition form factors of the axial-vector resonance $f_1(1285)$ and its decay into e^+e^-". In: *JHEP* 07 (2021), p. 106. DOI: 10.1007/JHEP07(2021)106. arXiv: 2103.09829 [hep-ph].

[110] Igor Danilkin et al. "A dispersive estimate of scalar contributions to hadronic light-by-light scattering". In: *Phys. Lett. B* 820 (2021), p. 136502. DOI: 10.1016/j.physletb.2021.136502. arXiv: 2105.01666 [hep-ph].

[111] Gilberto Colangelo et al. "Short-distance constraints for the longitudinal component of the hadronic light-by-light amplitude: an update". In: *Eur. Phys. J. C* 81.8 (2021), p. 702. DOI: 10.1140/epjc/s10052-021-09513-x. arXiv: 2106.13222 [hep-ph].

[112] Bob Holdom. "Two U(1)'s and Epsilon Charge Shifts". In: *Phys. Lett. B* 166 (1986), pp. 196–198. DOI: 10.1016/0370-2693(86)91377-8.

[113] Maxim Pospelov. "Secluded U(1) below the weak scale". In: *Phys. Rev. D* 80 (2009), p. 095002. DOI: 10.1103/PhysRevD.80.095002. arXiv: 0811.1030 [hep-ph].

[114] Chien-Yi Chen et al. "Implications of a light "dark Higgs" solution to the g_μ-2 discrepancy". In: *Phys. Rev. D* 93.3 (2016), p. 035006. DOI: 10.1103/PhysRevD.93.035006. arXiv: 1511.04715 [hep-ph].

[115] Hooman Davoudiasl et al. "Tale of two anomalies". In: *Phys. Rev. D* 98.7 (2018), p. 075011. DOI: 10.1103/PhysRevD.98.075011. arXiv: 1806.10252 [hep-ph].

[116] L. Darmé et al. "Invisible decays of axion-like particles: constraints and prospects". In: *JHEP* 06 (2021), p. 009. DOI: 10.1007/JHEP06(2021)009. arXiv: 2012.07894 [hep-ph].

[117] M. Cadeddu et al. "Muon and electron g-2 and proton and cesium weak charges implications on dark Zd models". In: *Phys. Rev. D* 104.1 (2021), p. 011701. DOI: 10.1103/PhysRevD.104.L011701. arXiv: 2104.03280 [hep-ph].

[118] Manuel A. Buen-Abad et al. "Challenges for an axion explanation of the muon $g-2$ measurement". In: (Apr. 2021). arXiv: 2104.03267 [hep-ph].

[119] Luc Darmé et al. "Flavour anomalies and the muon $g-2$ from feebly interacting particles". In: (June 2021). arXiv: 2106.12582 [hep-ph].

[120] Andrzej Czarnecki et al. "The Muon anomalous magnetic moment: A Harbinger for 'new physics'". In: *Phys. Rev. D* 64 (2001), p. 013014. DOI: 10.1103/PhysRevD.64.013014. arXiv: hep-ph/0102122.

[121] Dominik Stöckinger. "Muon (g − 2) and Physics Beyond the Standard Model". In: *Adv. Ser. Direct. High Energy Phys.* 20 (2009), pp. 393–438. DOI: 10.1142/9789814271844_0012.

[122] Andreas Crivellin et al. "Combined explanations of $(g-2)_{\mu,e}$ and implications for a large muon EDM". In: *Phys. Rev. D* 98.11 (2018), p. 113002. DOI: 10.1103/PhysRevD.98.113002. arXiv: 1807.11484 [hep-ph].

[123] Rodolfo Capdevilla et al. "A No-Lose Theorem for Discovering the New Physics of $(g-2)_\mu$ at Muon Colliders". In: (Jan. 2021). arXiv: 2101.10334 [hep-ph].

[124] B. Ananthanarayan et al. "Top mass prediction from supersymmetric guts". In: *Phys. Rev. D* 44 (1991), pp. 1613–1615. DOI: 10.1103/PhysRevD.44.1613.

[125] Marcela Carena et al. "Electroweak symmetry breaking and bottom - top Yukawa unification". In: *Nucl. Phys. B* 426 (1994), pp. 269–300. DOI: 10.1016/0550-3213(94)90313-1. arXiv: hep-ph/9402253.

[126] Jorge L. Lopez et al. "Large $(g-2)_\mu$ in $SU(5) \times U(1)$ supergravity models". In: *Phys. Rev. D* 49 (1994), pp. 366–372. DOI: 10.1103/PhysRevD.49.366. arXiv: hep-ph/9308336.

[127] U. Chattopadhyay et al. "Probing supergravity grand unification in the Brookhaven g-2 experiment". In: *Phys. Rev. D* 53 (1996), pp. 1648–1657. DOI: 10.1103/PhysRevD.53.1648. arXiv: hep-ph/9507386.

[128] Athanasios Dedes et al. "Correlation of $B_s \to \mu^+\mu^-$ and $(g-2)_\mu$ in minimal supergravity". In: *Phys. Rev. Lett.* 87 (2001), p. 251804. DOI: 10.1103/PhysRevLett.87.251804. arXiv: hep-ph/0108037.

[129] A. Djouadi et al. "(eb), (et) type leptoquarks at $e\,p$ colliners". In: *Z. Phys. C* 46 (1990), pp. 679–686. DOI: 10.1007/BF01560270.

[130] Debrupa Chakraverty et al. "A Nonsupersymmetric resolution of the anomalous muon magnetic moment". In: *Phys. Lett. B* 506 (2001), pp. 103–108. DOI: 10.1016/S0370-2693(01)00419-1. arXiv: hep-ph/0102180.

[131] Kingman Cheung. "Muon anomalous magnetic moment and leptoquark solutions". In: *Phys. Rev. D* 64 (2001), p. 033001. DOI: 10.1103/PhysRevD.64.033001. arXiv: hep-ph/0102238.

[132] Martin Bauer et al. "Minimal Leptoquark Explanation for the $R_{D^{(*)}}$, R_K , and $(g-2)_\mu$ Anomalies". In: *Phys. Rev. Lett.* 116.14 (2016), p. 141802. DOI: 10.1103/PhysRevLett.116.141802. arXiv: 1511.01900 [hep-ph].

[133] Estefania Coluccio Leskow et al. "$(g-2)\mu$, lepton flavor violation, and Z decays with leptoquarks: Correlations and future prospects". In: *Phys. Rev. D* 95.5 (2017), p. 055018. DOI: 10.1103/PhysRevD.95.055018. arXiv: 1612.06858 [hep-ph].

[134] Andreas Crivellin et al. "Correlating $h \to \mu^+\mu^-$ to the Anomalous Magnetic Moment of the Muon via Leptoquarks". In: *Phys. Rev. Lett.* 127.2 (2021), p. 021801. DOI: 10.1103/PhysRevLett.127.021801. arXiv: 2008.02643 [hep-ph].

[135] Andreas Crivellin et al. "Scalar Leptoquarks in Leptonic Processes". In: *JHEP* 02 (2021), p. 182. DOI: 10.1007/JHEP02(2021)182. arXiv: 2010.06593 [hep-ph].

[136] Prasanta Das et al. "Anomalous magnetic moment of the muon in a composite model". In: (Feb. 2001). Ed. by J. Caparthy. arXiv: hep-ph/0102242.

[137] Zhao-Hua Xiong et al. "Muon anomalous magnetic moment in technicolor models". In: *Phys. Lett. B* 508 (2001), pp. 295–300. DOI: 10.1016/S0370-2693(01)00521-4. arXiv: hep-ph/0102259.

[138] Seong Chan Park et al. "Muon anomalous magnetic moment and the stabilized Randall-Sundrum scenario". In: *Phys. Lett. B* 506 (2001), pp. 99–102. DOI: 10.1016/S0370-2693(01)00417-8. arXiv: hep-ph/0103072.

[139] G. F. Giudice et al. "Testing new physics with the electron g-2". In: *JHEP* 11 (2012), p. 113. DOI: 10.1007/JHEP11(2012)113. arXiv: 1208.6583 [hep-ph].

[140] Radovan Dermisek et al. "Explanation of the Muon g-2 Anomaly with Vectorlike Leptons and its Implications for Higgs Decays". In: *Phys. Rev. D* 88 (2013), p. 013017. DOI: 10.1103/PhysRevD.88.013017. arXiv: 1305.3522 [hep-ph].

[141] Adam Falkowski et al. "Vector-like leptons: Higgs decays and collider phenomenology". In: *JHEP* 05 (2014), p. 092. DOI: 10.1007/JHEP05(2014)092. arXiv: 1312.5329 [hep-ph].

[142] Wolfgang Altmannshofer et al. "$L_\mu - L_\tau$ theory of Higgs flavor violation and $(g-2)_\mu$". In: *Phys. Rev. D* 94.9 (2016), p. 095026. DOI: 10.1103/PhysRevD.94.095026. arXiv: 1604.08221 [hep-ph].

[143] Kamila Kowalska et al. "Expectations for the muon g-2 in simplified models with dark matter". In: *JHEP* 09 (2017), p. 112. DOI: 10.1007/JHEP09(2017)112. arXiv: 1707.00753 [hep-ph].

[144] Pere Arnan et al. "Generic Loop Effects of New Scalars and Fermions in $b \to s\ell^+\ell^-$, $(g-2)_\mu$ and a Vector-like 4^{th} Generation". In: *JHEP* 06 (2019), p. 118. DOI: 10.1007/JHEP06(2019)118. arXiv: 1904.05890 [hep-ph].

[145] Andreas Crivellin et al. "Consequences of chirally enhanced explanations of $(g-2)_\mu$ for $h \to \mu\mu$ and $Z \to \mu\mu$". In: *JHEP* 07 (2021), p. 135. DOI: 10.1007/JHEP07(2021)135. arXiv: 2104.03202 [hep-ph].

[146] P. M. Ferreira et al. "$(g-2)_\mu$ in the 2HDM and slightly beyond – an updated view". In: (Apr. 2021). arXiv: 2104.03367 [hep-ph].

[147] Eung Jin Chun et al. "Explaining $g-2$ anomalies in two Higgs doublet model with vector-like leptons". In: *JHEP* 11 (2020), p. 077. DOI: 10.1007/JHEP11(2020)077. arXiv: 2009.08314 [hep-ph].

[148] Mariana Frank et al. "Muon anomalous magnetic moment in two-Higgs-doublet models with vectorlike leptons". In: *Phys. Rev. D* 102.11 (2020), p. 115034. DOI: 10.1103/PhysRevD.102.115034. arXiv: 2008.11909 [hep-ph].

[149] Junjie Cao et al. "Lepton-Specific Two-Higgs Doublet Model: Experimental Constraints and Implication on Higgs Phenomenology". In: *Phys. Rev. D* 80 (2009), p. 071701. DOI: 10.1103/PhysRevD.80.071701. arXiv: 0909.5148 [hep-ph].

[150] Alessandro Broggio et al. "Limiting two-Higgs-doublet models". In: *JHEP* 11 (2014), p. 058. DOI: 10.1007/JHEP11(2014)058. arXiv: 1409.3199 [hep-ph].

[151] Lei Wang et al. "A light pseudoscalar of 2HDM confronted with muon g-2 and experimental constraints". In: *JHEP* 05 (2015), p. 039. DOI: 10.1007/JHEP05(2015)039. arXiv: 1412.4874 [hep-ph].

[152] Victor Ilisie. "New Barr-Zee contributions to $(g-2)_\mu$ in two-Higgs-doublet models". In: *JHEP* 04 (2015), p. 077. DOI: 10.1007/JHEP04(2015)077. arXiv: 1502.04199 [hep-ph].

[153] Tomohiro Abe et al. "Lepton-specific two Higgs doublet model as a solution of muon $g-2$ anomaly". In: *JHEP* 07 (2015), p. 064. DOI: 10.1007/JHEP07(2015)064. arXiv: 1504.07059 [hep-ph].

[154] Andreas Crivellin et al. "A perturbed lepton-specific two-Higgs-doublet model facing experimental hints for physics beyond the Standard Model". In: *Phys. Rev. Lett.* 116.8 (2016), p. 081801. DOI: 10.1103/PhysRevLett.116.081801. arXiv: 1507.07567 [hep-ph].

[155] Andreas Crivellin et al. "$b \to s\ell^+\ell^-$ transitions in two-Higgs-doublet models". In: *JHEP* 06 (2019), p. 119. DOI: 10.1007/JHEP06(2019)119. arXiv: 1903.10440 [hep-ph].

[156] Syuhei Iguro et al. "Probing $\mu\tau$ flavor-violating solutions for the muon $g-2$ anomaly at Belle II". In: *JHEP* 09 (2020), p. 144. DOI: 10.1007/JHEP09(2020)144. arXiv: 2002.12728 [hep-ph].

[157] Hong-Xin Wang et al. "muon $g-2$ anomaly and μ-τ-philic Higgs doublet with a light CP-even component". In: (Apr. 2021). arXiv: 2104.03242 [hep-ph].

[158] Wei-Shu Hou et al. "Charged lepton flavor violation in light of Muon $g-2$". In: (July 2021). arXiv: 2107.14114 [hep-ph].

[159] Timothy Chupp et al. "Electric dipole moments of atoms, molecules, nuclei, and particles". In: *Rev. Mod. Phys.* 91.1 (2019), p. 015001. DOI: 10.1103/RevModPhys.91.015001. arXiv: 1710.02504 [physics.atom-ph].

[160] G. W. Bennett et al. "An Improved Limit on the Muon Electric Dipole Moment". In: *Phys. Rev. D* 80 (2009), p. 052008. DOI: 10.1103/PhysRevD.80.052008. arXiv: 0811.1207 [hep-ex].

[161] V. Andreev et al. "Improved limit on the electric dipole moment of the electron". In: *Nature* 562.7727 (2018), pp. 355–360. DOI: 10.1038/s41586-018-0599-8.

[162] R.Sekhar Chivukula et al. "A Composite Technicolor Standard Model of Quarks". In: *Nucl. Phys. B* 292 (1987), pp. 93–108. DOI: 10.1016/0550-3213(87)90638-9.

[163] L.J. Hall et al. "Weak scale effective supersymmetry". In: *Phys. Rev. Lett.* 65 (1990), pp. 2939–2942. DOI: 10.1103/PhysRevLett.65.2939.

[164] A.J. Buras et al. "Universal unitarity triangle and physics beyond the standard model". In: *Phys. Lett. B* 500 (2001), pp. 161–167. DOI: 10.1016/S0370-2693(01)00061-2. arXiv: hep-ph/0007085.

[165] G. D'Ambrosio et al. "Minimal flavor violation: An Effective field theory approach". In: *Nucl. Phys. B* 645 (2002), pp. 155–187. DOI: 10.1016/S0550-3213(02)00836-2. arXiv: hep-ph/0207036.

[166] Joel Nathan Butler. "Highlights and Perspectives from the CMS Experiment". In: *5th Large Hadron Collider Physics Conference*. Sept. 2017. arXiv: 1709.03006 [hep-ex].

[167] Lucia Masetti. "ATLAS results and prospects with focus on beyond the Standard Model". In: *Nucl. Part. Phys. Proc.* 303-305 (2018). Ed. by Giulia Ricciardi et al., pp. 43–48. DOI: 10.1016/j.nuclphysbps.2019.03.009.

[168] R. Aaij et al. "Differential branching fractions and isospin asymmetries of $B \to K^{(*)}\mu^+\mu^-$ decays". In: *JHEP* 06 (2014), p. 133. DOI: 10.1007/JHEP06(2014)133. arXiv: 1403.8044 [hep-ex].

[169] Roel Aaij et al. "Test of lepton universality using $B^+ \to K^+\ell^+\ell^-$ decays". In: *Phys. Rev. Lett.* 113 (2014), p. 151601. DOI: 10.1103/PhysRevLett.113.151601. arXiv: 1406.6482 [hep-ex].

[170] Roel Aaij et al. "Angular analysis and differential branching fraction of the decay $B_s^0 \to \phi\mu^+\mu^-$". In: *JHEP* 09 (2015), p. 179. DOI: 10.1007/JHEP09(2015)179. arXiv: 1506.08777 [hep-ex].

[171] Roel Aaij et al. "Angular analysis of the $B^0 \to K^{*0}\mu^+\mu^-$ decay using 3 fb^{-1} of integrated luminosity". In: *JHEP* 02 (2016), p. 104. DOI: 10.1007/JHEP02(2016)104. arXiv: 1512.04442 [hep-ex].

[172] Vardan Khachatryan et al. "Angular analysis of the decay $B^0 \to K^{*0}\mu^+\mu^-$ from pp collisions at $\sqrt{s} = 8$ TeV". In: *Phys. Lett. B* 753 (2016), pp. 424–448. DOI: 10.1016/j.physletb.2015.12.020. arXiv: 1507.08126 [hep-ex].

[173] Ina Carli. "Angular analysis of $B_d^0 \to K^*\mu^+\mu^-$ decay with the ATLAS detector". In: *PoS* FPCP2017 (2017), p. 043. DOI: 10.22323/1.304.0043.

[174] Albert M Sirunyan et al. "Measurement of angular parameters from the decay $\mathrm{B}^0 \to \mathrm{K}^{*0}\mu^+\mu^-$ in proton-proton collisions at $\sqrt{s} = 8$ TeV". In: *Phys. Lett. B* 781 (2018), pp. 517–541. DOI: 10.1016/j.physletb.2018.04.030. arXiv: 1710.02846 [hep-ex].

[175] R. Aaij et al. "Test of lepton universality with $B^0 \to K^{*0}\ell^+\ell^-$ decays". In: *JHEP* 08 (2017), p. 055. DOI: 10.1007/JHEP08(2017)055. arXiv: 1705.05802 [hep-ex].

[176] "Combination of the ATLAS, CMS and LHCb results on the $B_{(s)}^0 \to \mu^+\mu^-$ decays". In: (Aug. 2020).

[177] Roel Aaij et al. "Branching fraction measurements of the rare $B_s^0 \to \phi\mu^+\mu^-$ and $B_s^0 \to f_2'(1525)\mu^+\mu^-$ decays". In: (May 2021). arXiv: 2105.14007 [hep-ex].

[178] Marcel Algueró et al. "$b \to s\ell\ell$ global fits after Moriond 2021 results". In: *55th Rencontres de Moriond on QCD and High Energy Interactions*. Apr. 2021. arXiv: 2104.08921 [hep-ph].

[179] Wolfgang Altmannshofer et al. “New Physics in Rare B Decays after Moriond 2021”. In: (Mar. 2021). arXiv: 2103.13370 [hep-ph].

[180] Ashutosh Kumar Alok et al. “A unique discrimination between new physics scenarios in $b \to s\mu^+\mu^-$ anomalies”. In: (Jan. 2020). arXiv: 2001.04395 [hep-ph].

[181] T. Hurth et al. “Model independent analysis of the angular observables in $B^0 \to K^{*0}\mu^+\mu^-$ and $B^+ \to K^{*+}\mu^+\mu^-$”. In: *Phys. Rev. D* 103 (2021), p. 095020. DOI: 10.1103/PhysRevD.103.095020. arXiv: 2012.12207 [hep-ph].

[182] Marco Ciuchini et al. “Lessons from the $B^{0,+} \to K^{*0,+}\mu^+\mu^-$ angular analyses”. In: *Phys. Rev. D* 103.1 (2021), p. 015030. DOI: 10.1103/PhysRevD.103.015030. arXiv: 2011.01212 [hep-ph].

[183] Vincenzo Cirigliano et al. “Minimal flavor violation in the lepton sector”. In: *Nucl. Phys. B* 728 (2005), pp. 121–134. DOI: 10.1016/j.nuclphysb.2005.08.037. arXiv: hep-ph/0507001.

[184] X. G. He et al. “New Z-prime Phenomenology”. In: *Phys. Rev. D* 43 (1991), pp. 22–24. DOI: 10.1103/PhysRevD.43.R22.

[185] Robert Foot. “New Physics From Electric Charge Quantization?” In: *Mod. Phys. Lett. A* 6 (1991), pp. 527–530. DOI: 10.1142/S0217732391000543.

[186] Xiao-Gang He et al. “Simplest Z-prime model”. In: *Phys. Rev. D* 44 (1991), pp. 2118–2132. DOI: 10.1103/PhysRevD.44.2118.

[187] Giovanni Marco Pruna. “Leptonic CP violation in the charged sector and effective field theory approach”. In: *PoS* FPCP2017 (2017), p. 016. DOI: 10.22323/1.304.0016. arXiv: 1710.08311 [hep-ph].

[188] Andreas Crivellin et al. “Combined Explanations of $(g-2)_\mu$, $(g-2)_e$ and Implications for a Large Muon EDM$*$”. In: *PoS* ALPS2019 (2020), p. 009. DOI: 10.22323/1.360.0009. arXiv: 1905.03789 [hep-ph].

[189] Rebecca Chislett. “The muon EDM in the g-2 experiment at Fermilab”. In: *EPJ Web Conf.* 118 (2016). Ed. by G. D’Ambrosio et al., p. 01005. DOI: 10.1051/epjconf/201611801005.

[190] F. J. M. Farley et al. “A New method of measuring electric dipole moments in storage rings”. In: *Phys. Rev. Lett.* 93 (2004), p. 052001. DOI: 10.1103/PhysRevLett.93.052001. arXiv: hep-ex/0307006.

[191] A. Adelmann et al. “Compact storage ring to search for the muon electric dipole moment”. In: *J. Phys. G* 37 (2010), p. 085001. DOI: 10.1088/0954-3899/37/8/085001.

[192] Hiromi Iinuma et al. “Three-dimensional spiral injection scheme for the g-2/EDM experiment at J-PARC”. In: *Nucl. Instrum. Meth. A* 832 (2016), pp. 51–62. DOI: 10.1016/j.nima.2016.05.126.

[193] A. Adelmann et al. “Search for a muon EDM using the frozen-spin technique”. In: (Feb. 2021). arXiv: 2102.08838 [hep-ex].

[194] GA Beer et al. “Enhancement of muonium emission rate from silica aerogel with a laser-ablated surface”. In: *Progress of Theoretical and Experimental Physics* 2014.9 (2014). DOI: 10.1093/ptep/ptu116.

[195] A. Antognini et al. “Muonium emission into vacuum from mesoporous thin films at cryogenic temperatures”. In: *Phys. Rev. Lett.* 108 (2012), p. 143401. DOI: 10.1103/PhysRevLett.108.143401. arXiv: 1112.4887 [physics.atom-ph].

[196] K. S. Khaw et al. “Spatial confinement of muonium atoms”. In: *Phys. Rev. A* 94.2 (2016), p. 022716. DOI: 10.1103/PhysRevA.94.022716. arXiv: 1606.05840 [physics.atom-ph].

[197] Kim S. Khaw. “Towards next generation fundamental precision measurements with muons”. PhD thesis. ETH Zürich Research Collection, 2015. URL: https://www.research-collection.ethz.ch/handle/20.500.11850/102926.

[198] D Taqqu. “Ultraslow Muonium for a Muon beam of ultra high quality”. In: *Physics Procedia* 17 (2011), pp. 216–223. DOI: 10.1016/j.phpro.2011.06.039.

[199] Klaus Kirch et al. “Testing antimatter gravity with muonium”. In: *International Journal of Modern Physics: Conference Series*. Vol. 30. World Scientific. 2014, p. 1460258. DOI: 10.1142/S2010194514602580.

[200] Anna Soter et al. “Development of a cold atomic muonium beam for next generation atomic physics and gravity experiments”. In: *SciPost Phys. Proc.* (5 2021), p. 31. DOI: 10.21468/SciPostPhysProc.5.031.

[201] M Saarela et al. “Hydrogen isotope and ^{3}He impurities in liquid ^{4}He”. In: *Journal of Low Temperature Physics* 90.5 (1993), pp. 415–449. DOI: 10.1007/BF00681890.

[202] JM Marin et al. “Atomic and Molecular Hydrogen Impurities in Liquid 4 He”. In: *Journal of Low Temperature Physics* 110.1 (1998), pp. 205–211. DOI: 10.1023/A:1022599725388.

[203] Savely G. Karshenboim. “Precision physics of simple atoms: QED tests, nuclear structure and fundamental constants”. In: *Phys. Rept.* 422 (2005), pp. 1–63. DOI: 10.1016/j.physrep.2005.08.008. arXiv: hep-ph/0509010.

[204] Claudia Frugiuele et al. “Current and future perspectives of positronium and muonium spectroscopy as dark sectors probe”. In: *Phys. Rev. D* 100.1 (2019), p. 015010. DOI: 10.1103/PhysRevD.100.015010. arXiv: 1902.08585 [hep-ph].

[205] André H. Gomes et al. “Laboratory tests of Lorentz and CPT symmetry with muons”. In: *Phys. Rev. D* 90 (7 Oct. 2014), p. 076009. DOI: 10.1103/PhysRevD.90.076009.

[206] Savely G. Karshenboim. “A Constraint on antigravity of antimatter from precision spectroscopy of simple atoms”. In: *Astron. Lett.* 35 (2009), p. 663. DOI: 10.1134/S1063773709100028. arXiv: 0811.1008 [gr-qc].

[207] Klaus P. Jungmann. “Precision Muonium Spectroscopy”. In: *Journal of the Physical Society of Japan* 85.9 (2016), p. 091004. DOI: 10.7566/JPSJ.85.091004.

[208] T. Prokscha et al. “The new muE4 beam at PSI: A hybrid-type large acceptance channel for the generation of a high intensity surface-muon beam”. In: *Nucl. Instrum. Meth. A* 595 (2008), pp. 317–331. DOI: 10.1016/j.nima.2008.07.081.

[209] P. Crivelli. “The Mu-MASS (MuoniuM lAser SpectroScopy) experiment”. In: *Hyperfine Interact.* 239.1 (2018), p. 49. DOI: 10.1007/s10751-018-1525-z. arXiv: 1811.00310 [physics.atom-ph].

[210] B. Ohayon et al. “Precision measurement of the Lamb shift in Muonium”. In: (Aug. 2021). arXiv: 2108.12891 [physics.atom-ph].

[211] Ben Ohayon et al. “Current status and prospects of muonium spectroscopy at PSI”. In: *SciPost Phys. Proc.* 5 (2021), p. 029. DOI: 10.21468/SciPostPhysProc.5.029.

[212] S. Kanda et al. “New precise spectroscopy of the hyperfine structure in muonium with a high-intensity pulsed muon beam”. In: (2020). arXiv: 2004.05862 [hep-ex].

[213] Michael I. Eides. “Hyperfine Splitting in Muonium: Accuracy of the Theoretical Prediction”. In: *Phys. Lett. B* 795 (2019), pp. 113–116. DOI: 10.1016/j.physletb.2019.06.011. arXiv: 1812.10881 [hep-ph].

[214] Cédric Delaunay et al. “Towards an independent determination of muon g-2 from muonium spectroscopy”. In: (June 2021). arXiv: 2106.11998 [hep-ph].

[215] Pavel Fadeev et al. “Revisiting spin-dependent forces mediated by new bosons: Potentials in the coordinate-space representation for macroscopic- and atomic-scale experiments”. In: *Phys. Rev. A* 99.2 (2019), p. 022113. DOI: 10.1103/PhysRevA.99.022113. arXiv: 1810.10364 [hep-ph].

[216] Yu. M. Andreev et al. “Constraints on New Physics in Electron $g-2$ from a Search for Invisible Decays of a Scalar, Pseudoscalar, Vector, and Axial Vector”. In: *Phys. Rev. Lett.* 126.21 (2021), p. 211802. DOI: 10.1103/PhysRevLett.126.211802. arXiv: 2102.01885 [hep-ex].

[217] V. Meyer et al. “Measurement of the $1s-2s$ Energy Interval in Muonium”. In: *Phys. Rev. Lett.* 84 (6 Feb. 2000), pp. 1136–1139. DOI: 10.1103/PhysRevLett.84.1136.

[218] Joseph W Goodman. *Statistical optics*. John Wiley & Sons, 2015.

[219] Markus K Oberthaler et al. “Inertial sensing with classical atomic beams”. In: *Physical Review A* 54.4 (1996), p. 3165. DOI: 10.1103/PhysRevA.54.3165.

[220] Ben McMorran et al. “Model for partial coherence and wavefront curvature in grating interferometers”. In: *Physical Review A* 78.1 (2008), p. 013601. DOI: 10.1103/PhysRevA.78.013601.

[221] D. M. Webber et al. “Measurement of the Positive Muon Lifetime and Determination of the Fermi Constant to Part-per-Million Precision”. In: *Phys. Rev. Lett.* 106 (2011), p. 041803. DOI: 10.1103/PhysRevLett.106.079901. arXiv: 1010.0991 [hep-ex].

[222] W. Fetscher et al. “Muon Decay: Complete Determination of the Interaction and Comparison with the Standard Model”. In: *Phys. Lett. B* 173 (1986), pp. 102–106. DOI: 10.1016/0370-2693(86)91239-6.

[223] N. Danneberg et al. “Muon decay: Measurement of the transverse polarization of the decay positrons and its implications for the Fermi coupling constant and time reversal invariance”. In: *Phys. Rev. Lett.* 94 (2005), p. 021802. DOI: 10.1103/PhysRevLett.94.021802.

[224] Wulf Fetscher. “Muon Decay”. In: *SciPost Phys. Proc.* 5 (2021), p. 006. DOI: 10.21468/SciPostPhysProc.5.006.

[225] A. Jodidio et al. “Search for Right-Handed Currents in Muon Decay”. In: *Phys. Rev. D* 34 (1986). [Erratum: Phys.Rev.D 37, 237 (1988)], p. 1967. DOI: 10.1103/PhysRevD.34.1967.

[226] A. Hillairet et al. “Precision muon decay measurements and improved constraints on the weak interaction”. In: *Phys. Rev. D* 85 (2012), p. 092013. DOI: 10.1103/PhysRevD.85.092013. arXiv: 1112.3606 [hep-ex].

[227] R. Bayes et al. “Experimental Constraints on Left-Right Symmetric Models from Muon Decay”. In: *Phys. Rev. Lett.* 106 (2011), p. 041804. DOI: 10.1103/PhysRevLett.106.041804.

[228] J. F. Bueno et al. “Precise measurement of parity violation in polarized muon decay”. In: *Phys. Rev. D* 84 (2011), p. 032005. DOI: 10.1103/PhysRevD.84.032005. arXiv: 1104.3632 [hep-ex].

[229] D. V. Forero et al. “Lepton flavor violation and non-unitary lepton mixing in low-scale type-I seesaw”. In: *JHEP* 09 (2011), p. 142. DOI: 10.1007/JHEP09(2011)142. arXiv: 1107.6009 [hep-ph].

[230] R. Alonso et al. “Muon conversion to electron in nuclei in type-I seesaw models”. In: *JHEP* 01 (2013), p. 118. DOI: 10.1007/JHEP01(2013)118. arXiv: 1209.2679 [hep-ph].

[231] André de Gouvêa et al. “Global Constraints on a Heavy Neutrino”. In: *Phys. Rev. D* 93.3 (2016), p. 033005. DOI: 10.1103/PhysRevD.93.033005. arXiv: 1511.00683 [hep-ph].

[232] J. Beacham et al. “Physics Beyond Colliders at CERN: Beyond the Standard Model Working Group Report”. In: *J. Phys. G* 47.1 (2020), p. 010501. DOI: 10.1088/1361-6471/ab4cd2. arXiv: 1901.09966 [hep-ex].

[233] A. J. Krasznahorkay et al. “Observation of Anomalous Internal Pair Creation in Be8 : A Possible Indication of a Light, Neutral Boson”. In: *Phys. Rev. Lett.* 116.4 (2016), p. 042501. DOI: 10.1103/PhysRevLett.116.042501. arXiv: 1504.01527 [nucl-ex].

[234] Prateek Agrawal et al. “Feebly-Interacting Particles:FIPs 2020 Workshop Report”. In: (Feb. 2021). arXiv: 2102.12143 [hep-ph].

[235] Martin Bauer et al. “Flavor probes of axion-like particles”. In: (Oct. 2021). arXiv: 2110.10698 [hep-ph].

[236] R. Bayes et al. “Search for two body muon decay signals”. In: *Phys. Rev. D* 91.5 (2015), p. 052020. DOI: 10.1103/PhysRevD.91.052020. arXiv: 1409.0638 [hep-ex].

[237] Apostolos Pilaftsis. “Astrophysical and terrestrial constraints on singlet Majoron models”. In: *Phys. Rev. D* 49 (1994), pp. 2398–2404. DOI: 10.1103/PhysRevD.49.2398. arXiv: hep-ph/9308258.

[238] M. Hirsch et al. “Majoron emission in muon and tau decays revisited”. In: *Phys. Rev. D* 79 (2009). [Erratum: Phys.Rev.D 79, 079901 (2009)], p. 055023. DOI: 10.1103/PhysRevD.79.055023. arXiv: 0902.0525 [hep-ph].

[239] Lorenzo Calibbi et al. “Looking forward to Lepton-flavor-violating ALPs”. In: (June 2020). arXiv: 2006.04795 [hep-ph].

[240] Xavier Garcia i Tormo et al. “Bounds on majoron emission from muon to electron conversion experiments”. In: *Phys. Rev. D* 84 (2011), p. 113010. DOI: 10.1103/PhysRevD.84.113010. arXiv: 1110.2874 [hep-ph].

[241] J. Terrance Goldman et al. “Light Boson Emission in the Decay of the μ^+”. In: *Phys. Rev. D* 36 (1987), pp. 1543–1546. DOI: 10.1103/PhysRevD.36.1543.

[242] R. D. Bolton et al. “Search for Rare Muon Decays with the Crystal Box Detector”. In: *Phys. Rev. D* 38 (1988), p. 2077. DOI: 10.1103/PhysRevD.38.2077.

[243] A.M. Baldini et al. “Search for lepton flavour violating muon decay mediated by a new light particle in the MEG experiment”. In: *Eur. Phys. J. C* 80.9 (2020), p. 858. DOI: 10.1140/epjc/s10052-020-8364-1. arXiv: 2005.00339 [hep-ex].

[244] Christina D. Kreisch et al. “Neutrino puzzle: Anomalies, interactions, and cosmological tensions”. In: *Phys. Rev. D* 101.12 (2020), p. 123505. DOI: 10.1103/PhysRevD.101.123505. arXiv: 1902.00534 [astro-ph.CO].

[245] Jose Luis Bernal et al. “The trouble with H_0”. In: *JCAP* 10 (2016), p. 019. DOI: 10.1088/1475-7516/2016/10/019. arXiv: 1607.05617 [astro-ph.CO].

[246] N. Aghanim et al. “Planck 2018 results. VI. Cosmological parameters”. In: *Astron. Astrophys.* 641 (2020). [Erratum: Astron.Astrophys. 652, C4 (2021)], A6. DOI: 10.1051/0004-6361/201833910. arXiv: 1807.06209 [astro-ph.CO].

[247] Kun-Feng Lyu et al. “Self-interacting neutrinos: Solution to Hubble tension versus experimental constraints”. In: *Phys. Rev. D* 103.1 (2021), p. 015004. DOI: 10.1103/PhysRevD.103.015004. arXiv: 2004.10868 [hep-ph].

[248] A. P. Lessa et al. “Revising limits on neutrino-Majoron couplings”. In: *Phys. Rev. D* 75 (2007), p. 094001. DOI: 10.1103/PhysRevD.75.094001. arXiv: hep-ph/0701068.

[249] Pulak Banerjee et al. “QED at NNLO with McMule”. In: *SciPost Phys.* 9 (2020), p. 027. DOI: 10.21468/SciPostPhys.9.2.027. arXiv: 2007.01654 [hep-ph].

[250] B. Pontecorvo. "Mesonium and anti-mesonium". In: *Sov. Phys. JETP* 6 (1957), p. 429.

[251] V.W. Hughes et al. "Formation of Muonium and Observation of its Larmor Precession". In: *Phys. Rev. Lett.* 5 (1960), pp. 63–65.

[252] J.J. Amato et al. "Search for muonium-antimuonium conversion". In: *Phys. Rev. Lett.* 21 (1968), pp. 1709–1712.

[253] Glen M. Marshall et al. "A Search for Muonium to Anti-muonium Conversion". In: *Phys. Rev. D* 25 (1982), p. 1174.

[254] T.M. Huber et al. "Search for Mixing of Muonium (μ^+e^-) and Anti-muonium (μ^-e^+)". In: *Phys. Rev. D* 41 (1990), pp. 2709–2725.

[255] P.R. Bolton et al. "Observation of Muonium in Vacuum". In: *Phys. Rev. Lett.* 47 (1981), pp. 1441–1444. DOI: 10.1103/PhysRevLett.47.1441.

[256] B. Ni et al. "Search for Spontaneous Conversion of Muonium to Antimuonium". In: *Phys. Rev. Lett.* 59.24 (1987), pp. 2716–2719.

[257] B. Ni et al. "Search for spontaneous conversion of muonium to anti-muonium". In: *Phys. Rev. D* 48 (1993), pp. 1976–1989.

[258] B.E. Matthias et al. "New search for the spontaneous conversion of muonium to anti-muonium". In: *Phys. Rev. Lett.* 66 (1991), pp. 2716–2719.

[259] R. Abela et al. "Improved upper limit on muonium to anti-muonium conversion". In: *Phys. Rev. Lett.* 77 (1996), pp. 1950–1953. arXiv: nucl-ex/9805005.

[260] L. Willmann et al. "New bounds from searching for muonium to anti-muonium conversion". In: *Phys. Rev. Lett.* 82 (1999), pp. 49–52. arXiv: hep-ex/9807011.

[261] S. Agostinelli et al. "GEANT4–a simulation toolkit". In: *Nucl. Instrum. Meth. A* 506 (2003), pp. 250–303. DOI: 10.1016/S0168-9002(03)01368-8.

[262] A. Antognini et al. "Proton Structure from the Measurement of $2S-2P$ Transition Frequencies of Muonic Hydrogen". In: *Science* 339 (2013), pp. 417–420. DOI: 10.1126/science.1230016.

[263] Randolf Pohl et al. "Laser spectroscopy of muonic deuterium". In: *Science* 353.6300 (2016), pp. 669–673. DOI: 10.1126/science.aaf2468.

[264] Julian J. Krauth et al. "Measuring the α-particle charge radius with muonic helium-4 ions". In: *Nature* 589.7843 (2021), pp. 527–531. DOI: 10.1038/s41586-021-03183-1.

[265] Frederik Wauters et al. "The *muX* project". In: (Aug. 2021). arXiv: 2108.10765 [physics.ins-det].

[266] John H. Missimer et al. "The Neutral Weak Current of the Muon". In: *Phys. Rept.* 118 (1985), p. 179.

[267] K. Kirch et al. "Metastability of the Muonic Boron $2S$ State". In: *Phys. Rev. Lett.* 78 (23 1997), pp. 4363–4366. DOI: 10.1103/PhysRevLett.78.4363.

[268] Savely G. Karshenboim et al. "Constraints on muon-specific dark forces". In: *Phys. Rev. D* 90.7 (2014). [Addendum: Phys.Rev.D 90, 079905 (2014)], p. 073004. DOI: 10.1103/PhysRevD.90.073004. arXiv: 1401.6154 [hep-ph].

[269] Andreas Crivellin et al. "First-generation new physics in simplified models: from low-energy parity violation to the LHC". In: *JHEP* 10 (2021), p. 221. DOI: 10.1007/JHEP10(2021)221. arXiv: 2107.13569 [hep-ph].

[270] E.G. Kessler et al. "The GAMS4 flat crystal facility". In: *Nuclear Instruments and Methods in Physics Research Section A: Accelerators, Spectrometers, Detectors and Associated Equipment* 457.1 (2001), pp. 187–202. ISSN: 0168-9002. DOI: https://doi.org/10.1016/S0168-9002(00)00753-1.

[271] Saskia Kraft-Bermuth et al. "Microcalorimeters for X-Ray Spectroscopy of Highly Charged Ions at Storage Rings". In: *Atoms* 6.4 (2018), p. 59. DOI: 10.3390/atoms6040059.

[272] R. Winkler et al. "256-pixel microcalorimeter array for high-resolution γ-ray spectroscopy of mixed-actinide materials". In: *Nuclear Instruments and Methods in Physics Research Section A: Accelerators, Spectrometers, Detectors and Associated Equipment* 770 (2015), pp. 203–210. ISSN: 0168-9002. DOI: https://doi.org/10.1016/j.nima.2014.09.049.

[273] Nancy Paul et al. "Testing Quantum Electrodynamics with Exotic Atoms". In: *Phys. Rev. Lett.* 126.17 (2021), p. 173001. DOI: 10.1103/PhysRevLett.126.173001. arXiv: 2011.09715 [physics.atom-ph].

[274] Ryuichiro Kitano et al. "Detailed calculation of lepton flavor violating muon electron conversion rate for various nuclei". In: *Phys. Rev. D* 66 (2002). [Erratum: Phys.Rev.D 76, 059902 (2007)], p. 096002. DOI: 10.1103/PhysRevD.76.059902. arXiv: hep-ph/0203110.

[275] A. Yaouanc et al. *Muon Spin Rotation, Relaxation, and Resonance: Applications to Condensed Matter*. Oxford, UK: Oxford University Press, 2011.

[276] Donald G. Fleming et al. "Kinetic Isotope Effects for the Reactions of Muonic Helium and Muonium with H_2". In: *Science* 331.6016 (2011), pp. 448–450. DOI: 10.1126/science.1199421.

[277] F. Berg et al. "Target Studies for Surface Muon Production". In: *Phys. Rev. Accel. Beams* 19.2 (2016), p. 024701. DOI: 10.1103/PhysRevAccelBeams.19.024701. arXiv: 1511.01288 [physics.ins-det].

[278] Oren Shafir et al. "Demonstrating multibit magnetic memory in the Fe_8 high-spin molecule by muon spin rotation". In: *Phys. Rev. B* 72 (2005), p. 092410. DOI: 10.1103/PhysRevB.72.092410.

[279] Lorenzo Tesi et al. "Isotope effects on the spin dynamics of single-molecule magnets probed using muon spin spectroscopy". In: *Chem. Commun.* 54 (2018), pp. 7826–7829. DOI: 10.1039/C8CC04703K.

[280] Evan Kiefl et al. “Robust Magnetic Properties of a Sublimable Single-Molecule Magnet”. In: *ACS Nano* 10 (2016), pp. 5663–5669. DOI: 10.1021/acsnano.6b01817.

[281] Ola Kenji Forslund et al. “Magnetic phase diagram of $K_2Cr_8O_{16}$ clarified by high-pressure muon spin spectroscopy”. In: *Scientific Reports* 9 (2019), p. 1141. DOI: 10.1038/s41598-018-37844-5.

[282] Tom Lancaster et al. “Another dimension: investigations of molecular magnetism using muon–spin relaxation”. In: *Physica Scripta* 88.6 (2013), p. 068506. DOI: 10.1088/0031-8949/88/06/068506.

[283] Katherine Tustain et al. “From magnetic order to quantum disorder in the Zn-barlowite series of S = 1/2 kagomé antiferromagnets”. In: *npj Quantum Materials* 5 (2020), p. 74. DOI: 10.1038/s41535-020-00276-4.

[284] Bin Gao et al. “Experimental signatures of a three-dimensional quantum spin liquid in effective spin-1/2 $Ce_2Zr_2O_7$ pyrochlore”. In: *Nature Physics* 15 (2019), pp. 1052–1057. DOI: 10.1038/s41567-019-0577-6.

[285] Francis Pratt. “Superconductivity and Magnetism in Organic Materials Studied with μSR”. In: *Journal of the Physical Society of Japan* 85 (2016), p. 091008. DOI: 10.7566/JPSJ.85.091008.

[286] Ke Wang et al. “Spintronic and Electronic Phenomena in Organic Molecules Measured with μSR”. In: *Journal of the Physical Society of Japan* 85 (2016), p. 091011. DOI: 10.7566/JPSJ.85.091011.

[287] F L Pratt. “Muon spin relaxation as a probe of electron motion in conducting polymers”. In: *Journal of Physics: Condensed Matter* 16 (2004), S4779–S4796. DOI: 10.1088/0953-8984/16/40/019.

[288] Iain McKenzie et al. “Muoniated spin probes in the discotic liquid crystal HHTT: Rapid electron spin relaxation in the hexagonal columnar and isotropic phases”. In: *Phys. Rev. E* 87 (2013), p. 012504. DOI: 10.1103/PhysRevE.87.012504.

[289] Z. Guguchia et al. “Tunable anomalous Hall conductivity through volume-wise magnetic competition in a topological kagomé magnet”. In: *Nature Communications* 11 (2020), p. 559. DOI: 0.1038/s41467-020-14325-w.

[290] Zurab Guguchia et al. “Nodeless superconductivity and its evolution with pressure in the layered dirac semimetal 2M-WS_2”. In: *npj Quantum Materials* 4 (2019), p. 50. DOI: 10.1038/s41535-019-0189-5.

[291] Jonas A. Krieger et al. “Proximity-Induced Odd-Frequency Superconductivity in a Topological Insulator”. In: *Phys. Rev. Lett.* 125 (2020), p. 026802. DOI: 10.1103/PhysRevLett.125.026802.

[292] J. A. Krieger et al. “Do topology and ferromagnetism cooperate at the EuS/Bi_2Se_3 interface?” In: *Phys. Rev. B* 99 (6 2019), p. 064423. DOI: 10.1103/PhysRevB.99.064423.

[293] H. V. Alberto et al. "Slow-muon study of quaternary solar-cell materials: Single layers and $p-n$ junctions". In: *Phys. Rev. Materials* 2 (2018), p. 025402. DOI: 10.1103/PhysRevMaterials.2.025402.

[294] M.A. Curado et al. "Front passivation of Cu(In,Ga)Se2 solar cells using Al2O3: Culprits and benefits". In: *Applied Materials Today* 21 (2020), p. 100867. DOI: 10.1016/j.apmt.2020.100867.

[295] Judith Woerle et al. "Interaction of low-energy muons with defect profiles in proton-irradiated Si and 4H-SiC". In: *Phys. Rev. B* 100 (2019), p. 115202. DOI: 10.1103/PhysRevB.100.115202.

[296] J. Woerle et al. "Muon Interaction with Negative-U and High-Spin-State Defects: Differentiating Between C and Si Vacancies in 4H-SiC". In: *Phys. Rev. Applied* 14 (2020), p. 054053. DOI: 10.1103/PhysRevApplied.14.054053.

[297] T. Prokscha et al. "Direct Observation of Hole Carrier-Density Profiles and Their Light-Induced Manipulation at the Surface of Ge". In: *Phys. Rev. Applied* 14 (2020), p. 014098. DOI: 10.1103/PhysRevApplied.14.014098.

[298] R. Abela et al. "Muons on request (MORE): Combining advantages of continuous and pulsed muon beams". In: *Hyperfine Interactions* 120-121.1-8 (1999), pp. 575–578. ISSN: 03043843. DOI: 10.1023/A:1017046817431.

[299] A. E. Pifer et al. "A High Stopping Density μ^+ Beam". In: *Nucl. Instrum. Meth.* 135 (1976), pp. 39–46. DOI: 10.1016/0029-554X(76)90823-5.

[300] T. Prokscha et al. "Depth dependence of the ionization energy of shallow hydrogen states in ZnO and CdS". In: *Physical Review B* 90 (2014), p. 235303. DOI: 10.1103/PhysRevB.90.235303.

[301] P. Bakule et al. "Generation and applications of slow polarized muons". In: *Contemp. Phys.* 45 (2004), p. 203. DOI: 10.1080/00107510410001676803.

[302] E. Morenzoni et al. "Nano-scale thin film investigations with slow polarized muons". In: *J. Phys.: Cond. Matt.* 16 (2004), S4583. DOI: 10.1088/0953-8984/16/40/010.

[303] Judith Woerle et al. *Low-Energy Muons as a Tool for a Depth-Resolved Analysis of the SiO2/4H-SiC Interface*. Conference Name: Silicon Carbide and Related Materials 2019 Pages: 581-586 Volume: 1004. 2020. DOI: 10.4028/www.scientific.net/MSF.1004.581.

[304] Jun Sugiyama et al. "Li-ion diffusion in $Li_4Ti_5O_{12}$ and $LiTi_2O_4$ battery materials detected by muon spin spectroscopy". In: *Physical Review B* 92 (2015), p. 014417. DOI: 10.1103/PhysRevB.92.014417.

[305] Jun Sugiyama. "Spin polarized beam for battery materials research: $\mu_{\pm SR}$ and β_{-NMR}". In: *Hyperfine Interactions* 240 (2019), p. 17. DOI: 10.1007/s10751-019-1560-4.

[306] Z. Salman et al. "Near-Surface Structural Phase Transition of $SrTiO_3$ Studied with Zero-Field β-Detected Nuclear Spin Relaxation and Resonance". In: *Phys. Rev. Lett.* 96.14 (2006), p. 147601. DOI: 10.1103/PhysRevLett.96.147601. URL: https://link.aps.org/doi/10.1103/PhysRevLett.96.147601.

[307] K. Yokoyama et al. "Photoexcited Muon Spin Spectroscopy: A New Method for Measuring Excess Carrier Lifetime in Bulk Silicon". In: *Physical Review Letters* 119 (2017), p. 226601. DOI: 10.1103/PhysRevLett.119.226601.

[308] I. Belosevic et al. "muCool: A next step towards efficient muon beam compression". In: *Eur. Phys. J. C* 79.5 (2019), p. 430. DOI: 10.1140/epjc/s10052-019-6932-z. arXiv: 1811.08332 [physics.acc-ph].

[309] A. Aqeel et al. "Probing current-induced magnetic fields in Au—YIG heterostructures with low-energy muon spin spectroscopy". In: *Applied Physics Letters* 110 (2017), p. 062409. DOI: 10.1063/1.4975487.

[310] T. Moorsom et al. "Reversible spin storage in metal oxide—fullerene heterojunctions". In: *Science Advances* 6 (2020), eaax1085. DOI: 10.1126/sciadv.aax1085. (Visited on 03/21/2020).

[311] Lu Li et al. "Coexistence of magnetic order and two-dimensional superconductivity at LaAlO3/SrTiO3 interfaces". In: *Nature Physics* 7 (2011), pp. 762–766. DOI: 10.1038/nphys2080.

[312] Julie A. Bert et al. "Direct imaging of the coexistence of ferromagnetism and superconductivity at the LaAlO3/SrTiO3 interface". In: *Nature Physics* 7 (2011), pp. 767–771. DOI: 10.1038/nphys2079.

[313] G. M. Luke et al. "Time-reversal symmetry-breaking superconductivity in Sr2RuO4". In: *Nature* 394 (1998), pp. 558–561. DOI: 10.1038/29038.

[314] Lin Jiao et al. "Chiral superconductivity in heavy-fermion metal UTe2". In: *Nature* 579 (2020), pp. 523–527. DOI: 10.1038/s41586-020-2122-2.

[315] G. Janka et al. "Intense beam of metastable Muonium". In: *The European Physical Journal C* 80 (2020), p. 804. DOI: 10.1140/epjc/s10052-020-8400-1.

[316] Y. Miyake et al. "Ultra slow muon microscopy by laser resonant ionization at J-PARC, MUSE". In: *Hyperfine Interactions* 216 (2013), pp. 79–83. DOI: 10.1007/s10751-012-0759-4.

[317] Takayuki Yamazaki et al. "Muon Cyclotron for Transmission Muon Microscope". In: *Proceedings of the 22nd International Conference on Cyclotrons and their Applications* Cyclotrons2019 (2020). DOI: 10.18429/JACOW-CYCLOTRONS2019-TUP024.

[318] Luping Zhou et al. "Simulation studies for upgrading the surface muon beamline μE4 at PSI". In: (2021). arXiv: 2108.04986 [physics.acc-ph].

[319] E. Köhler et al. "Application of muonic X-ray techniques to the elemental analysis of archeological objects". In: *Nuclear Instruments and Methods in Physics Research* 187 (1981), pp. 563–568. DOI: 10.1016/0029-554X(81)90389-X.

[320] H. Daniel. "Application of X rays from negative muons". In: *Nuclear Instruments and Methods in Physics Research Section B: Beam Interactions with Materials and Atoms* 3 (1984), pp. 65–70. DOI: 10.1016/0168-583X(84)90338-0.

[321] K Ninomiya et al. "Development of elemental analysis by muonic X-ray measurement in J-PARC". In: *Journal of Physics: Conference Series* 225 (2010), p. 012040. DOI: 10.1088/1742-6596/225/1/012040.

[322] A. D. Hillier et al. "Probing beneath the surface without a scratch — Bulk non-destructive elemental analysis using negative muons". In: *Microchemical Journal* 125 (2016), pp. 203–207. DOI: 10.1016/j.microc.2015.11.031.

[323] https://www.psi.ch/en/industry/news/tattoos-innovative-radiopharmaka-fur-die-theragnostik.

[324] J. Adam et al. "The MEG detector for $\mu^+ \to e^+\gamma$ decay search". In: *Eur. Phys. J. C* 73.4 (2013), p. 2365. DOI: 10.1140/epjc/s10052-013-2365-2. arXiv: 1303.2348 [physics.ins-det].

[325] D. Taqqu. "Compression and extraction of stopped muons". In: *Phys. Rev. Lett.* 97 (2006), p. 194801. DOI: 10.1103/PhysRevLett.97.194801.

[326] W. Blum et al. "The Drift of Electrons and Ions in Gases". In: 2008, pp. 1–48. DOI: 10.1007/978-3-540-76684-1_2.

[327] Yu Bao et al. "Muon cooling: longitudinal compression". In: *Phys. Rev. Lett.* 112.22 (2014), p. 224801. DOI: 10.1103/PhysRevLett.112.224801. arXiv: 1402.2418 [physics.acc-ph].

[328] A. Antognini et al. "Demonstration of Muon-Beam Transverse Phase-Space Compression". In: *Phys. Rev. Lett.* 125.16 (2020), p. 164802. DOI: 10.1103/PhysRevLett.125.164802. arXiv: 2003.11986 [physics.acc-ph].

[329] Ivana Belosevic. "Simulation and experimental verification of transverse and longitudinal compression of positive muon beams: Towards a novel high-brightness low-energy muon beam-line". PhD thesis. Zurich, ETH, 2019. DOI: 10.3929/ethz-b-000402802.

[330] S. Bae et al. "First muon acceleration using a radio frequency accelerator". In: *Phys. Rev. Accel. Beams* 21.5 (2018), p. 050101. DOI: 10.1103/PhysRevAccelBeams.21.050101. arXiv: 1803.07891 [physics.acc-ph].

[331] D. Schrage et al. "CW RFQ fabrication and engineering". In: (Dec. 1998). URL: https://www.osti.gov/biblio/335199.

[332] Colin Carlile et al. *European Spallation Source Technical Design Report*. Apr. 2013. ISBN: 978-91-980173-2-8. DOI: 10.13140/RG.2.1.2040.6483/1.

[333] A. Antognini et al. "Studying Antimatter Gravity with Muonium". In: *Atoms* 6.2 (2018), p. 17. DOI: 10.3390/atoms6020017. arXiv: 1802.01438 [physics.ins-det].

[334] S. Chatrchyan et al. "The CMS Experiment at the CERN LHC". In: *JINST* 3 (2008), S08004. DOI: 10.1088/1748-0221/3/08/S08004.

[335] H. Chr. Kastli et al. “CMS barrel pixel detector overview”. In: *Nucl. Instrum. Meth. A* 582 (2007). Ed. by Giovanni Ambrosi et al., pp. 724–727. DOI: 10.1016/j.nima.2007.07.058. arXiv: physics/0702182.

[336] W. Adam et al. “The CMS Phase-1 Pixel Detector Upgrade”. In: *JINST* 16.02 (2021), P02027. DOI: 10.1088/1748-0221/16/02/P02027. arXiv: 2012.14304 [physics.ins-det].

[337] J. H. Jungmann-Smith et al. “Towards hybrid pixel detectors for energy-dispersive or soft X-ray photon science”. In: *Journal of Synchrotron Radiation* 23.2 (2016), pp. 385–394. DOI: 10.1107/S1600577515023541.

[338] A. Bergamaschi et al. “The MÖNCH Detector for Soft X-ray, High-Resolution, and Energy Resolved Applications”. In: *Synchrotron Radiation News* 31.6 (2018), pp. 11–15. DOI: 10.1080/08940886.2018.1528428.

[339] Aschkan Allahgholi et al. “The Adaptive Gain Integrating Pixel Detector at the European XFEL”. In: *Journal of Synchrotron Radiation* 26.1 (2019), pp. 74–82. DOI: 10.1107/S1600577518016077.

[340] Ch. Broennimann et al. “Development of an indium bump bond process for silicon pixel detectors at PSI”. In: *Nucl. Instrum. Meth. A* 565 (2006). Ed. by J. Grosse-Knetter et al., pp. 303–308. DOI: 10.1016/j.nima.2006.05.011. arXiv: physics/0510021.

[341] Christopher J. Kenney et al. “A Prototype monolithic pixel detector”. In: *Nucl. Instrum. Meth. A* 342 (1994), pp. 59–77. DOI: 10.1016/0168-9002(94)91411-7.

[342] R. Turchetta et al. “A monolithic active pixel sensor for charged particle tracking and imaging using standard VLSI CMOS technology”. In: *Nucl. Instrum. Meth. A* 458 (2001), pp. 677–689. DOI: 10.1016/S0168-9002(00)00893-7.

Acronyms

μSR muon spin rotation

ALP axion-like particle

AMM anomalous magnetic moment

APV atomic parity violation

BG background

BR branching ratio

BSM beyond the Standard Model

CDCH cylindrical drift chamber

CDW charge density wave

cLFV charged lepton flavour violation

D-MAPS depleted monolithic active pixel sensor

DC direct current

DR dilution refrigerator

EDM electric dipole moment

EFT effective field theory

FMR ferromagnetic resonance

Gas PM gaseous photo multiplier tube

GPU graphics processing unit

HFS hyperfine splitting

HIMB High-Intensity Muon Beams

HLbL hadronic light-by-light scattering

HPGe high-purity germanium

HVMAPS high-voltage monolithic active pixel sensor

HVP hadronic vacuum polarisation

LE-μSR low-energy muon spin rotation

LE-μ^+ low-energy muon

LEM Low Energy Muons

LHC Large Hadron Collider

LXe liquid xenon

LYSO Lutetium–Yttrium oxyorthosilicate

MFV minimal flavour violation

MPGD micro-pattern gaseous detector

MPPC multi-pixel photon counter

MSSM minimal supersymmetric Standard Model

NMR nuclear magnetic resonance

PV parity violation

QED quantum electrodynamics

RF radio frequency

RFQ radio frequency quadrupole

RMD radiative muon decay

RMS root mean square

RPC resistive plate chamber

SμS Swiss Muon Source

SES single event sensititivity

SFHe superfluid helium

SiPM silicon photomultiplier

SLS Swiss Light Source

SM Standard Model of particle physics

TDC time-to-digital converter

TPC time projection chamber

TRSB time-reversal symmetry breaking

VUV vacuum ultraviolet